

NO-A194 955

PIEZOELECTRIC AND ELECTROSTRICTIVE MATERIALS FOR  
TRANSDUCER APPLICATIONS. (U) PENNSYLVANIA STATE UNIV  
UNIVERSITY PARK MATERIALS RESEARCH LAB.

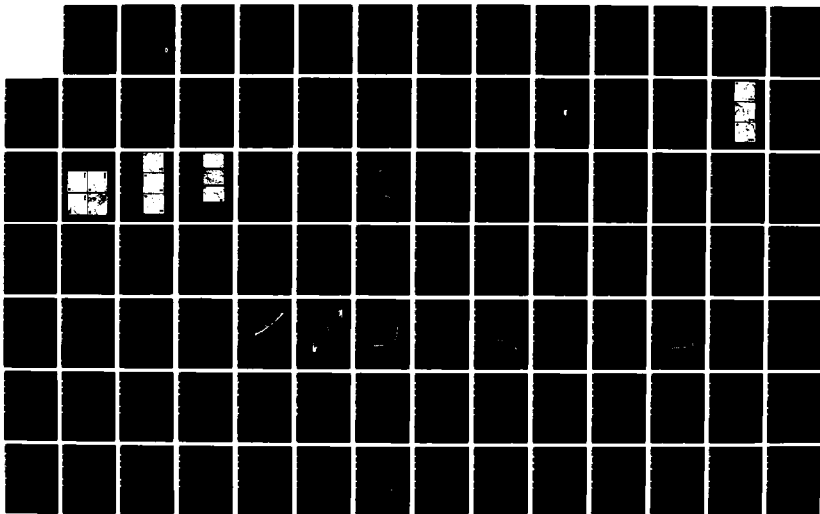
1/2

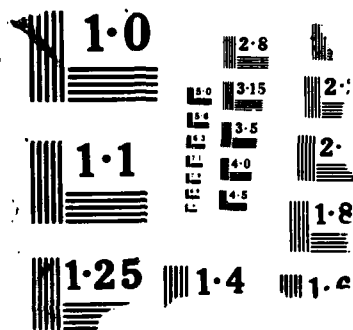
UNCLASSIFIED

L E CROSS ET AL. MAR 88 N00014-82-K-8339

F/G 20/3

NL





4

# PIEZOELECTRIC AND ELECTROSTRICTIVE MATERIALS FOR TRANSDUCER APPLICATIONS

AD-A194 955

DTIC FILE COPY

Period January 1 to December 31, 1987

Annual Report

OFFICE OF NAVAL RESEARCH

Contract No. N00014-82-K0339

APPROVED FOR PUBLIC RELEASE--DISTRIBUTION UNLIMITED

Reproduction in whole or in part is permitted for any purpose of the  
United States Government

L.E. Cross  
R.E. Newnham  
G.R. Barsch  
J.V. Biggers

March 1988

DTIC  
ELECTE  
MAY 09 1988  
S E D

Volume III



**THE MATERIALS RESEARCH LABORATORY**

THE PENNSYLVANIA STATE UNIVERSITY

UNIVERSITY PARK, PENNSYLVANIA

88 5 9 04 8

## List of Tables

Table I. Coefficients of the Energy Function.

Table II. Values of the Constants in the Energy Function used in Calculations.

## List of Figures

Figure 1. Spontaneous polarization as a function of temperature calculated for the stable and the metastable regions of the ferroelectric rhombohedral form.

Inset. Comparison with measured polarization over the stable range of the phase.

Figure 2. Spontaneous lattice strain  $x_4$  as a function of temperature calculated for the stable and metastable regions of the ferroelectric rhombohedral form.

Inset. Comparison of calculated and measured strain over the stable region of the phase.

Figure 3. Antiferroelectric orthorhombic strain  $x_4$  as a function of temperature: Comparison of calculated and measured values.

Figure 4. Calculated free energy  $\Delta G$  for ferroelectric and antiferroelectric forms.

Inset is an expanded scale to permit identification of the  $F_R$  to  $A_F$  and  $A_F$  to paraelectric transitions.

Figure 5. Calculated dielectric permittivity in the antiferroelectric orthorhombic phase averaged for a polycrystalline sample.

Inset. Comparison with low frequency dielectric data.

Figure 6. Measured microwave relaxation in the dielectric permittivity of lead zirconate (Lanagan et al.<sup>5</sup>) compared to the calculated room temperature value for the antiferroelectric polycrystal.

Figure 7. Comparison of calculated permittivity as a function of temperature with measured values at low and at microwave frequencies.

Figure 8. Values of  $\Xi = \Delta G_{FR}(\text{at } T_{AF})/\Delta G_{A0}(PZ)$  required to fit calculated and measured phase diagrams.  $\Xi$  is assumed to be independent of temperature.



Accession For	
NTIS GRA&I	<input checked="" type="checkbox"/>
DTIC TAB	<input type="checkbox"/>
Unannounced	<input type="checkbox"/>
Justification	
By	
Distribution/	
Availability Codes	
Dist	Avail and/or Special
A-1	

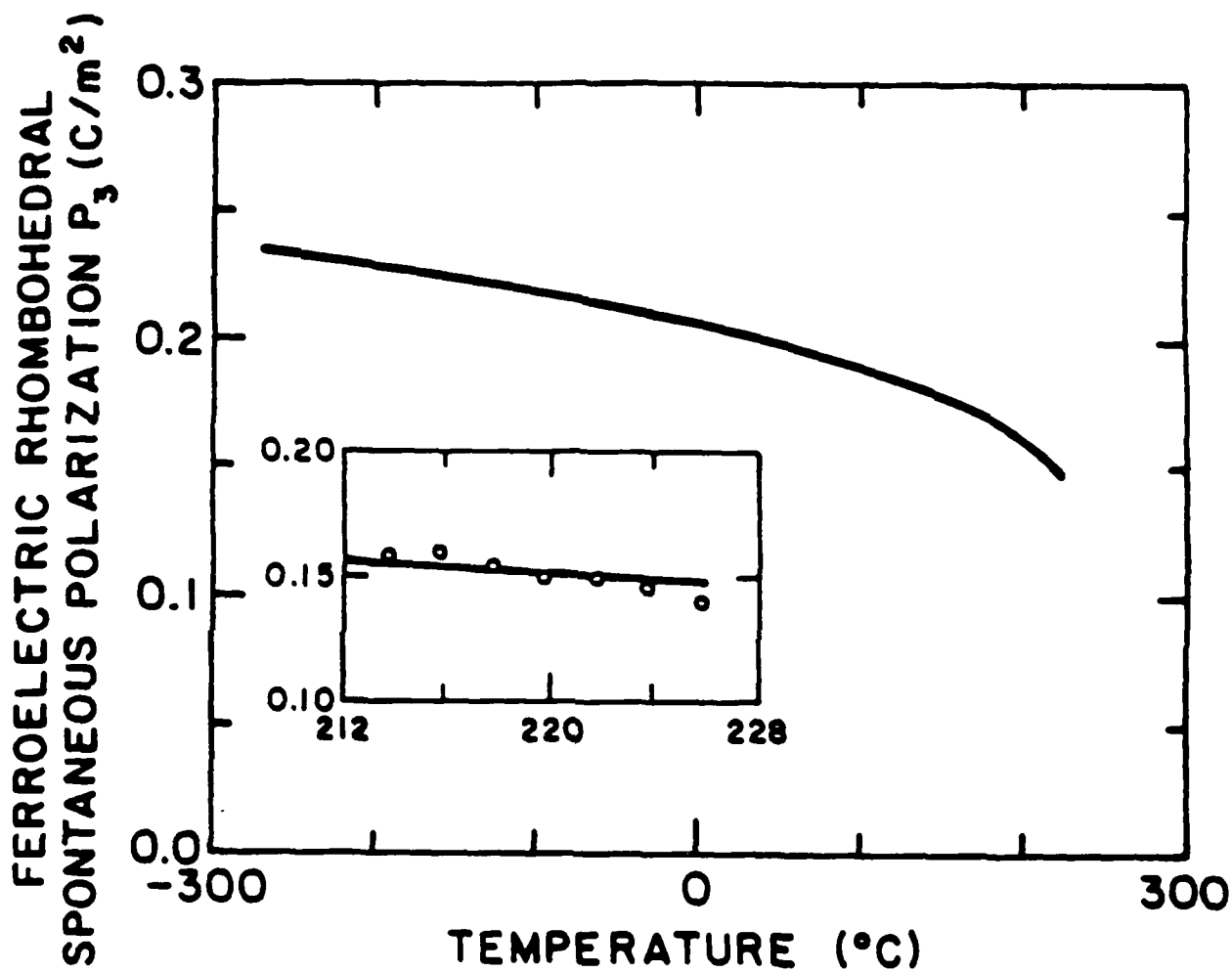


Fig. 1

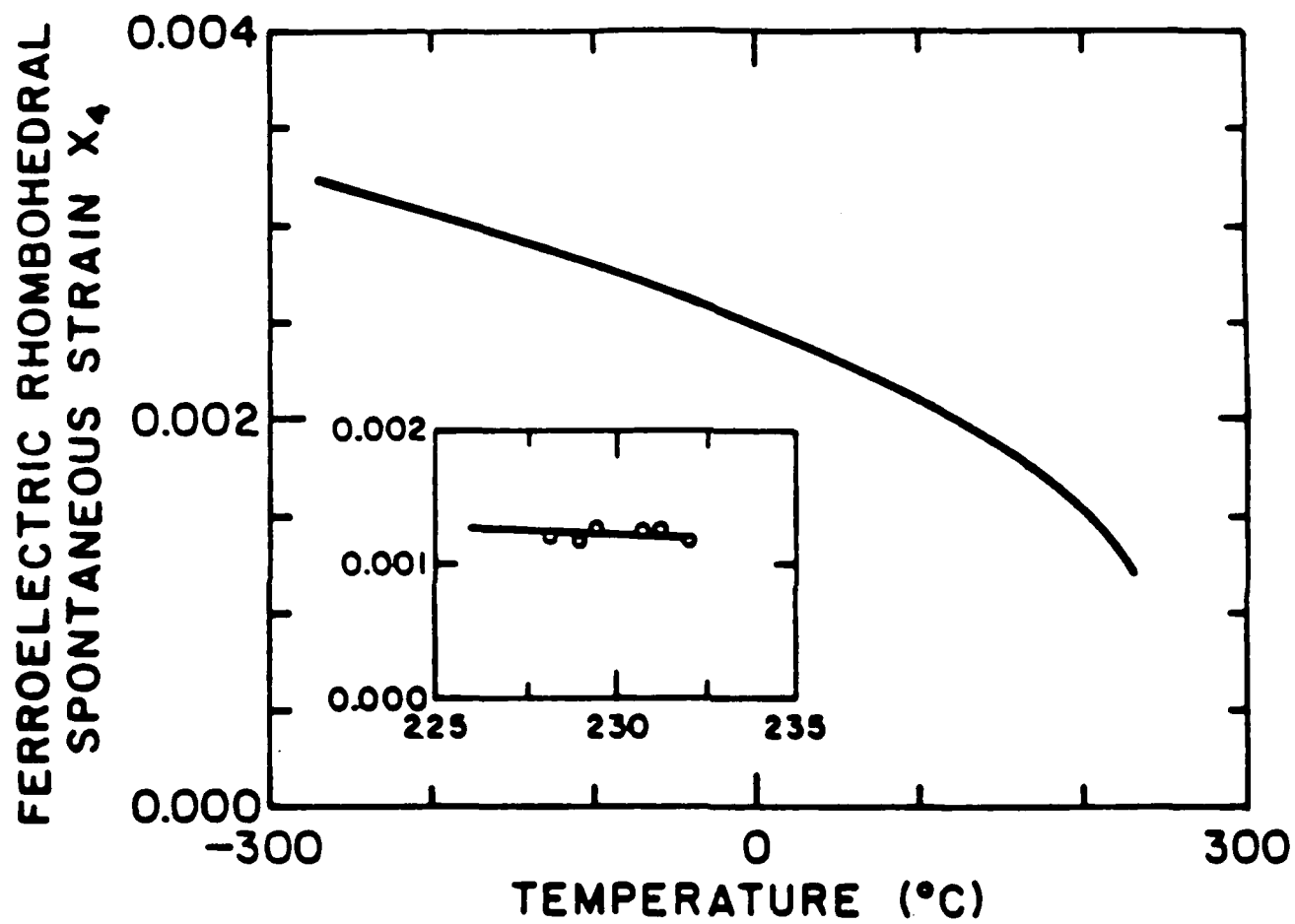
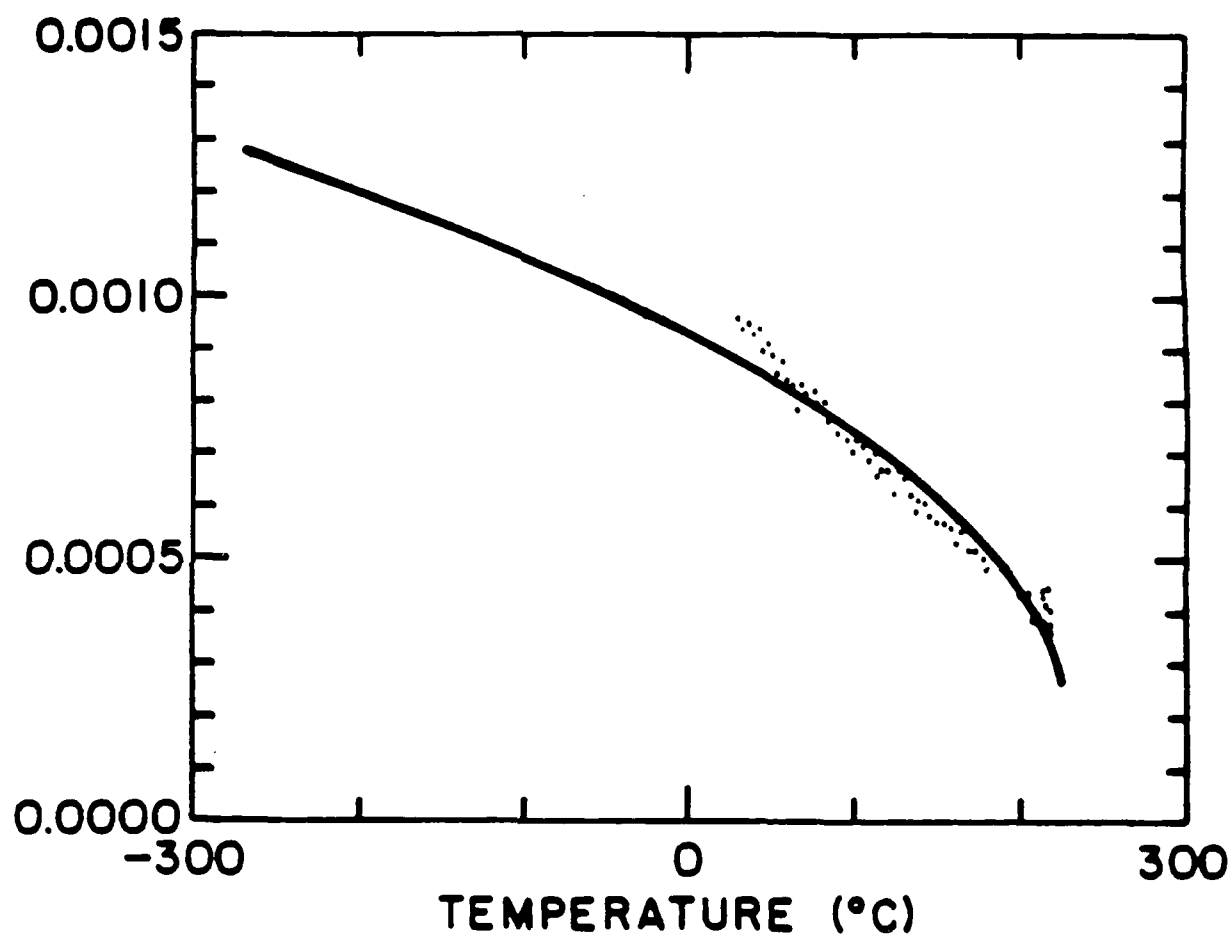


Fig. 2

ANTIFERROELECTRIC ORTHORHOMBIC  
SPONTANEOUS STRAIN  $\times 4$



*Fig. 3*

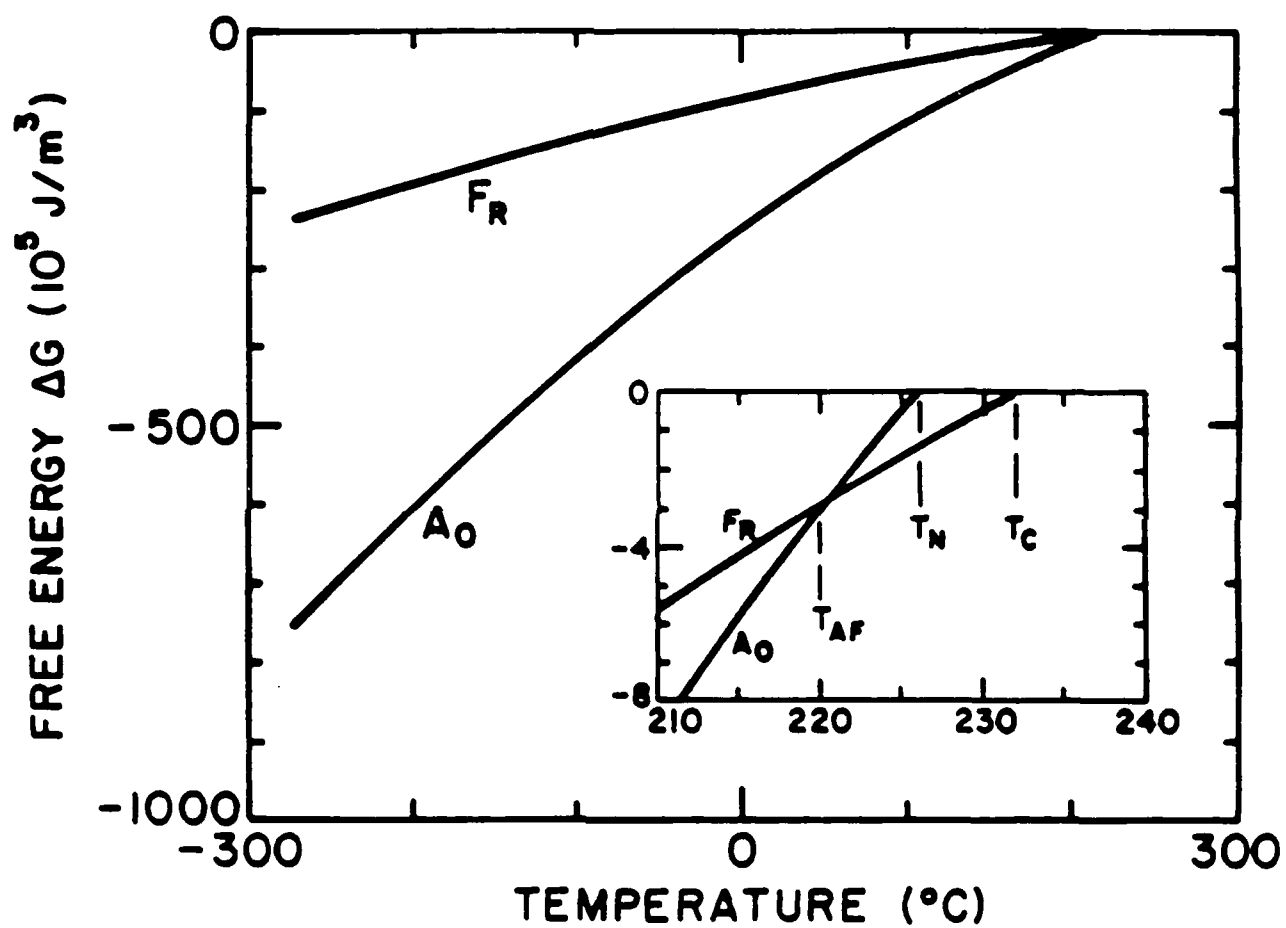


Fig. 4



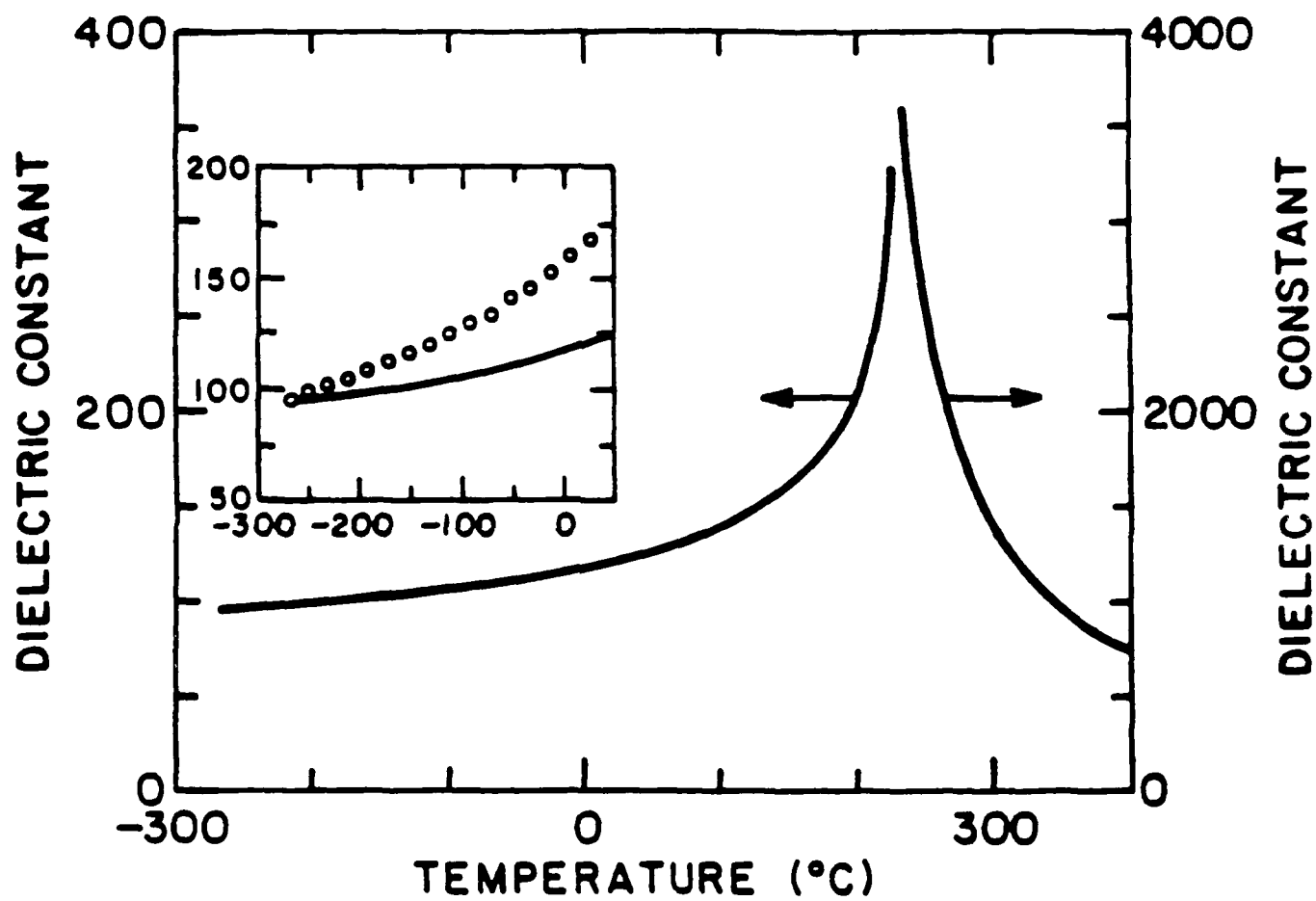


Fig. 5

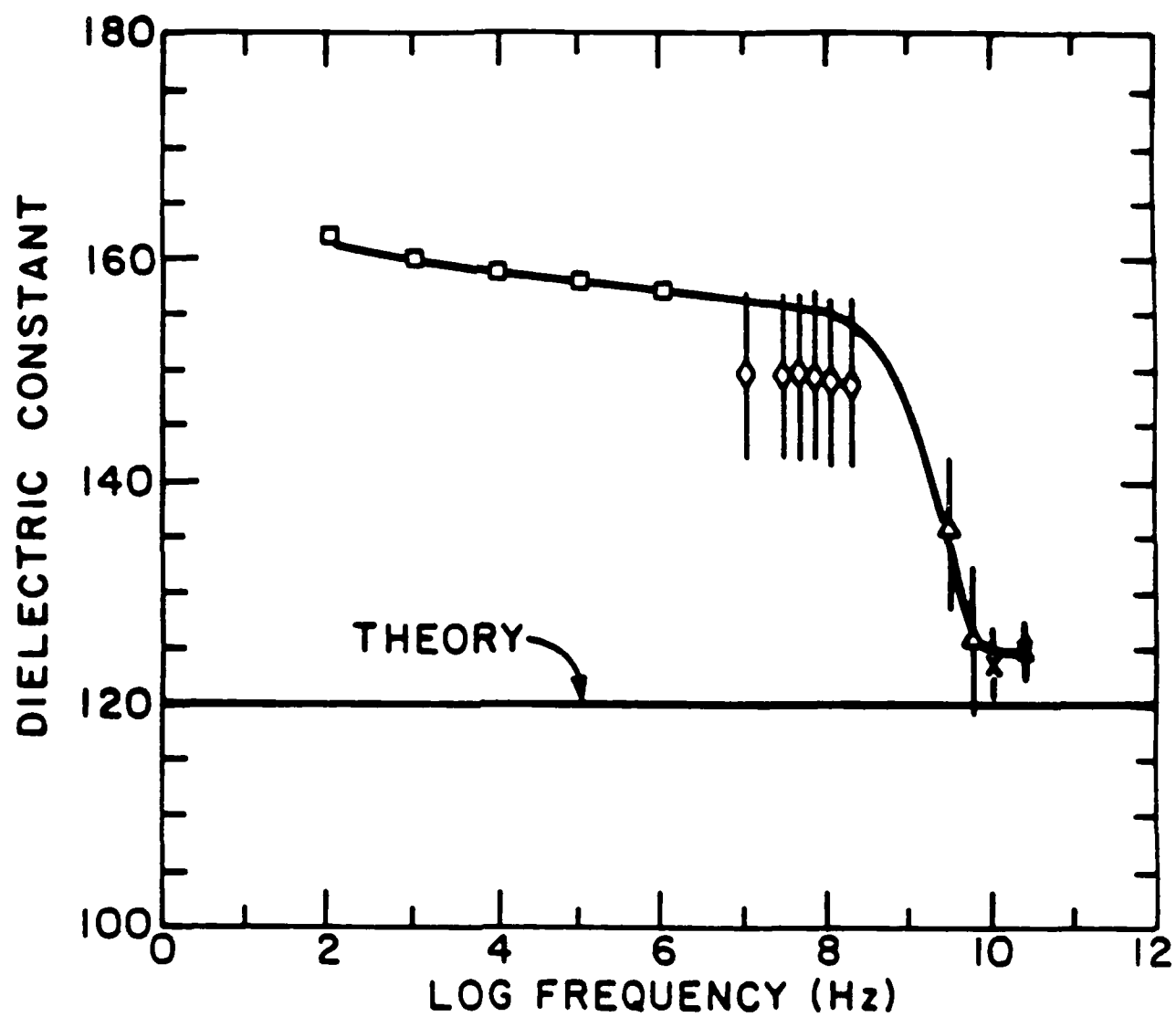


Fig. 6

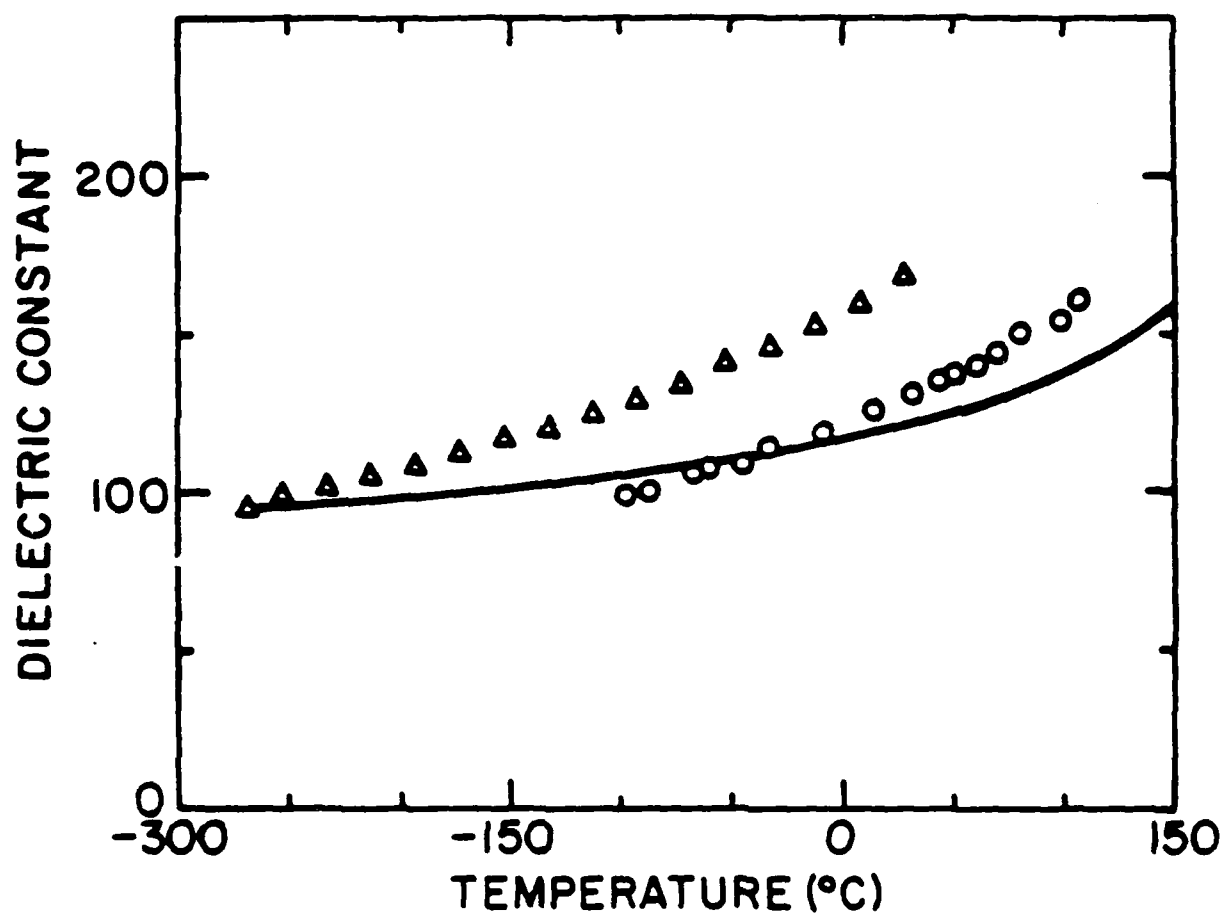
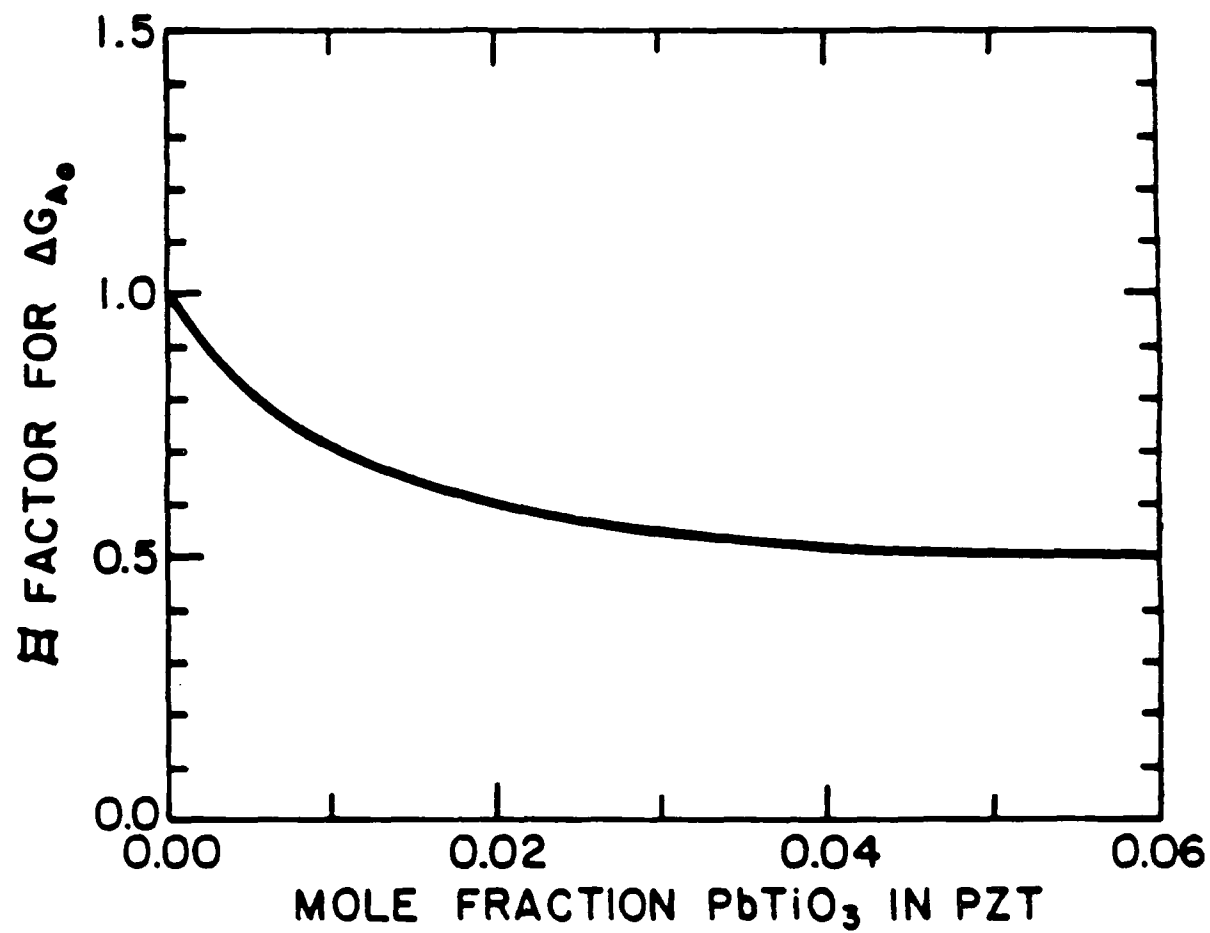


Fig. 7



*Fig. 8*

## FABRICATION AND CHARACTERIZATION OF PURE HOMOGENEOUS PZT CERAMICS FROM SOL-GEL DERIVED POWDERS

Z.Q. Zhuang<sup>†</sup>, M.J. Haun, S.J. Jang, and L.E. Cross

Materials Research Laboratory  
The Pennsylvania State University  
University Park, PA 16802

### ABSTRACT

In the course of the development of a phenomenological theoretical model for the whole lead zirconate-titanate solid solution system, it was found that some of the required experimental information was missing. To permit these required measurements, pure homogeneous ceramic samples of specific PZT compositions were fabricated from sol-gel derived powders. This paper describes the preparation and characterization of these required compositions.

High-purity lead acetate, titanium isopropoxide, and zirconium n-propoxide were used as precursors to form PZT powders using a sol-gel technique. X-ray powder diffraction was used to study the effect of calcining time and temperature from 400 to 900°C. The submicron-size calcined powders were sintered at temperatures from 1000 to 1250°C, depending on the composition, into high density (96 to 97% of the theoretical density) ceramic bodies with uniform microstructure. Excess lead oxide was included in the starting powders to control the lead stoichiometry and to act as a transient liquid phase to facilitate grain growth and densification by eliminating the porosity in the ceramics during sintering. The effects of density and of a second phase of lead oxide in the grain boundaries on the dielectric properties and poling characteristics are discussed.

<sup>†</sup>Visiting Scientist from the Department of Inorganic Materials Science and Engineering,  
South China Institute of Technology, Guangzhou, The People's Republic of China.

## I. INTRODUCTION

Additional experimental data were found to be needed to complete the development of a phenomenological theory for the lead zirconate-titanate (PZT) solid solution system.<sup>1-2</sup> For this purpose pure homogeneous polycrystalline ceramic PZT samples of compositions across the ferroelectric region of the phase diagram were fabricated from sol-gel derived powders. The dielectric, piezoelectric, elastic, electrostrictive, and pyroelectric properties were measured on these samples. Future publications will describe these measurements and the use of this data in the development of the phenomenological theory for PZT.

The purpose of this paper is to present the details of the experimental procedure used to fabricate dense ceramic PZT samples from sol-gel derived powders. X-ray diffraction patterns and scanning electron micrographs of the calcined powders and sintered ceramic samples will be presented. The effects of the ceramic density and the existence of a second phase of lead oxide in the grain boundaries on the dielectric properties and poling characteristics will also be discussed.

## II. EXPERIMENTAL PROCEDURE

A sol-gel method described in Reference 3 was used to prepare powders of pure lead zirconate-titanate with compositions of  $\text{Pb}(\text{Zr}_x\text{Ti}_{1-x})\text{O}_3$  with values of  $x$  ranging from 0.4 to 0.94. This method was similar to the procedure used in Reference 4 to prepare  $\text{PbTiO}_3$ . High-purity lead acetate  $[\text{Pb}(\text{C}_2\text{H}_3\text{O}_2)_2 \cdot 3\text{H}_2\text{O}]$ , titanium isopropoxide  $[\text{Ti}(\text{OC}_3\text{H}_7)_4]$ , and zirconium n-propoxide  $[\text{Zr}(\text{OC}_3\text{H}_7)_4]$  were used as precursors, with methoxyethanol  $[\text{C}_3\text{H}_8\text{O}_2]$  used as the solvent. A flow chart of the sol-gel procedure used is shown in Figure 1.

Excess lead oxide was included in these PZT powders to control the lead stoichiometry during the sintering of ceramic samples. The excess lead oxide also acted as a transient liquid phase to aid in sintering dense ceramics. It was incorporated into the powders by starting with additional lead acetate during the sol-gel procedure. The amount of excess lead oxide added varied from one-half to eight mole percent depending on the composition and on the final grain size of the ceramic samples that was desired. Due to the greater partial pressure of lead oxide in

lead zirconate compared to that in lead titanate, the amount of excess lead oxide was increased as the Zr/Ti ratio of the PZT compositions increased.

To study the effect of calcining conditions, the dried PZT 50/50 gel was calcined at several temperatures for different lengths of time. The gel was first heated slowly to 250 °C and held for three hours to remove some of the organics. The powder was still x-ray amorphous after this heat treatment. Five gram amounts of this powder were placed in alumina crucibles and calcined at 400 to 900 °C for different lengths of time. The crucibles were placed into the furnace at the calcine temperature, held for the desired length of time, and then removed from the furnace and quenched in air. The crystallized phases and particle size of the powders were then determined using x-ray diffraction and scanning electron microscopy.

All of the PZT compositions were calcined using the following procedure to produce powders to be used to press pellets for sintering into ceramic samples. The dried gels were first heated at a rate of 3 °C/min to 200 °C and held for 30 min. The temperature was then raised at 8 °C/min to 750 °C with one hour holds at 500 and 750 °C.

Green pellets 1.25 cm in diameter and 3 mm thick were uniaxially pressed in a steel die at 5,000 psi without binder. The pellets were sintered on platinum sheets in a set of alumina crucibles with a lead oxide source at 1000 to 1280 °C, depending on the composition. Lead zirconate with five weight percent excess lead oxide was used as the lead oxide source powder.

The alumina crucible arrangement is shown in Figure 2. By varying the number of crucibles and the amount of lead oxide source powder used, the sintering time could be varied from one to 60 hours to control the density and grain size of the sintered ceramic samples.

The samples used for dielectric property measurements were sputtered with gold electrodes. The dielectric constant and dielectric loss under a weak ac field were measured at frequencies of 0.1, 1, 10 and 100 KHz using a Hewlett Packard 4274A multifrequency LCR meter under full program control in an HP9816 computer-controlled system. The temperature dependence of the dielectric properties was measured during cooling at a rate of 2 °C per minute using a Delta Design 2300 environmental chamber.

X-ray powder diffraction was carried out on an APD 3600 Philips Automated X-ray diffractometer with  $\text{CuK}\alpha$  radiation, using as-prepared gel powders, calcined powders and powders crushed from freshly sintered ceramics.

### III. RESULTS AND DISCUSSION

The x-ray powder diffraction patterns of the PZT 50/50 composition calcined at different temperatures for one hour are shown in Figure 3. The x-ray pattern of the dried amorphous gel is also shown in this figure. As described in the Experimental Procedure section, the dried gel was first heated to  $250^\circ\text{C}$  for 3 hours, and then placed directly into the furnace at the calcine temperature.

After calcining the gel at  $500^\circ\text{C}$  for one hour, two phases with perovskite and pyrochlore-type structures had crystallized as shown in Figure 3(B). After  $600^\circ\text{C}$  for one hour [Figure 3(C)] only the perovskite phase was detected. As the calcine temperature was increased, the tetragonal splitting of the perovskite peaks became more distinct [Figures 3(D)-(F)].

Above  $600^\circ\text{C}$  additional diffraction peaks developed corresponding to the crystallization of lead oxide as orthorhombic  $\text{PbO}$ , and possibly also as tetragonal  $\text{PbO}$  and orthorhombic  $\text{PbO}_2$ . As described previously, excess lead oxide was included in the powders to aid in sintering dense ceramic samples.

Figure 4 shows x-ray diffraction patterns of the PZT 50/50 composition calcined at  $800^\circ\text{C}$  for several different lengths of time. After calcining for five minutes, the perovskite PZT and lead oxide phases had crystallized along with cubic lead metal [Figure 4(A)]. The diffraction peaks at  $31.32$  and  $36.32$  degrees two-theta correspond to metallic lead, which was probably formed because of the reducing environment created by these calcining conditions. Metallic lead was found to be present when calcining at  $500$ - $900^\circ\text{C}$  for short times of less than 15 minutes. However at  $400^\circ\text{C}$  metallic lead was the only phase that crystallized and remained even after calcining for one hour.



After calcining for 15 minutes at 800 °C [Figure 4(B)], the lead metal was no longer present. The sharpness of the tetragonal perovskite peaks increased as the calcining time was increased [Figures 4(A)-(E)]. In addition, the ratios of the different forms of lead oxide present appeared to change as the calcine time was increased.

Figure 5 shows SEM micrographs of PZT 50/50 powders, calcined at three different temperatures. As shown previously, after calcining at 500 °C for one hour, phases with perovskite and pyrochlore structures had crystallized. Figure 5(A) shows the SEM micrograph of this powder. By increasing the calcine temperature the particle size of the powder increased, as shown in Figures 5(B) and (C).

Calcining at 750 °C for one hour was found to produce optimum powders for uniaxial pressing of pellets without binder. This temperature was also low enough to avoid the volatilization of lead oxide during calcining, and high enough to fully crystallize the perovskite PZT phase. Using the heating rates and hold times that were described in the Experimental Procedure section, all of the compositions were calcined at 750 °C for one hour.

X-ray diffraction patterns of these calcined powders are shown in Figures 6 and 7. The hkl's of the tetragonal and rhombohedral perovskite peaks have been labeled in Figures 6(A) and 7(A), respectively. As previously discussed the additional peaks correspond to lead oxide. Figures 6(B) and (C) show that for the PZT 50/50 and 52/48 compositions the tetragonality is less than that of the PZT 40/60 composition. The diffraction pattern of the PZT 50/50 composition calcined at 750 °C shown in Figure 6(B) should be compared with the patterns shown in Figures 3(D) and (E) for powders calcined at 700 and 800 °C.

Figure 8 shows SEM micrographs of four different PZT compositions calcined as described above. The particle sizes of the tetragonal compositions 52/48 and 50/50 [Figures 8(A) and (B)] are considerably larger than that of the rhombohedral compositions 54/56 and 90/10 [Figures 8(C) and (D)]. This may be due to the higher crystallization energies of the higher zirconia content compositions.

Figure 9 shows the scanning electron microstructures of the surfaces of ceramic samples of PZT 52/48 sintered at 1150 °C for 7, 18.5 and 34 hours. This figure shows that the open porosity decreased as the sintering time increased. As shown in Figure 9(A), the sample sintered for 7 hours had a uniform surface microstructure, even though the density was low (91% of the theoretical density). As the soaking time was increased to 18.5 hours grain growth and a decrease in porosity occurred, but this led to a nonuniform distribution of grain size, as shown in Figure 9(B). By further increasing the soaking time to 34 hours a more uniform microstructure resulted from continued grain growth, and the density increased to 97% of the theoretical density [see Figure 9(C)].

As shown by Figure 9 dense ceramic samples with uniform microstructures could be achieved at relatively low temperatures by sintering for long times. To be able to sinter for long times the lead oxide atmosphere had to be carefully controlled through the addition of excess lead oxide into the samples and by using the crucible arrangement and lead source described in the Experimental Procedure section.

This technique was also employed in preparing dense ceramic samples for all of the other PZT compositions. As an example, Figure 10(A) shows the SEM microstructure of the surface of a sample of rhombohedral PZT 60/40 ceramic sintered at 1100 °C for 30 hours. This sample had a density of 97% of the theoretical density.

Figures 10(B) and (C) show the SEM microstructure of the fracture surface of a PZT 50/50 ceramic sample sintered at 1015 °C for 25 hours. These figures show that the grains had embedded into each other because of the continuous grain growth during the long sintering time. This sample had a uniform grain size with a density of 97% of the theoretical density.

In addition to obtaining dense ceramics, single phase compositions were obtained by allowing the excess lead oxide to gradually volatilize out of the samples during the long sintering times. This can be observed in Figures 11 and 12, which show the x-ray diffraction patterns for the tetragonal and rhombohedral compositions, respectively. These figures show that within the limits of x-ray diffraction the excess lead oxide had volatilized out of the samples and only the

perovskite PZT phase remained after sintering. The yellow color of the samples also indicated that the excess lead oxide had volatilized out. A reddish color occurred when excess lead oxide remained in the samples.

If the excess lead oxide had not completely "boiled out" of the sample a deviation from lead stoichiometry could result and/or lead oxide could remain in the grain boundaries. Figures 13(A) and (B) show the temperature dependences of dielectric constant and loss for two PZT 50/50 ceramic samples. The solid lines in these figures correspond to a single phase ceramic sample, and the dashed lines correspond to a sample of the same composition with excess lead oxide still remaining. The dielectric constant for the single phase ceramic sample is larger than that of the sample with excess lead oxide. This can possibly be attributed to the existence of lead oxide of low dielectric constant (about 30 at room temperature<sup>5</sup>) being in a series with pure PZT grains.

The existence of lead oxide as a second phase in the grain boundaries is also harmful to the poling properties because of the concentration of the poling field on the boundary layer of lead oxide. This would result in lower piezoelectric constants.

Green pellets of PZT 52/48 were sintered at 1150 °C for 1.5, 7, 13.5, 18.5, 29.5, and 34 hours. Even though the soaking time was very different, single-phase ceramics were obtained by controlling the number of crucibles and the amount of lead source powder used. Shirasaki<sup>6</sup> showed that the lattice parameters of lead titanate changed significantly as the degree of lead stoichiometry was varied. The x-ray patterns of the PZT 52/48 samples with different soaking times were all very similar, as were the lattice parameters calculated from these patterns. This indicates that by controlling the sintering conditions, the lead stoichiometry could be controlled for all soaking times.

The dielectric constant and loss of these samples were plotted versus temperature in Figures 14(A) and (B). The density of these samples increased as the soaking time increased, which would contribute to the increase in dielectric constant as shown in Figure 14(A).

#### IV. CONCLUSION

High-purity lead acetate, titanium isopropoxide and zirconium n-propoxide were used as precursors to prepare pure homogeneous PZT powders at compositions across the ferroelectric region of the phase diagram by a sol-gel method.

In order to obtain compositionally stoichiometric ceramic samples, excess lead oxide was included in the compositions. The excess lead oxide acted as a transient liquid phase in the grain boundaries during sintering to maintain the compositional stoichiometry and to facilitate grain growth and densification by eliminating the porosity in the ceramics.

Dense (96 ~ 97% of the theoretical density) pure PZT ceramic samples with uniform microstructure were obtained at relatively low temperatures by sintering for long times. By controlling the amount of lead oxide source powder (PbO-rich lead zirconate) and changing the alumina crucible arrangement, the lead atmosphere could be maintained during the long sintering times. After sintering, only the perovskite PZT phase could be detected by x-ray powder diffraction.

As expected the dielectric constant was found to increase as the ceramic density increased. In addition, when excess lead oxide was present the dielectric properties were degraded.

The ceramic processing procedure described in this paper was used to fabricate pure homogeneous ceramic samples for low-temperature dielectric, piezoelectric, and elastic property measurements.<sup>3</sup> The electrostrictive and pyroelectric properties were also measured. Future publications will describe these measurements, and the use of these data in the development of a phenomenological thermodynamic theory of PZT.

#### ACKNOWLEDGEMENTS

The authors wish to thank Dr. T. Dekleva for setting up, demonstrating, and supplying the initial equipment for the sol-gel work, and Dr. B. V. Hiremath for help in the PZT processing and characterization.

## REFERENCES

- <sup>1</sup>A. Amin, Ph.D. Thesis, The Pennsylvania State University (1979); A. Amin, M.J. Haun, B. Badger, H.A. McKinstry, and L.E. Cross, "A Phenomenological Gibbs Function for the Single Cell Region of the  $\text{PbZrO}_3\text{:PbTiO}_3$  Solid Solution System," *Ferroelectrics*, 65, 107-130 (1985).
- <sup>2</sup>M.J. Haun, Z.Q. Zhuang, S.J. Jang, H.A. McKinstry, and L.E. Cross, "A Phenomenological Theory for the Second Order Transition Region of the PZT Solid Solution System," *Proc. of the 6th IEEE International Symposium on the Applications of Ferroelectrics*, Lehigh, PA, pp. 398-401 (1986).
- <sup>3</sup>Z.Q. Zhuang, M.J. Haun, S.J. Jang, and L.E. Cross, "Low Temperature Dielectric, Piezoelectric, and Elastic Properties of Pure (Undoped) PZT Ceramics," *Proc. of the 6th IEEE International Symposium on the Applications of Ferroelectrics*, Lehigh, PA, pp. 394-397 (1986).
- <sup>4</sup>S.R. Gurkovich and J.B. Blum, "Preparation of Monolithic Lead-Titanate by a Sol-gel Process," in *Ultrastructure Processing of Ceramics, Glasses, and Composites*, Edited by L.L. Hench and D.R. Ulrich, Wiley-Interscience, New York, p. 152 (1984).
- <sup>5</sup>K. Wasa and S. Hayakawa, "Dielectric Properties of  $\text{PbO}$  Thin Films," *Jpn. J. Appl. Phys.*, 8, 276 (1969).
- <sup>6</sup>S. Shirasaki, "Defect Lead Titanates with Diverse Curie Temperatures," *Solid State Comm.*, 9, 1217-1220 (1971).

## FIGURE CAPTIONS

- Figure 1. Flow chart of the sol-gel procedure used to prepare PZT powders.
- Figure 2. The crucible arrangement used for sintering ceramic samples.
- Figure 3. X-ray powder diffraction patterns of the (A) PZT 50/50 gel and the PZT 50/50 composition calcined for one hour at: (B) 500, (C) 600, (D) 700, (E) 800, and (F) 900 °C. In (B) I refers to the perovskite phase and II refers to the pyrochlore phase. In (F) the hkl's of the tetragonal perovskite phase are labeled.
- Figure 4. The x-ray powder diffraction patterns for sol-gel derived powders of PZT 50/50 calcined at 800 °C for: (A) 5 minutes, (B) 15 minutes, (C) 30 minutes, (D) 1 hour, and (E) 4 hours. In (E) the hkl's of the tetragonal perovskite phase are labeled.
- Figure 5. SEM micrographs of sol-gel derived PZT 50/50 powders calcined at (A) 500 °C for 1 hour, (B) 800 °C for 2 hours, and (C) 900 °C for 1 hour.
- Figure 6. X-ray powder diffraction patterns for tetragonal compositions calcined at 750 °C for 1 hour: (A) PZT 40/60, (B) PZT 50/50, and (C) PZT 52/48.
- Figure 7. X-ray powder diffraction patterns for rhombohedral compositions calcined at 750 °C for 1 hour: (A) PZT 60/40, (B) PZT 70/30, (C) PZT 90/10, and (D) PZT 94/6.
- Figure 8. SEM micrographs of sol-gel derived PZT powders calcined at 750 °C for 1 hour: (A) PZT 52/48, (B) PZT 50/50, (C) PZT 54/46, and (D) PZT 90/10.
- Figure 9. SEM surface microstructures of PZT 52/48 ceramics sintered at 1150 °C for (A) 7 hours, (B) 18.5 hours and (C) 34 hours.
- Figure 10. SEM microstructures of (A) the surface of PZT 60/40 sintered at 1100 °C for 30 hours, and (B) and (C) the fracture surfaces of PZT 50/50 sintered at 1015 °C for 25 hours.
- Figure 11. X-ray powder diffraction patterns for ceramics of tetragonal compositions: (A) PZT 40/60, (B) PZT 50/50, and (C) PZT 52/48.
- Figure 12. X-ray powder diffraction patterns for ceramics of rhombohedral compositions: (A) PZT 60/40, (B) PZT 70/30, (C) PZT 90/10, and (D) PZT 94/6.
- Figure 13. The temperature dependence of (A) the dielectric constant and (B) loss for PZT 50/50 ceramic samples. The solid lines correspond to a single phase ceramic sample and the dotted lines denote a sample with a second phase of lead oxide.
- Figure 14. The temperature dependences of the (A) dielectric constant and (B) loss for PZT 52/48 ceramics sintered at 1150 °C for (a) 1.5, (b) 7, (c) 13.5, (d) 18.5, (e) 29.5, and (f) 34 hours.

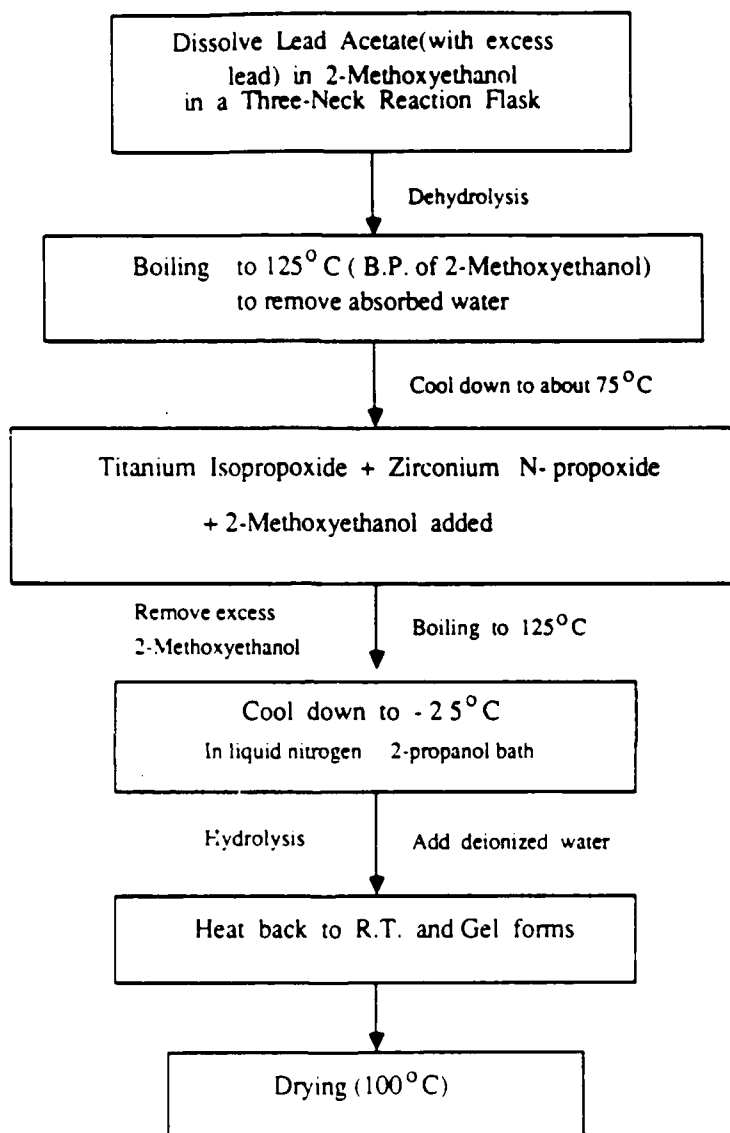


Fig. 1

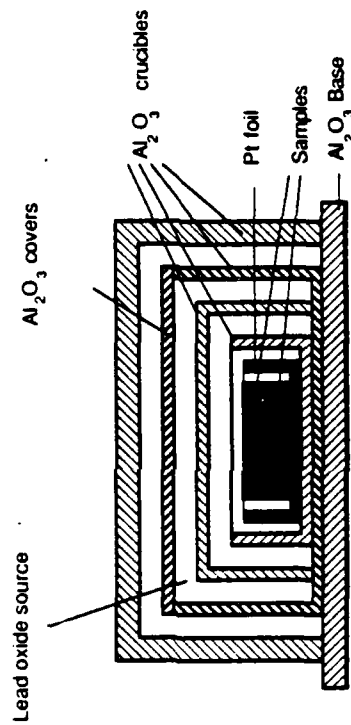


Fig. 2



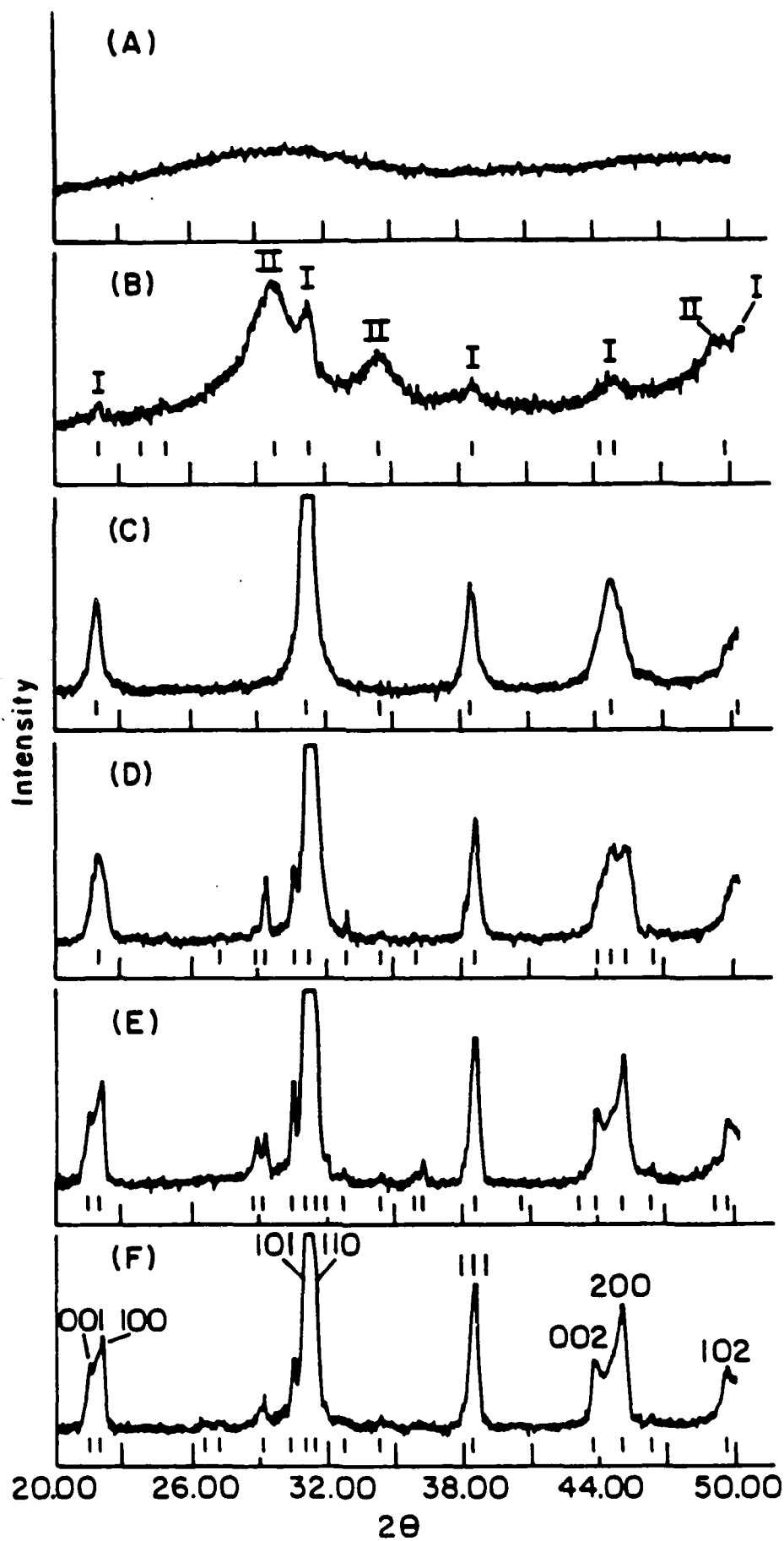


Fig. 3 (A)-(F)

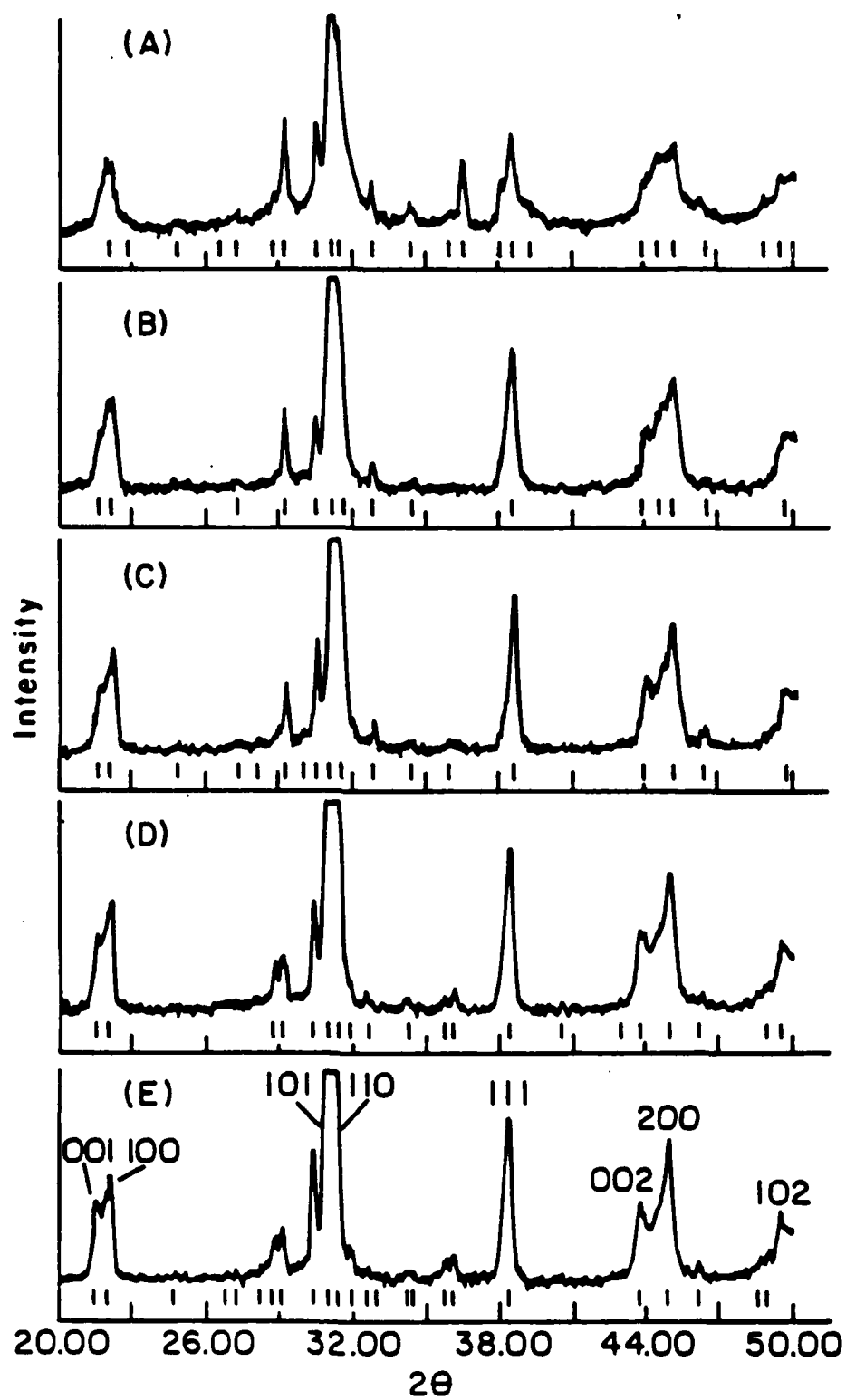


Fig. 4 (A) - (E)

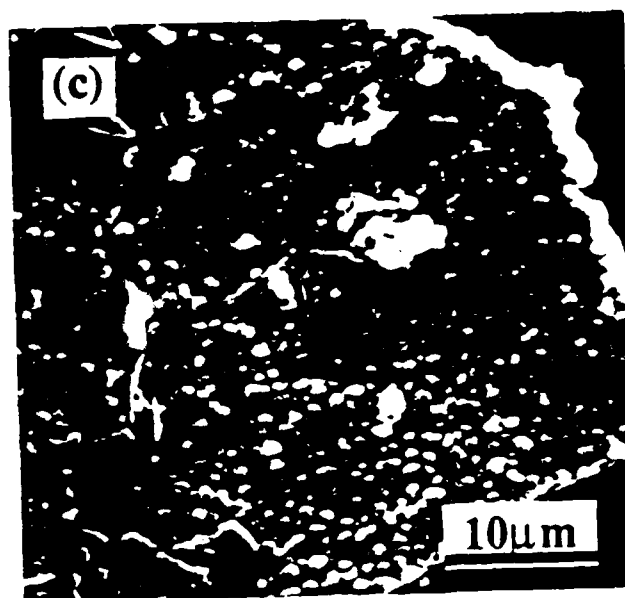
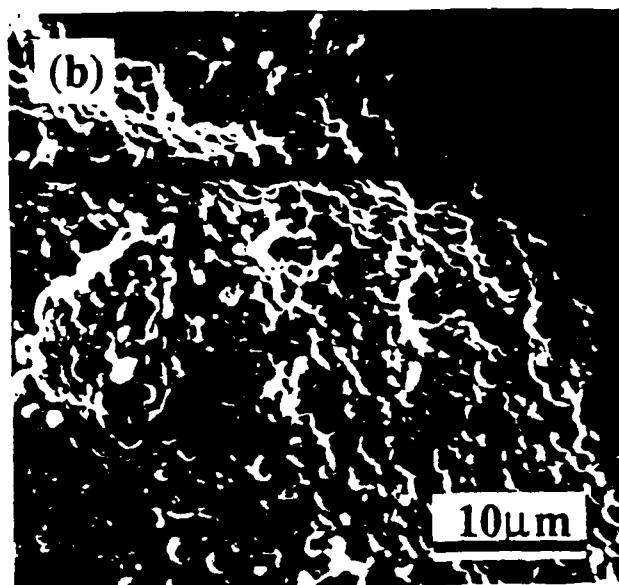
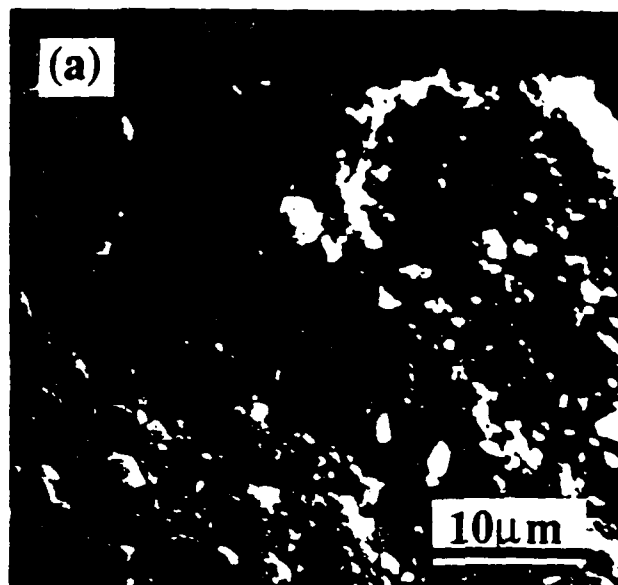


Fig. 5

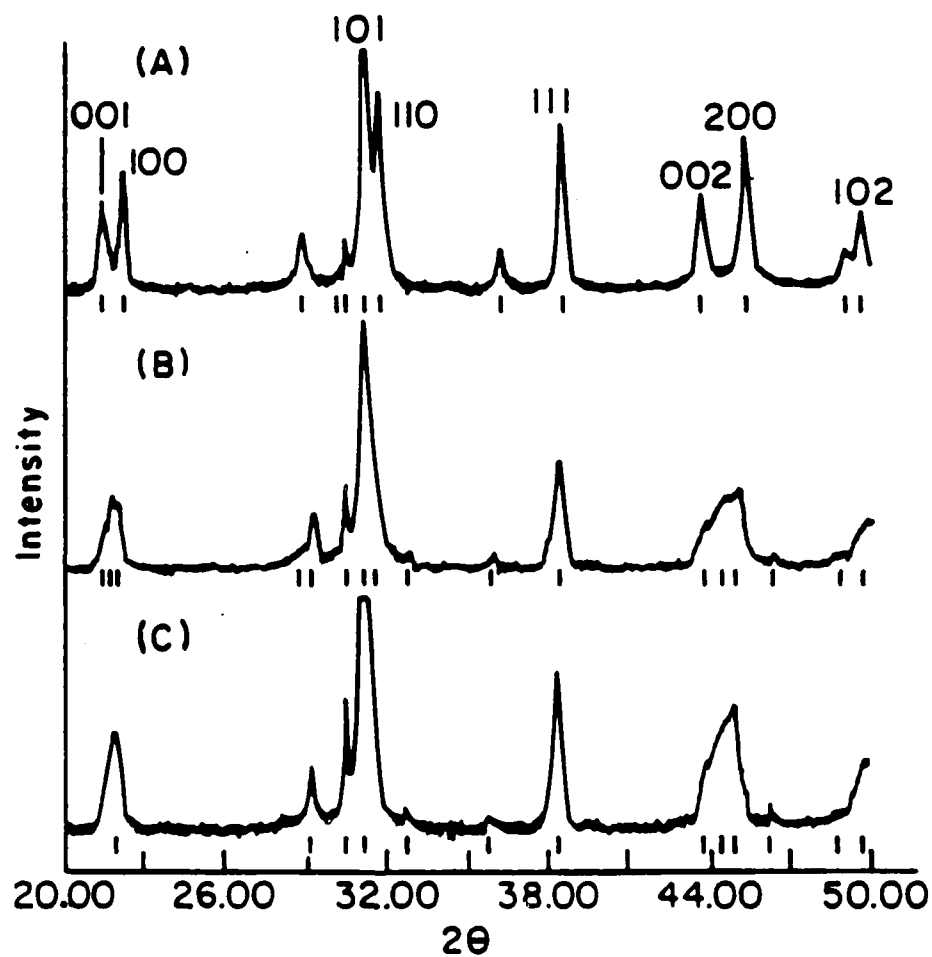


Fig. 6 (A) - (C)

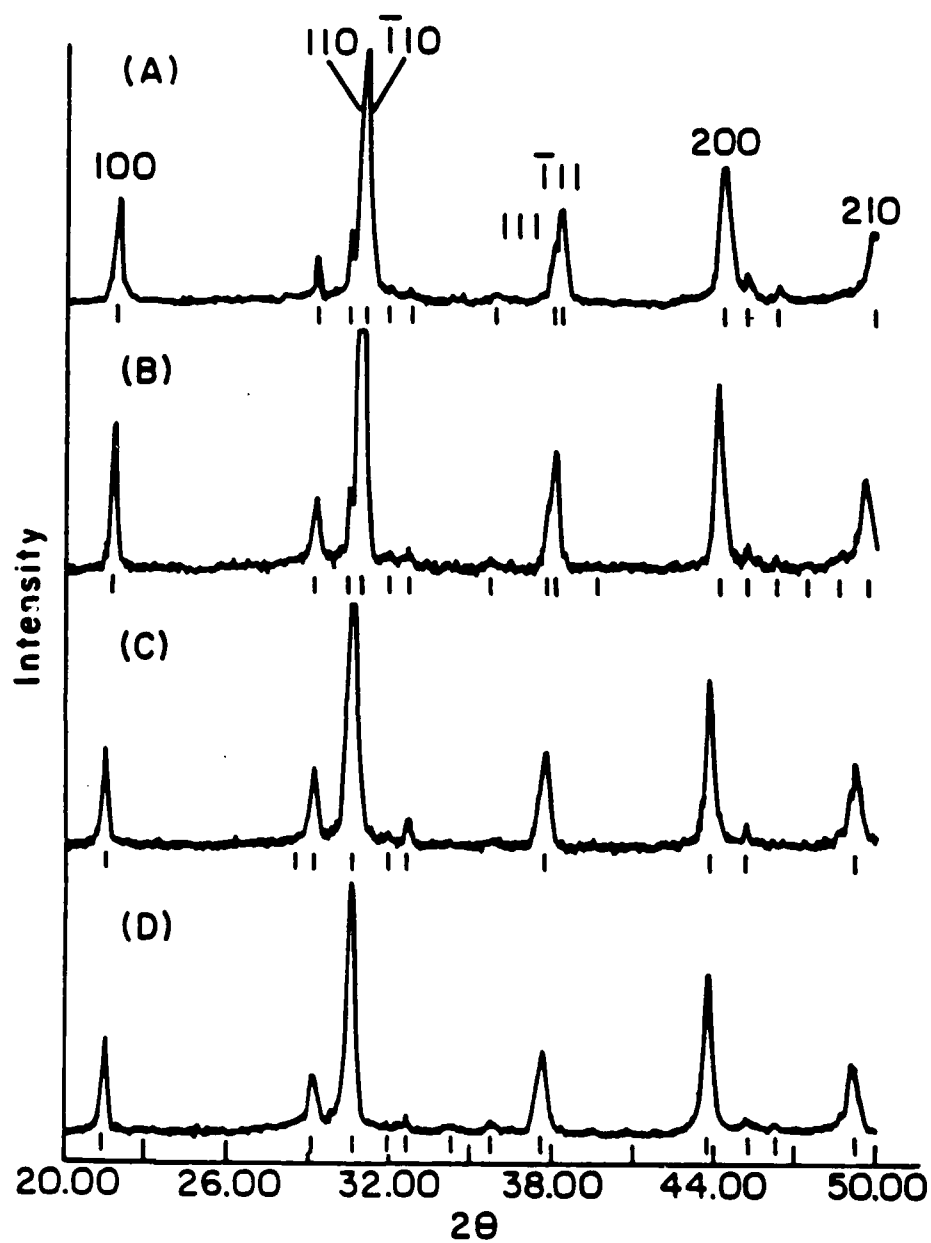


Fig. 7 (A)-(D)

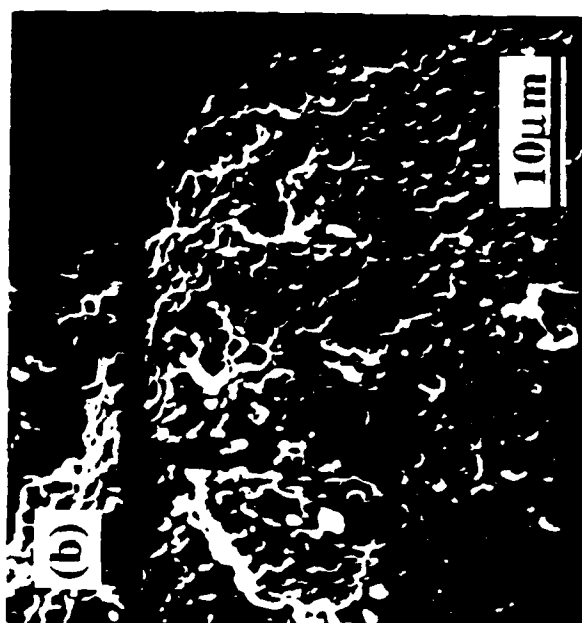
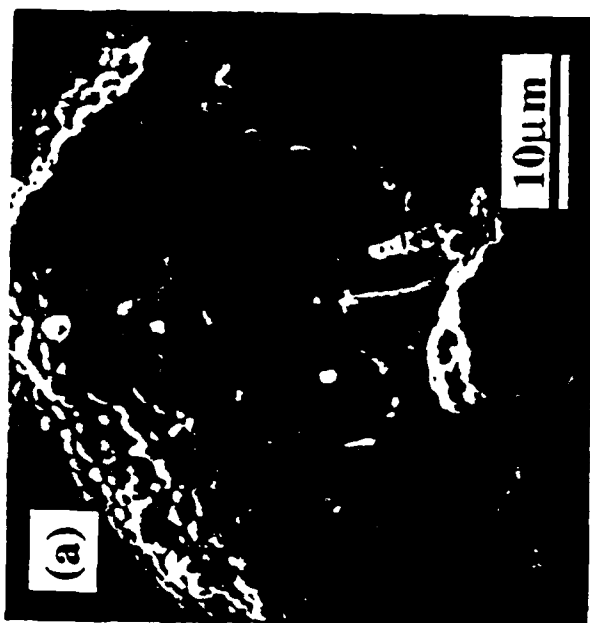


Fig. 8

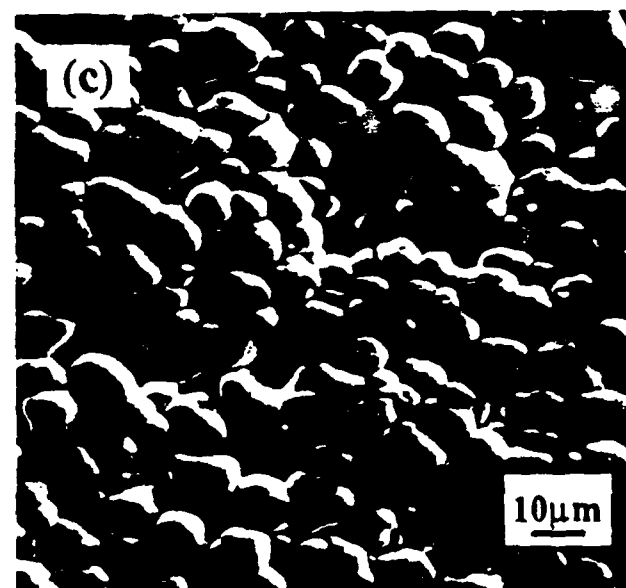
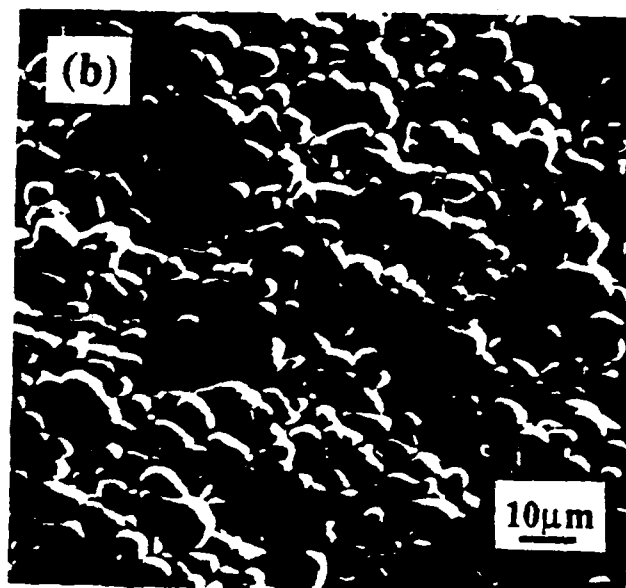
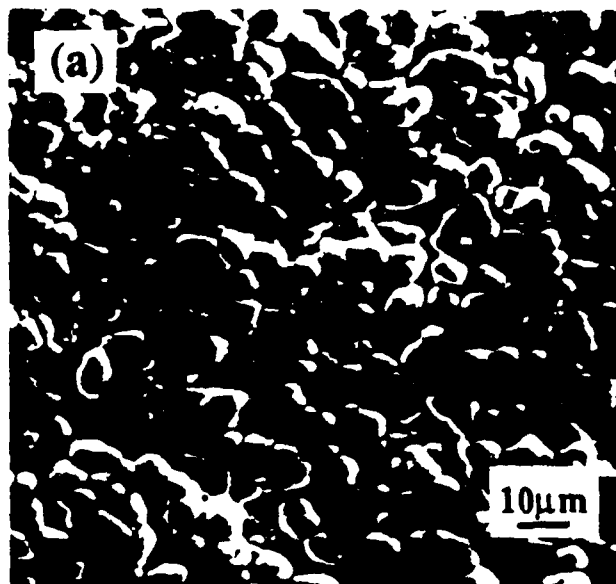


Fig. 9

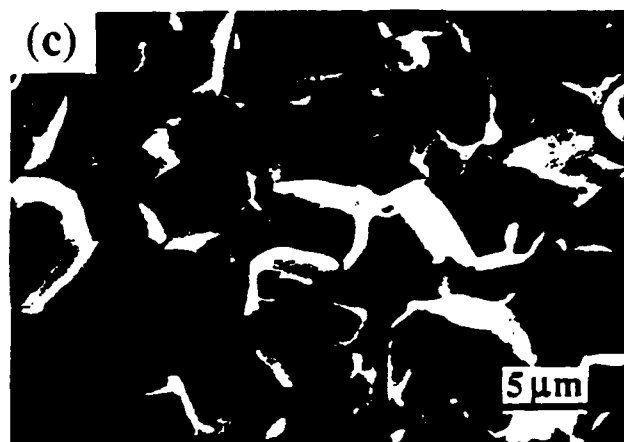
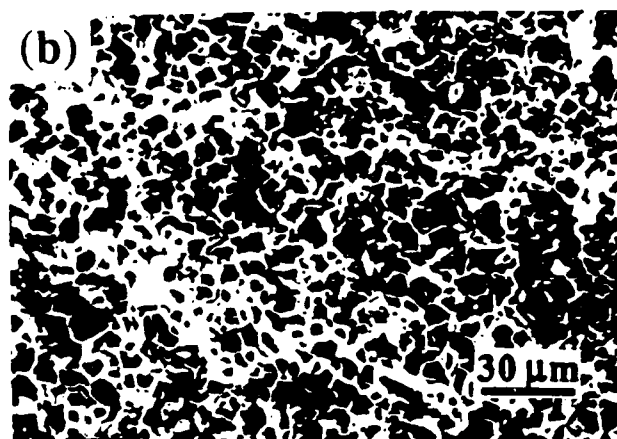
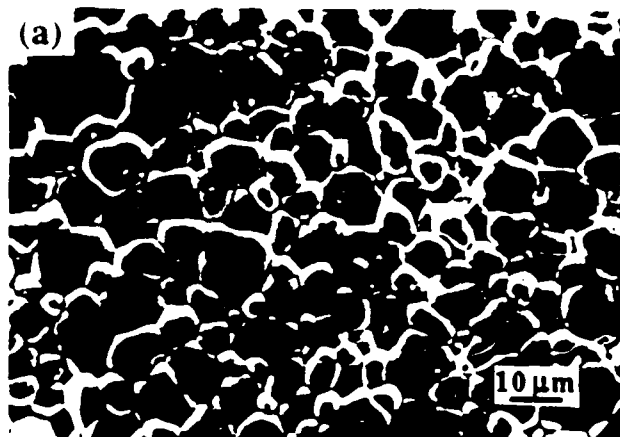


Fig. 10



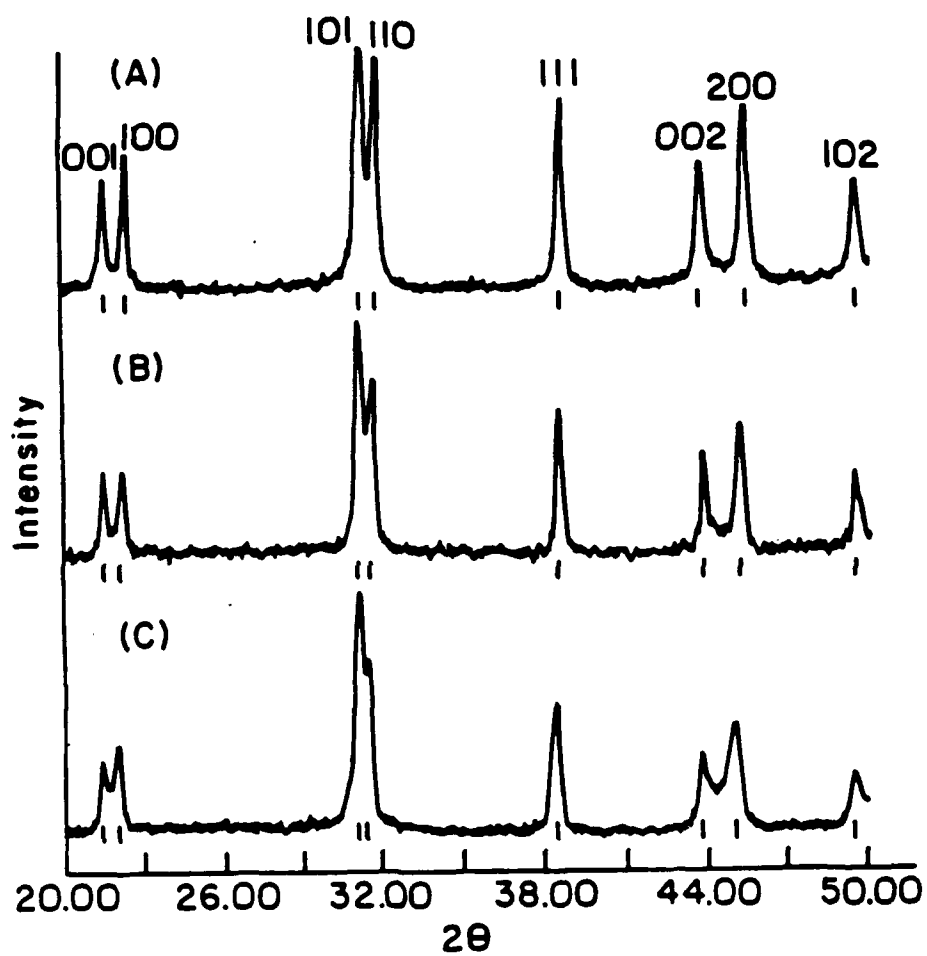


Fig. 11 (A) - (C)

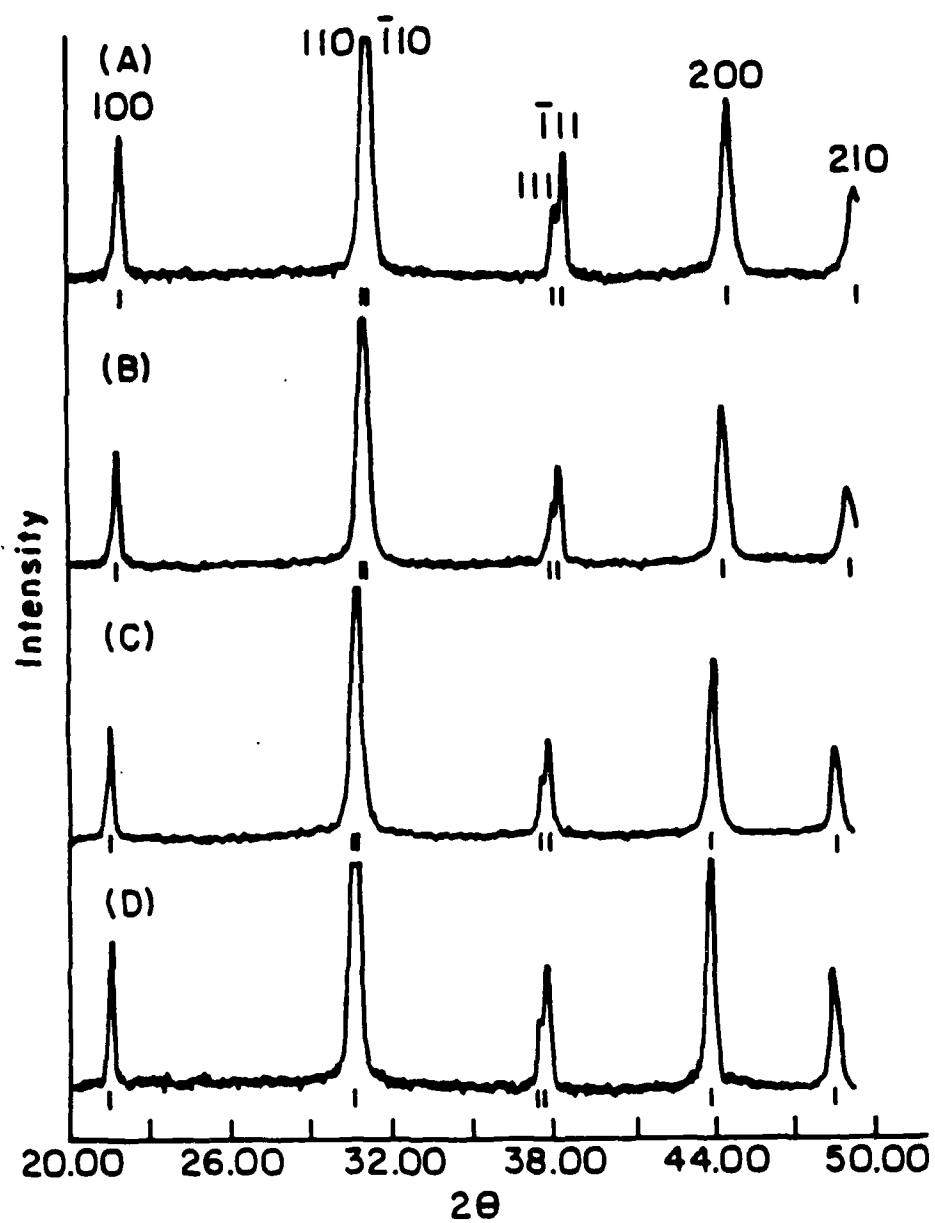
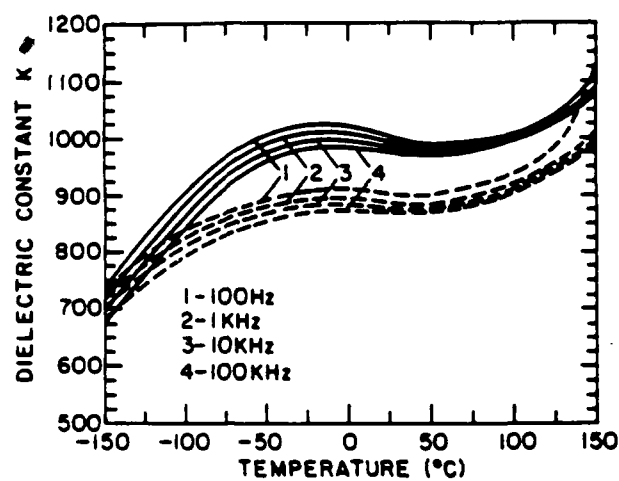
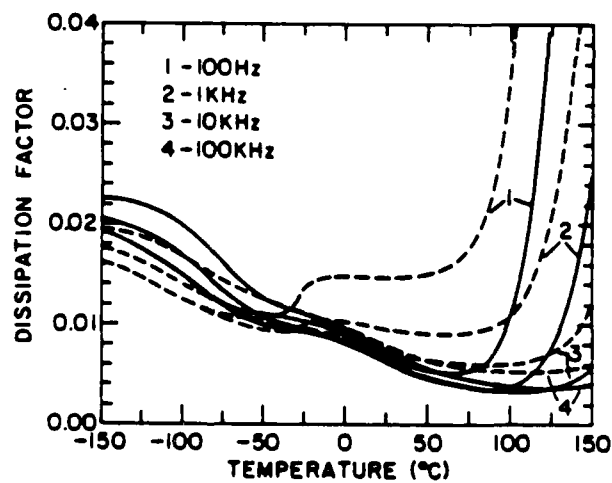


Fig. 12 (A)-(D)

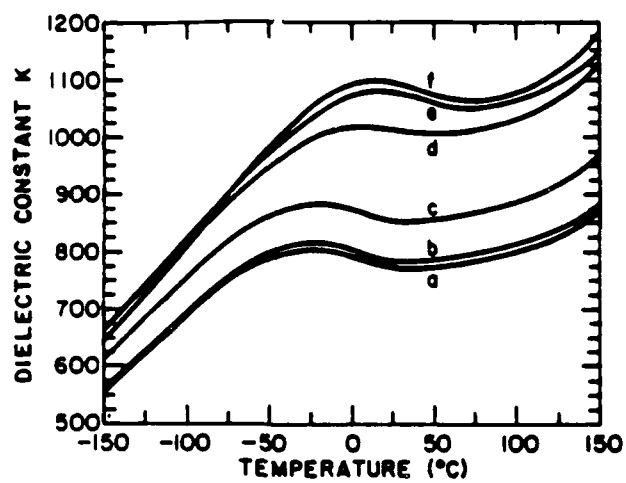


(A)

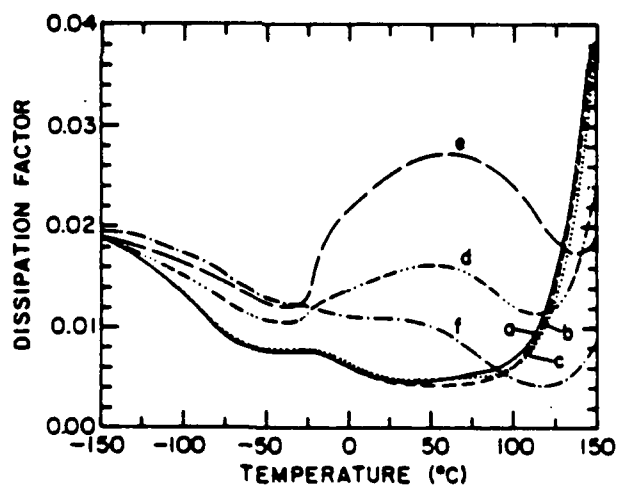


(B)

Fig. 13 (A) and (B)



(A)



(B)

Fig. 14 (A) and (B)

MODELING OF THE ELECTROSTRICTIVE, DIELECTRIC,  
AND PIEZOELECTRIC PROPERTIES OF CERAMIC  $\text{PbTiO}_3$

M. J. Haun, E. Furman, S. J. Jang, and L. E. Cross

Materials Research Laboratory  
The Pennsylvania State University  
University Park, PA 16802

ABSTRACT

The upper and lower limits of the electrostrictive constants, dielectric permittivities, spontaneous polarization, and piezoelectric coefficients were calculated for ceramic  $\text{PbTiO}_3$  from theoretical single crystal constants. Experimental ceramic data falls between these upper and lower limits. The large piezoelectric anisotropy  $\bar{d}_{33}/\bar{d}_{31}$  of ceramic  $\text{PbTiO}_3$  was shown to be related to the single crystal  $\text{PbTiO}_3$  electrostrictive anisotropies  $Q_{11}/Q_{12}$  and  $Q_{44}/Q_{12}$ . The possibility of a change in sign of the ceramic  $\bar{d}_{31}$  coefficient due to a slight variation in the single crystal electrostrictive anisotropies was discussed. The single crystal and predicted ceramic hydrostatic electrostrictive constants were found to be equal. Using this result the ceramic hydrostatic  $\bar{g}_h$  coefficient is always smaller than the single crystal  $g_h$ , but the ceramic hydrostatic  $\bar{d}_h$  coefficient can be either larger or smaller than the single crystal  $d_h$  depending on the dielectric anisotropy ( $\epsilon_{11}/\epsilon_{33}$ ) of the single crystal.

## 1. INTRODUCTION

Lead titanate has been extensively used as an end member of ceramic solid solution systems with important piezoelectric properties.<sup>1</sup> One particularly interesting property is the large piezoelectric anisotropy ( $d_{33}/d_{31}$ ) that has been achieved in modified lead titanate ceramics, but not present in the single crystal. These materials are of interest in high-frequency ultrasonic transducer applications.<sup>2</sup>

Turik et al.<sup>3</sup> showed that this large ceramic piezoelectric anisotropy could be obtained by averaging the single crystal piezoelectric coefficients. They concluded that the small single crystal dielectric and piezoelectric anisotropies of  $\text{PbTiO}_3$  lead to large ceramic piezoelectric anisotropy. Wersing et al.<sup>4,5</sup> combined Luchaninov's<sup>6</sup> averaging equations with Devonshire's<sup>7</sup> single crystal relations to calculate the ceramic piezoelectric coefficients from the single crystal dielectric permittivities, electrostrictive constants and spontaneous polarization. The ceramic  $d_{31}$  coefficient was found to disappear for a particular ratio of the electrostrictive coefficients and a certain degree of polarization.<sup>5</sup>

The purpose of this study is to further understand the behavior of  $\text{PbTiO}_3$  by calculating the ceramic electrostrictive constants, dielectric permittivities, spontaneous polarization, and piezoelectric coefficients from the single crystal constants that were recently determined from a Devonshire type phenomenological theory<sup>8</sup>. The upper and lower limits of the properties will be calculated using simple averaging relations. These calculations will then be compared with experimental data.

## 2. ELECTROSTRICTIVE CONSTANTS

The upper and lower limits of the ceramic elastic constants can be calculated from single crystal values using the Voigt and Reuss methods of averaging.<sup>9</sup> Voigt determined the stiffness of the ceramic from the space averages of the stiffnesses of the crystallites, while Reuss found the ceramic compliance from the space averages of the compliances of the crystallites. Hill<sup>9</sup> showed that both of these models are only approximate and that the true values should fall between these bounds. In most cases, the experimental values do fall between the Voigt and Reuss limits. Electrostriction is also a fourth rank tensor with similar matrix to tensor conversion as the elastic constants, and thus the same equations can be used to predict the upper and lower limits of the electrostrictive constants.

The electrostrictive ( $Q_{ijkl}$ ) and inverse electrostrictive ( $q_{ijkl}$ ) constants relate the strain ( $x_{ij}$ ) to the polarization components ( $P_k P_l$ ) by the following relations:

$$x_{ij} = Q_{ijkl} P_k P_l \quad (1)$$

$$P_i P_j = q_{ijkl} x_{kl} \quad (2)$$

The tensor to matrix conversions of the electrostrictive and inverse electrostrictive constants are the same as that of the elastic compliances and stiffnesses, respectively:

$$\begin{aligned} Q_{ijkl} &= Q_{mn} \cdot && \text{when } m \text{ and } n = 1, 2, \text{ or } 3 \\ 2Q_{ijkl} &= Q_{mn} \cdot && \text{when } m \text{ or } n = 4, 5, \text{ or } 6 \\ 4Q_{ijkl} &= Q_{mn} \cdot && \text{when } m \text{ and } n = 4, 5, \text{ or } 6 \end{aligned} \quad (3)$$

$$q_{ijkl} = q_{mn} \cdot \quad \text{for all } m \text{ and } n \quad (4)$$

Using a similar procedure as that of Voigt and Reuss for the elastic constants, the electrostrictive and inverse electrostrictive constants of a polycrystalline ceramic can be calculated from the space averages of the single crystal values by assuming that the ceramic is composed of a

Equations (5) and (9) give ceramic electrostrictive constants corresponding to the series and parallel models, respectively, and will be used to calculate the upper and lower bounds of the ceramic electrostrictive constants from the single crystal values. Devonshire<sup>7,10</sup> calculated the ceramic electrostrictive constants of BaTiO<sub>3</sub> using Equation (5). However at that time the single crystal electrostrictive constants had been overestimated due to the low values of the spontaneous polarization that were used in the calculations. Thus the agreement with experimental ceramic electrostrictive constants was not very good. When a more realistic value of the polarization (0.26 C/m<sup>2</sup> at room temperature) was later measured<sup>11</sup>, Jona and Shirane<sup>12</sup> recalculated the single crystal electrostrictive constants and used Equation (5) to determine the ceramic  $\bar{Q}_{11}$  and  $\bar{Q}_{12}$  values. These calculations were in good agreement with the experimental measurements.

The ceramic electrostrictive constants of BaTiO<sub>3</sub> were calculated from the single crystal values using Equations (5) and (9) as shown in Table I. The values of the experimental ceramic electrostrictive constants, also listed in this Table, fall between these upper and lower bounds. Thus the Voigt and Reuss type methods of averaging appear to work well in predicting the limits of the electrostrictive constants in addition to the elastic constants.

Two sets of calculated upper and lower bounds of the electrostrictive constants of ceramic PbTiO<sub>3</sub> are listed in Table I. The same values of the single crystal  $Q_{11}$  and  $Q_{12}$  constants were used in both sets of calculations, but different  $Q_{44}$  values were used. In the first set of PbTiO<sub>3</sub> calculations a  $Q_{44}$  of  $6.75 (10^{-2} \text{ m}^4/\text{C}^2)$  was used. This value was calculated in Reference 3 from experimental values of  $\epsilon_{11}$ ,  $d_{15}$ , and  $P_s$  from PbTiO<sub>3</sub> single crystals. In the second set of calculations a  $Q_{44}$  of  $2.0 (10^{-2} \text{ m}^4/\text{C}^2)$  was used. This value was calculated in Reference 15 from spontaneous polarization and strain data for the rhombohedral Pb(Zr<sub>0.9</sub>Ti<sub>0.1</sub>)O<sub>3</sub> composition. In all three sets of data shown in Table I the magnitudes of the ceramic  $\bar{Q}_{11}$  and  $\bar{Q}_{12}$  constants are less than the corresponding single crystal values, but the ceramic  $\bar{Q}_{44}$  constants are larger.

The electrostrictive anisotropies  $-\bar{Q}_{11}/\bar{Q}_{12}$  and  $-\bar{Q}_{44}/\bar{Q}_{12}$  increase in BaTiO<sub>3</sub> and PbTiO<sub>3</sub> ceramics compared to the corresponding single crystal anisotropies as shown in Table I. The



$-\bar{Q}_{11}/\bar{Q}_{12}$  anisotropy increases, even though the  $\bar{Q}_{11}$  constant decreases, because of the greater decrease in the  $-\bar{Q}_{12}$  constant. The  $-\bar{Q}_{44}/\bar{Q}_{12}$  anisotropy increases because of both the decrease in  $-\bar{Q}_{12}$  and increase in  $\bar{Q}_{44}$ .

The electrostrictive anisotropies of ceramic  $\text{PbTiO}_3$  are larger than those in  $\text{BaTiO}_3$ , because of the differences in single crystal anisotropies. In the second set of  $\text{PbTiO}_3$  data the ceramic anisotropies calculated from the parallel model changed sign because  $\bar{Q}_{12}$  became positive. To better understand the effect of the single crystal anisotropies on the ceramic anisotropy Equations (5) and (9) can be rearranged as shown below:

$$\bar{\sigma}_{\text{series}} = \frac{-1/\sigma + 1/(2\mu) + 4}{3/\sigma + 1/\mu - 2}, \text{ and} \quad (10)$$

$$\bar{\sigma}_{\text{parallel}} = \left[ 1 + \frac{2 + 3(1/\sigma - 1) + 4\mu(1/\sigma + 1)(1/\sigma - 2)}{4 + (1/\sigma - 1) - 2\mu(1/\sigma + 1)(1/\sigma - 2)} \right]^{-1}, \quad (11)$$

$$\text{where } \bar{\sigma} = -\bar{Q}_{12}/\bar{Q}_{11}, \quad \sigma = -Q_{12}/Q_{11}, \text{ and } \mu = -Q_{12}/Q_{44}. \quad (12)$$

The ratio  $\sigma$  is the electrostrictive analogue to Poisson's ratio ( $= -s_{12}/s_{11}$ ). The electrostrictive ratios defined by Equation (12) are the inverse of the electrostrictive anisotropies listed in Table I.

In Figure 1 the ceramic ratio  $\bar{\sigma}$  was plotted versus the single crystal  $\sigma$  ratio for different values of the single crystal  $\mu$  ratio using Equations (10) and (11). Using either the series or parallel models, the ceramic  $\bar{\sigma}$  ratio decreases (anisotropy increases) as the single crystal  $\sigma$  and  $\mu$  ratios decrease and increase, respectively. The value of the  $\mu$  ratio has less effect on the ceramic  $\bar{\sigma}$  when using the series model compared to the parallel model. The ceramic  $\bar{\sigma}$  can be either positive or negative depending on the values of the single crystal ratios. A negative value of the ceramic  $\bar{\sigma}$  would be due to a positive  $\bar{Q}_{12}$ , assuming that  $\bar{Q}_{11}$  is also positive. If the ceramic  $\bar{\sigma}$  changes sign because the  $-\bar{Q}_{12}$  constant decreased to zero and changed sign, then the ceramic anisotropy ( $-\bar{Q}_{11}/\bar{Q}_{12}$ ) would increase and go to infinity.

The square shaped data points in Figure 1 represent BaTiO<sub>3</sub>, and the circular and triangular shaped data points represent the first and second sets of PbTiO<sub>3</sub> data in Table I, respectively. As shown in Figure 1 the single crystal ratios of BaTiO<sub>3</sub> cause the ceramic  $\bar{\sigma}$  ratio to be larger than that of PbTiO<sub>3</sub> resulting in less anisotropy. When using the smaller value of the  $Q_{44}$  constant, the upper and lower limits of the PbTiO<sub>3</sub> ceramic  $\bar{\sigma}$  ratio range from positive to negative values, illustrating the possibility of having very large anisotropy and a positive ceramic  $\bar{Q}_{12}$  constant.

The larger value of the  $Q_{44}$  constant shown in Table I should better represent the actual  $Q_{44}$  of PbTiO<sub>3</sub>, since this value was determined from measurements on PbTiO<sub>3</sub>. This value will be used in calculating the piezoelectric coefficients later in the paper. When using this value, large ceramic anisotropy still resulted as shown in Table I. The electrostrictive constants of perovskite ferroelectrics have been experimentally shown to be only slightly temperature dependent,<sup>16,17</sup> and thus were assumed to be independent of temperature throughout this paper. However, since the magnitude of the  $\bar{Q}_{12}$  constant of ceramic PbTiO<sub>3</sub> is small, a slight temperature dependence of the single crystal electrostrictive constants could cause the ceramic  $\bar{Q}_{12}$  to go to zero and change signs as a function of temperature. This will be further discussed later in the paper when the electrostrictive anisotropy is related to the piezoelectric anisotropy.

An interesting result of this averaging procedure is that the ceramic hydrostatic electrostrictive constant ( $\bar{Q}_h = \bar{Q}_{11} + 2 \bar{Q}_{12}$ ) is equal to the single crystal  $Q_h$  when using either Equation (5) or (9), even though the magnitudes of the ceramic  $\bar{Q}_{11}$  and  $\bar{Q}_{12}$  coefficients are considerably lower than the single crystal values. The experimental ceramic  $\bar{Q}_h$  of BaTiO<sub>3</sub> is 3.3 ( $10^{-2} \text{ m}^4/\text{C}^2$ ) from the data in Table I, which is in fairly good agreement with the single crystal and predicted ceramic values of 2.3. However, even better agreement is found with ceramic  $\bar{Q}_h$ 's of 2.1 and 2.8 ( $10^{-2} \text{ m}^4/\text{C}^2$ ), which can be calculated from data in Reference 18 using the relation  $Q_h = - (d\theta/dP)/(2\epsilon_0 C)$ , where  $C$  is the Curie-Weiss constant and  $d\theta/dP$  is the slope of the pressure dependence of the Curie temperature ( $\theta$ ). A similar result also occurs when using these series and parallel models for the elastic constants. The ceramic volume compressibility is equal to that of the single crystal.

### 3. DIELECTRIC PERMITTIVITY

Parallel and series models were also used to calculate the upper and lower limits of the ceramic dielectric permittivity from the single crystal values:

$$\text{Parallel: } \bar{\epsilon} = (2/3)\epsilon_{11} + (1/3)\epsilon_{33} \quad (13)$$

$$\text{Series: } 1/\bar{\epsilon} = (2/3)/\epsilon_{11} + (1/3)/\epsilon_{33} \quad (14)$$

$\bar{\epsilon}$  is the ceramic permittivity, and  $\epsilon_{11}$  and  $\epsilon_{33}$  are the single crystal permittivities perpendicular and parallel to the polar axis, respectively (assumed to be equal to the dielectric susceptibilities).

The upper and lower limits of the ceramic permittivity were plotted versus temperature in Figure 2 using Equations (13) and (14) and the phenomenological calculations of the single crystal permittivities from Reference 8. Only a slight difference in the upper and lower limits was found, because of the small dielectric anisotropy of single crystal  $\text{PbTiO}_3$ . The experimental data (circular data points) plotted in this figure were calculated from the piezoelectric  $d_{33}$  and  $g_{33}$  data given in Reference 19 (and plotted later in this paper) for a ceramic  $\text{PbTiO}_3$  sample doped with 1.0 mole percent  $\text{MnO}_2$ . This experimental data is in good agreement with the predicted upper and lower bounds. Another experimental data point is plotted in this figure. This value was listed in a table in Reference 19 for the same composition measured at room temperature. The predicted upper and lower limits of the ceramic dielectric permittivity at 25°C are 105 and 96.5. These values were calculated from the single crystal  $\epsilon_{11}$  and  $\epsilon_{33}$  values of 124.4 and 66.6 from Reference 8.

### 4. SPONTANEOUS POLARIZATION

There are six possible directions for the polar axis in a tetragonal structure such as that of  $\text{PbTiO}_3$ . If an applied electric field causes all of the domains in a ceramic to align along the closest of these directions to the field, then the polarization of the ceramic ( $\bar{P}$ ) will be:  $\bar{P} = 0.831 P$ , where

$P$  is the single crystal polarization.<sup>20</sup> This gives the upper limit of the ceramic polarization by assuming that 1/6 of the domains did not require switching, 1/6 switched through  $180^\circ$ , and 2/3 through  $90^\circ$ .<sup>21</sup> However, Carl<sup>22</sup> found that, in dense  $\text{PbTiO}_3$  ceramics doped with small amounts of lanthanum and manganese, the  $180^\circ$  domain alignment was virtually perfect, but only about ten percent of the domains switched by  $90^\circ$ . By assuming that no  $90^\circ$  domain switching occurs and that only 1/6 of the domains realign through  $180^\circ$ ,  $\bar{P} = (1/3)(0.831)P = 0.277 P$ . This will be assumed to be the lower limit of the ceramic polarization. If  $90^\circ$  domain alignment does not occur, then the 2/3 of the domains that would ideally switch through  $90^\circ$  will instead possibly switch through  $180^\circ$ . If all of these domains switch through  $180^\circ$  then  $\bar{P} = 0.5 P$ . This result will be assumed to be the upper limit of the ceramic polarization.

The upper and lower limits of the spontaneous polarization of ceramic  $\text{PbTiO}_3$  are plotted in Figure 3 along with the single crystal polarization. Carl<sup>22</sup> found that the polarization of ceramic  $\text{PbTiO}_3$  was approximately  $0.3 \text{ C/m}^2$  at room temperature. This value falls between the calculated limits at  $25^\circ\text{C}$  of  $0.21$  and  $0.38 \text{ C/m}^2$  as shown in Figure 3.

## 5. PIEZOELECTRIC COEFFICIENTS

The piezoelectric voltage ( $g_{ij}$ ) and charge ( $d_{ij}$ ) coefficients of a single crystal of  $\text{PbTiO}_3$  are related to the electrostrictive constants, dielectric permittivities, and spontaneous polarization by the following equations<sup>23</sup>:

$$g_{33} = 2 Q_{11} P_3, \quad g_{31} = 2 Q_{12} P_3, \quad g_{15} = Q_{44} P_3 \quad (15)$$

$$d_{33} = 2 \epsilon_0 \epsilon_{33} Q_{11} P_3, \quad d_{31} = 2 \epsilon_0 \epsilon_{33} Q_{12} P_3, \quad d_{15} = \epsilon_0 \epsilon_{11} Q_{44} P_3 \quad (16)$$

These equations are based on the approximation that the dielectric susceptibilities  $\eta_{11}$  and  $\eta_{33}$  are equal to the dielectric permittivities  $\epsilon_{11}$  and  $\epsilon_{33}$ .

Equations (15) and (16) are single crystal relations and should probably not be used for ceramics. However, these equations can be used to determine the upper and lower limits of the ceramic piezoelectric coefficients from the limits of the ceramic electrostrictive constants, dielectric permittivities, and spontaneous polarization. For example:

$$\bar{g}_{33}^U = 2 \bar{Q}_{11}^U \bar{P}_3^U, \quad \bar{g}_{33}^L = 2 \bar{Q}_{11}^L \bar{P}_3^L, \quad (17)$$

where U and L refer to the upper and lower limits as defined in the previous sections. Similar equations were used to calculate the ceramic limits for the other piezoelectric constants. Since there was very little difference between the upper and lower limits of the ceramic  $\text{PbTiO}_3$  dielectric permittivity (see Figure 2), the average of the series and parallel models was used in the calculations of the piezoelectric  $d_{ij}$  constants. However, for a material such as  $\text{BaTiO}_3$  with a large dielectric anisotropy, the limits of the dielectric permittivity should also be accounted for.

Using this procedure the upper and lower limits of the piezoelectric coefficients were calculated and plotted versus temperature in Figure 4. The single crystal coefficients are also plotted in this figure for comparison along with experimental ceramic data. The values of the piezoelectric coefficients at 25°C are listed in Table II. The circular data points shown in Figures 1(a) and (d) were measured in Reference 19 on ceramic  $\text{PbTiO}_3$  doped with 1.0 mole percent  $\text{MnO}_2$ . This data falls between the predicted upper and lower limits with similar temperature dependences as the calculated curves. The diamond shaped data points shown in Figures 1(a), (b), (d), and (e) are also from Reference 19 for the same composition. The corresponding experimental dielectric data was previously shown in Figure 2. The experimental  $g_{31}$  and  $d_{31}$  coefficients also fall between the upper and lower limits. The square shaped data points shown in Figures 1(c) and (f) are from Reference 24 for ceramic  $\text{PbTiO}_3$  doped with 1.0 and 2.5 mole percent  $\text{MnO}_2$  and  $\text{LaO}_{3/2}$ , respectively. The experimental  $g_{15}$  coefficient of this composition falls between the limits, but the  $d_{15}$  coefficient was greater than the upper limit because of a larger dielectric permittivity (170) than that predicted. The difference between the ceramic and single crystal values of the  $g_{15}$  and  $d_{15}$

coefficients is smaller than that of the other coefficients, because the ceramic  $\bar{Q}_{44}$  constant is larger than the single crystal value.

From Equations (15) and (16) the piezoelectric anisotropy of a single crystal is found to be equal to the electrostrictive anisotropy:

$$g_{33}/g_{31} = d_{33}/d_{31} = Q_{11}/Q_{12} = -1/\sigma \quad (18)$$

This single crystal relation can be used to approximate the upper and lower limits of the ceramic piezoelectric anisotropy from the ceramic electrostrictive anisotropy by assuming that:

$$(\bar{g}_{33}/\bar{g}_{31})^U = \bar{g}_{33}^U/\bar{g}_{31}^U, \quad (\bar{g}_{33}/\bar{g}_{31})^L = \bar{g}_{33}^L/\bar{g}_{31}^L \quad (19)$$

Equations (10) and (11) and Figure 1 can then be used to predict the upper and lower bounds of the ceramic piezoelectric anisotropy from the single crystal electrostrictive anisotropies. From Table II, experimentally  $-\bar{g}_{31}/\bar{g}_{33} = 0.11$  for ceramic  $\text{PbTiO}_3$ . This value falls between the predicted ceramic  $-\bar{Q}_{12}/\bar{Q}_{11}$  bounds of 0.077 and 0.17 plotted in Figure 1 (listed in Table I as  $-Q_{11}/Q_{12}$ ). However, the experimental  $-\bar{g}_{31}/\bar{g}_{33}$  of  $\text{BaTiO}_3$  has a value of 0.41<sup>25</sup>, which does not fall between the predicted ceramic  $-\bar{Q}_{12}/\bar{Q}_{11}$  bounds of 0.19 and 0.31 (see Table I).

Equation 19 was based on the assumption that the boundary conditions are the same for the  $\bar{g}_{33}$  and  $\bar{g}_{31}$  coefficients. However, the boundary conditions might not be the same, and thus the following relations should probably be used to calculate the bounds of the piezoelectric anisotropies:

$$(\bar{g}_{33}/\bar{g}_{31})^U = \bar{g}_{33}^U/\bar{g}_{31}^L = (\bar{d}_{33}/\bar{d}_{31})^U = \bar{d}_{33}^U/\bar{d}_{31}^L = \bar{Q}_{11}^U/\bar{Q}_{12}^L \quad (20)$$

$$(\bar{g}_{33}/\bar{g}_{31})^L = \bar{g}_{33}^L/\bar{g}_{31}^U = (\bar{d}_{33}/\bar{d}_{31})^L = \bar{d}_{33}^L/\bar{d}_{31}^U = \bar{Q}_{11}^L/\bar{Q}_{12}^U \quad (21)$$

Since for a particular domain configuration in a ceramic the polarization  $\bar{P}_3$  and dielectric permittivity  $\bar{\epsilon}_{33}$  are the same in the  $\bar{d}_{33}$  and  $\bar{d}_{31}$  relations, they were assumed to cancel out of Equations 20 and 21. The electrostrictive anisotropies  $\bar{Q}_{11}^U/\bar{Q}_{12}^L$  and  $\bar{Q}_{11}^L/\bar{Q}_{12}^U$  result in wider limits than those plotted in Figure 1, and can be calculated from relations similar to Equations 10 and 11.

Using Equations 20 and 21 the experimental value of  $-\bar{g}_{31}/\bar{g}_{33}$  of BaTiO<sub>3</sub> (0.41) falls between the predicted  $-\bar{Q}_{11}/\bar{Q}_{12}$  limits of 0.11 and 0.52 (calculated using the values from Table I).

From Equations 20 and 21 the upper and lower limits of the ceramic piezoelectric anisotropy only depend on the electrostrictive anisotropy and are independent of the dielectric properties. However, from piezoelectric averaging equations Turik et al.<sup>3</sup> concluded that the low dielectric anisotropy of single crystal PbTiO<sub>3</sub> contributed to the large ceramic piezoelectric anisotropy. Using Wersing's<sup>4,5</sup> approach of combining Luchaninov's<sup>6</sup> averaging equations with single crystal relations (Equation 16), and then solving for the anisotropy, results in the following relation:

$$\frac{\bar{d}_{33}}{\bar{d}_{31}} = \frac{\frac{2 Q_{11}}{(1-\delta-1) Q_{12}} + \frac{\epsilon_{11} Q_{44}}{\epsilon_{33} Q_{12}} + 2}{\frac{Q_{11}}{Q_{12}} - \frac{\epsilon_{11} Q_{44}}{2 \epsilon_{33} Q_{12}} + \frac{1+\delta}{1-\delta}}, \quad (22)$$

where  $\delta = \langle \cos^3 \theta \rangle / \langle \cos \theta \rangle$ , and  $\theta$  is the angle between the direction of the spontaneous polarization of a crystallite and the direction of the poling field. Equation 22 indicates that if the single crystal dielectric anisotropy ( $\epsilon_{11}/\epsilon_{33}$ ) decreases, the ceramic piezoelectric anisotropy will increase. If  $\delta = 3/5$  and  $\epsilon_{11}/\epsilon_{33} = 1$ , then the right side of Equation 23 reduces to the electrostrictive series model (Equation 10) which gave the upper limit of the  $\sigma$  ratio and the lower limit of the ceramic electrostrictive anisotropy. This indicates that Luchaninov's<sup>6</sup> averaging equations may represent the lower limit of the ceramic piezoelectric anisotropy which would result from the upper limits of the piezoelectric coefficients. Averaging equations for the lower limits of the piezoelectric coefficients may show that the ceramic piezoelectric anisotropy will increase when the single crystal dielectric anisotropy increases, which is the opposite conclusion as that of the other limit. Thus between these limits there may be little effect on the ceramic piezoelectric anisotropy from the single crystal dielectric anisotropy.

Irrespective of the dielectric anisotropy and degree of polarization, the large ceramic piezoelectric anisotropy of  $\text{PbTiO}_3$  can be explained by the the large electrostrictive anisotropy which was shown in Section 2 to be due to the small magnitude of the ceramic  $\bar{Q}_{12}$  constant. Since the value the ceramic  $\bar{Q}_{12}$  is close to zero, the sign of  $\bar{Q}_{12}$  could easily change from a slight variation in the single crystal anisotropies. This could also cause the  $\bar{d}_{31}$  coefficient to change signs, and result in an infinite piezoelectric anisotropy when  $\bar{d}_{31}$  goes to zero.

The single crystal electrostrictive anisotropies of  $\text{PbTiO}_3$  can be varied by changing the composition and/or temperature. When some of the titanium in  $\text{PbTiO}_3$  is substituted with zirconium to form PZT, the single crystal  $-Q_{12}/Q_{11}$  ratio increases, while the  $-Q_{12}/Q_{44}$  ratio decreases. This causes the ceramic  $-\bar{Q}_{12}/\bar{Q}_{11}$  and  $-\bar{d}_{31}/\bar{d}_{33}$  ratios to increase (see Figure 1), which results in less anisotropy. Zorn et al.<sup>17</sup> experimentally found that  $-\bar{Q}_{12}/\bar{Q}_{11} = 0.5$  and  $-\bar{Q}_{12}/\bar{Q}_{44} = 0.3$  for the  $\text{Pb}_{0.83}\text{Sr}_{0.12}\text{Ba}_{0.05}(\text{Zr}_{0.6}\text{Ti}_{0.38}\text{Nb}_{0.02})\text{O}_3$  composition which is close to the morphotropic boundary. These values would result in a ceramic piezoelectric anisotropy ( $-\bar{d}_{33}/\bar{d}_{31}$ ) of 2 using either the series or parallel models, which is in good agreement with the measured piezoelectric anisotropies.<sup>1</sup>

Doping  $\text{PbTiO}_3$  with other elements, such as samarium or calcium, was shown to increase the anisotropy.<sup>2,26</sup> Large piezoelectric anisotropies have also been found for the  $\text{Pb}(\text{Zr}_{0.95}(\text{Mn}_{1/3}\text{Nb}_{2/3})_{0.05})\text{O}_3$  composition.<sup>27</sup> This suggests that the single crystal electrostrictive ratios in the PZT system change in such a way as to cause the anisotropy to increase when moving from the morphotropic boundary towards  $\text{PbZrO}_3$ , as occurs when going the other way to  $\text{PbTiO}_3$ .

From Equations (15) and (16) the hydrostatic piezoelectric voltage ( $g_h = g_{33} + 2g_{31}$ ) and strain ( $d_h = d_{33} + 2d_{31}$ ) coefficients of a single crystal can be calculated from the following relations:

$$g_h = 2 P_3 Q_h, \quad d_h = 2 \epsilon_0 \epsilon_{33} P_3 Q_h \quad (23)$$



These single crystal relations can also be used to predict the upper and lower bounds of the ceramic hydrostatic piezoelectric coefficients. By dividing the resulting equations for the ceramic bounds by the single crystal equations, and again realizing that for a particular domain configuration in a ceramic the polarization  $\bar{P}_3$  and dielectric permittivity  $\bar{\epsilon}_{33}$  are the same in the  $\bar{d}_{33}$  and  $\bar{d}_{31}$  equations, the following relations are obtained:

$$\frac{\bar{g}_h^L}{g_h} = \frac{\bar{P}_3}{P_3} \frac{\bar{Q}_h^L}{Q_h}, \quad \frac{\bar{g}_h^U}{g_h} = \frac{\bar{P}_3}{P_3} \frac{\bar{Q}_h^U}{Q_h} \quad (24)$$

$$\frac{\bar{d}_h^L}{d_h} = \frac{\bar{\epsilon}_{33}}{\epsilon_{33}} \frac{\bar{P}_3}{P_3} \frac{\bar{Q}_h^L}{Q_h}, \quad \frac{\bar{d}_h^U}{d_h} = \frac{\bar{\epsilon}_{33}}{\epsilon_{33}} \frac{\bar{P}_3}{P_3} \frac{\bar{Q}_h^U}{Q_h} \quad (25)$$

Due to possibility of having different boundary conditions for the  $\bar{Q}_{11}$  and  $\bar{Q}_{12}$  constants, the limits of the hydrostatic electrostrictive constant should be calculated from the following relations:

$$\bar{Q}_h^L = \bar{Q}_{11}^L + 2 \bar{Q}_{12}^U, \quad \bar{Q}_h^U = \bar{Q}_{11}^U + 2 \bar{Q}_{12}^L \quad (26)$$

However, if the boundary conditions of  $\bar{Q}_{11}$  and  $\bar{Q}_{12}$  are the same, then the upper and lower limits of  $\bar{Q}_h$  would be equal to the single crystal  $Q_h$  (as described in Section 2). The values of the single crystal and ceramic  $Q_h$ 's of  $\text{BaTiO}_3$  are in fairly good agreement. Thus if the single crystal and ceramic  $Q_h$ 's are assumed to be equal, then from Equation 24 the ratio of the ceramic  $g_h$  divided by the single crystal  $g_h$  only depends on the ratio of the ceramic polarization divided by the single crystal polarization. Since the polarization of a ceramic is always lower than that of the single crystal, the value of the ceramic  $\bar{g}_h$  should be lower than the  $g_h$  of the single crystal. Experimentally, this is found in both  $\text{PbTiO}_3$  and  $\text{BaTiO}_3$ .

The ratio of  $\bar{d}_h$  coefficients would depend on the ratio of the ceramic  $\bar{\epsilon}_{33}$  divided by the single crystal  $\epsilon_{33}$ , in addition to the degree of poling. For a material such as  $\text{PbTiO}_3$  with a small dielectric anisotropy, the value of the ceramic  $\bar{d}_h$  should be lower than the  $d_h$  of the single crystal. Experimentally,  $\text{PbTiO}_3$  has a  $\bar{d}_h/d_h$  ratio of 0.46. However, Equation 25 predicts that a material

with a large dielectric anisotropy ( $\bar{\epsilon}_{11}/\bar{\epsilon}_{33}$ ) such as  $\text{BaTiO}_3$  could have a larger ceramic  $\bar{d}_h$  than the corresponding single crystal  $d_h$ . Experimentally,  $\text{BaTiO}_3$  has a ceramic  $\bar{d}_h$  value of approximately twice the single crystal value.<sup>25</sup> These results may be important in the design of materials for hydrostatic transducer applications, such as when a piezoelectric powder is dispersed in a polymer<sup>28</sup>. The properties of this type of composite will depend on the composition of the powder used and whether the powder is composed of single domain or multi-domain particles.

## SUMMARY

The upper and lower limits of the electrostrictive constants, dielectric permittivity, spontaneous polarization, and piezoelectric coefficients were calculated for ceramic  $\text{PbTiO}_3$  from theoretical single crystal constants. The ceramic was assumed to be composed of a large number of small single crystals with all possible orientations. The ceramic properties were calculated from the space averages of the single crystal constants, assuming that only  $180^\circ$  domain switching occurs. The experimental ceramic data was shown to be within the predicted upper and lower limits. Additional comparisons have been made between the theoretical predictions and low temperature dielectric and piezoelectric measurements on samarium doped lead titanate ceramics.<sup>29</sup>

The series and parallel equations used to calculate the upper and lower limits were used to derive relations that showed how the ceramic electrostrictive anisotropy ( $\bar{Q}_{11}/\bar{Q}_{12}$ ) depends on the single crystal electrostrictive anisotropies ( $Q_{11}/Q_{12}$  and  $Q_{44}/Q_{12}$ ). These relations can be used for any fourth rank tensor with similar tensor to matrix conversion, such as the elastic constants. The ceramic piezoelectric anisotropy ( $\bar{d}_{33}/\bar{d}_{31}$ ) was also shown to be related to the ceramic electrostrictive anisotropy.  $\text{PbTiO}_3$  was shown to have a large piezoelectric anisotropy, because of the large electrostrictive anisotropy which was due to the small magnitude of the ceramic  $\bar{Q}_{12}$  constant. Since the value the ceramic  $\bar{Q}_{12}$  is close to zero, the sign of  $\bar{Q}_{12}$  could easily change from a slight variation in the single crystal anisotropies due to a temperature dependence or modification

of the composition. This would also cause the  $\bar{d}_{31}$  coefficient to change signs, and result in an infinite piezoelectric anisotropy when  $\bar{d}_{31}$  goes to zero.

Damjanovic et al.<sup>30</sup> found that in calcium or samarium modified  $\text{PbTiO}_3$  ceramics the  $\bar{d}_{31}$  coefficient changes sign from negative values at low temperatures to positive values at high temperatures. They showed that this change in sign was due to a positive extrinsic contribution to  $\bar{d}_{31}$  that may dominate the negative intrinsic contribution. They also found that in samarium doped  $\text{PbTiO}_3$  samples poled with low electric fields a positive  $\bar{d}_{31}$  coefficient resulted over all of the temperature range tested (down to  $-180^\circ\text{C}$ ). If the  $\bar{d}_{31}$  coefficient remains positive at low temperatures where the extrinsic contributions have "frozen out", then the intrinsic  $\bar{d}_{31}$  may have increased to zero and become positive at low temperatures. They also found that as the poling field was increased the  $d_{31}$  versus temperature curves shifted to lower values (more negative). The amount of  $90^\circ$  domain switching increases as the poling field is increased causing the intrinsic ceramic anisotropy to decrease toward that of the single crystal. This would cause the intrinsic  $\bar{d}_{31}$  to shift to lower values approaching the single crystal value as the poling field is increased and would possibly explain the poling dependence that Damjanovic et al.<sup>30</sup> found.

The single crystal and ceramic hydrostatic electrostrictive constants were found to be equal when using either the series or parallel models. Using this result the ratio of the ceramic to single crystal hydrostatic  $g_h$  coefficients ( $\bar{g}_h/g_h$ ) was found to only depend on the degree of polarization ( $\bar{P}/P$ ). The  $\bar{d}_h/d_h$  ratio was found to depend on the ceramic to single crystal dielectric ratio  $\bar{\epsilon}_{33}/\epsilon_{33}$ , in addition to the degree of poling. The ceramic  $\bar{d}_h$  could be less than the single crystal  $d_h$  as is always true for the  $\bar{g}_h$  coefficients, or could be larger depending on the dielectric anisotropy ( $\epsilon_{11}/\epsilon_{33}$ ) of the single crystal.

The averaging procedure described in this paper provides a simple method of predicting the upper and lower bounds of the intrinsic ceramic properties from the single crystal constants. This procedure could also be used to determine single crystal constants from the ceramic properties. Pan

and Cross<sup>31</sup> have recently used the electrostrictive averaging equations to determine the single crystal  $Q_{44}$  constant of  $\text{Pb}(\text{Mg}_{1/3}\text{Nb}_{2/3})\text{O}_3$  from the measured single crystal and ceramic  $Q_{11}$  and  $Q_{12}$  constants. These equations may also be useful in determining the compositional dependence of the single crystal electrostrictive constants in the PZT system.

#### ACKNOWLEDGEMENTS

The authors wish to thank Dr. R. E. Newnham for helpful discussions concerning the averaging of the electrostrictive constants, and Dr. D. Damjanovic for discussions on the results of his measurements on modified lead titanate ceramics.

## REFERENCES

1. B. Jaffe, W. J. Cook, and H. Jaffe, *Piezoelectric Ceramics*, London: Academic Press, 1971.
2. H. Takeuchi, S. Jyomura, E. Yamamoto, and Y. Ito, "Electromechanical Properties of (Pb, Ln) (Ti, Mn) O<sub>3</sub> Ceramics (Ln = rare earths)", *J. Acoust. Soc. Am.*, vol. 72, no. 4 pp. 1114-1120, 1982.
3. A. V. Turik, E. G. Fesenko, V. G. Gavril'yachenko, and G. I. Khasabova, "Anisotropy of the Dielectric and Piezoelectric Properties of Lead Titanate", *Kristallografiya*, vol. 19, pp. 1095-1097, 1974; *Sov. Phys. - Cryst.*, vol. 19, pp. 677-678, 1974.
4. W. Wersing, G. Zorn, K. Lubitz, and J. Mohaupt, "Comparison of Piezoelectric Constants of PZT Ceramics with Values Calculated from Electrostrictive Coefficients", *Jpn. J. Appl. Phys.*, vol. 24, supplement 24-2, pp. 721-723, 1985.
5. W. Wersing, K. Lubitz, and J. Mohaupt, "Anisotropic Piezoelectric Effect in Modified PbTiO<sub>3</sub> Ceramics", Presented at the 6th IEEE International Symposium on the Applications of Ferroelectrics, Lehigh, PA, 1986.
6. A. G. Luchaninov, A. V. Shil'nikov, and L. A. Shuvalov, "On the Piezoelectric Effect in Acentric Ferroelectrics Ceramics with Zero Polarization", vol. 41, pp. 181-187, 1982.
7. A. F. Devonshire, "Theory of Barium Titanate - Part II", *Phil. Mag.*, vol. 42, no. 333, pp. 1065-1079, 1951.
8. M. J. Haun, E. Furman, S. J. Jang, H. A. McKinstry, and L. E. Cross, "Thermodynamic Theory of PbTiO<sub>3</sub>", *J. Appl. Phys.*, submitted.
9. R. F. S. Hearmon, "An Introduction to Applied Anisotropic Elasticity", Oxford: Oxford University Press, pp. 41-44, 1961.
10. A. F. Devonshire, "Theory of Ferroelectrics", *Advances in Physics*, vol. 3, no. 10, pp. 85-130, 1954.

11. W. J. Merz, "Double Hysteresis Loop of  $\text{BaTiO}_3$  at the Curie Point", *Phys. Rev.*, vol. 91, no. 3, pp. 513-517, 1953.
12. F. Jona and G. Shirane, *Ferroelectric Crystals*, New York: Pergamon Press, Inc., pp. 145-147, 1962.
13. D. Berlincourt and J. Jaffe, "Elastic and Piezoelectric Coefficients of Single-Crystal Barium Titanate", *Phys. Rev.*, vol. 111, no. 1, pp. 143-148, 1958.
14. G. Schmidt, "Bestimmung der Electrostriktionskonstanten  $Q_{11}$  von Bariumtitanatkeramik", *Z. Physik*, vol. 145, pp. 534-542, 1956.
15. M. J. Haun, Z. Q. Zhuang, S. J. Jang, H. A. McKinstry, and L. E. Cross, "A Phenomenological Theory for the Second Order Region of the PZT Solid Solution System", *Proc. of the 6th IEEE International Symposium on the Applications of Ferroelectrics*, Lehigh, PA, pp. 398-401, 1986.
16. S. J. Jang, *Electrostrictive Ceramics for Transducer Applications*, Ph.D. Thesis, The Pennsylvania State University, 1979; K. Uchino, S. Nomura, L. E. Cross, S. J. Jang, and R. E. Newnham, "Electrostriction Effect in Magnesium Niobate Single Crystals", *J. Appl. Phys.*, vol. 51, no. 2, pp. 1142-1145, 1980.
17. G. Zorn, W. Wersing, and H. Gobel, "Electrostrictive Tensor Components of PZT-Ceramics Measured by X-ray Diffraction", *Jpn. J. App. Phys.*, vol. 24, supplement 24-2, pp. 721-723, 1985.
18. G. A. Samara, "Pressure and Temperature Dependences of the Dielectric Properties of the Perovskites  $\text{BaTiO}_3$  and  $\text{SrTiO}_3$ ", *Phys. Rev.*, vol. 151, no. 2, pp. 378-386, 1966.
19. I. Ueda, "Effects of Additives on Piezoelectric and Related Properties of  $\text{PbTiO}_3$ ", *Jpn. J. App. Phys.*, vol. 11, no. 4, pp. 450-462, 1972.
20. H. G. Baerwald, "Thermodynamic Theory of Ferroelectric Ceramics", *Phys. Rev.*, vol. 105, no. 2, pp. 480-486, 1957.

21. D. Berlincourt and H. A. Krueger, "Domain Processes in Lead Titanate Zirconate and Barium Titanate Ceramics", *J. Appl. Phys.*, vol. 30, no. 11, pp. 1804-1810, 1959.
22. K. Carl, "Ferroelectric Properties and Fatiguing Effects of Modified  $\text{PbTiO}_3$  Ceramics", *Ferroelectrics*, vol. 9, pp. 23-32, 1975.
23. A. Amin, M. J. Haun, B. Badger, H. A. McKinstry, and L. E. Cross, "A Phenomenological Gibbs Function for the Single Cell Region of the  $\text{PbZrO}_3\text{:PbTiO}_3$  Solid Solution System", *Ferroelectrics*, vol. 65, pp. 107-130, 1985.
24. S. Ikegami, I. Ueda, and T. Nagata, "Electromechanical Properties of  $\text{PbTiO}_3$  Ceramics Containing La and Mn", *J. Acoustical Soc. Amer.*, vol. 50, no. 4, pp. 1060-1066, 1971.
25. K. H. Hellwege, Landolt-Bornstein, Numerical Data and Functional Relationships in Science and Technology, New Series, Group III, Crystal and Solid State Physics, vol. 16, *Ferroelectrics and Related Substances, Subvolume a, Oxides*, Berlin, Heidelberg, New York: Springer-Verlag, p. 73, 1981.
26. D. Damjanovic, T. R. Gururaja, S. J. Jang, and L. E. Cross, "Temperature Behavior of the Complex Piezoelectric  $d_{31}$  Coefficient in Modified Lead Titanate Ceramics", *Materials Letters*, vol. 4, pp. 414-419, 1986.
27. H. Takeuchi, S. Jyomura, C. Nakaya, "New Piezoelectric Materials for Ultrasonic Transducers", *Jpn. J. App. Phys.*, vol. 24, supplement 24-2, pp. 36-40, 1985.
28. Y. H. Lee, M. J. Haun, A. Safari, and R. E. Newnham, "Preparation of  $\text{PbTiO}_3$  Powder for a Flexible 0-3 Piezoelectric Composite", *Proc. of the 6th IEEE International Symposium on the Applications of Ferroelectrics*, Lehigh, PA, pp. 318-321, 1986.
29. J. N. Kim, M. J. Haun, S. J. Jang, L. E. Cross, and W. R. Xue, "Temperature Behavior of Dielectric and Piezoelectric Properties of Samarium Doped Lead Titanate Ceramics", *Trans. IEEE Ultrasonics, Ferroelectrics, and Frequency Control Soc.*, submitted.

30. D. Damjanovic, T. R. Gururaja, S. J. Jang, and L. E. Cross, "Possible Mechanisms for the Electromechanical Anisotropy in Modified Lead Titanate Ceramics", Proc. IEEE Ultrasonics Symposium, Williamsburg, VA, Nov. 17-19, 1986.
31. W. Pan and L. E. Cross, "Direct and Converse Electrostrictive Effects in  $\text{Pb}(\text{Mg}_{1/3}\text{Nb}_{2/3})\text{O}_3$  Ceramics", (to be published).



## TABLE CAPTIONS

TABLE I Electrostrictive Constants and Anisotropies of  $\text{BaTiO}_3$  and  $\text{PbTiO}_3$

TABLE II The Piezoelectric Coefficients of Ceramic  $\text{PbTiO}_3$  at  $25^\circ\text{C}$

TABLE I

Electrostrictive Constants and Anisotropies of BaTiO<sub>3</sub> and PbTiO<sub>3</sub>

	$(10^{-2} \text{ m}^4/\text{C}^2)$			$-\frac{Q_{11}}{Q_{12}}$	$-\frac{Q_{44}}{Q_{12}}$
	$\underline{Q_{11}}$	$\underline{Q_{12}}$	$\underline{Q_{44}}$		
BaTiO <sub>3</sub>					
Single Crystal	11.1 <sup>a</sup>	-4.42 <sup>a</sup>	5.85 <sup>a</sup>	2.5	1.3
Ceramic					
Series: Eq. (5)	6.06	-1.90	15.9	3.2	8.4
Parallel: Eq. (9)	3.64	-0.690	8.66	5.3	12.6
Experimental	5.76 <sup>b</sup>	-1.24 <sup>b</sup>	14.0 <sup>c</sup>	4.6	11.3
PbTiO <sub>3</sub>					
Single Crystal	8.9 <sup>d</sup>	-2.6 <sup>d</sup>	6.75 <sup>e</sup>	3.4	2.6
Ceramic					
Series: Eq. (5)	5.65	-0.975	13.25	5.8	13.6
Parallel: Eq. (9)	4.37	-0.335	9.41	13.0	28.1
Single Crystal	8.9 <sup>d</sup>	-2.6 <sup>d</sup>	2.0 <sup>f</sup>	3.4	0.77
Ceramic					
Series: Eq. (5)	4.70	-0.500	10.4	9.4	20.8
Parallel: Eq. (9)	2.28	0.708	3.15	-3.2	-4.4

<sup>a</sup> Calculated from the spontaneous polarization (0.26 C/m<sup>2</sup>) and piezoelectric g<sub>ij</sub> data from Reference 13.<sup>b</sup> From Reference 14.<sup>c</sup> Calculated from Equation (7).<sup>d</sup> From Reference 8.<sup>e</sup> From Reference 3.<sup>f</sup> From Reference 15.

TABLE II

The Piezoelectric Coefficients of Ceramic  $\text{PbTiO}_3$  at  $25^\circ\text{C}$ 

<u>Coefficient</u>	<u>Lower Limit</u>	<u>Experimental</u>	<u>Upper Limit</u>
$g_{33} (10^{-3} \text{ Vm/N})$	18.3	$33^a (38^b)$	42.6
$g_{31} (10^{-3} \text{ Vm/N})$	-1.40	$-3.5^a$	-7.36
$g_{15} (10^{-3} \text{ Vm/N})$	19.7	$27^c$	50.0
$d_{33} (10^{-12} \text{ C/N})$	16.3	$39^a (34^b)$	38.0
$d_{31} (10^{-12} \text{ C/N})$	-1.25	$-4.2^a$	-6.57
$d_{15} (10^{-12} \text{ C/N})$	17.6	$53^c$	44.6

<sup>a</sup>Diamond shaped data points in Fig. 4 (doped with 1.0 mole% Mn, from Ref. 19).<sup>b</sup>Circular shaped data points in Fig. 4 (doped with 1.0 mole% Mn, from Ref. 19).<sup>c</sup>Square shaped data points in Fig. 4 (doped with 1.0 and 2.5 mole% Mn and La, from Ref. 24)

## FIGURE CAPTIONS

- Figure 1. The ceramic  $\bar{\sigma}$  ratio plotted versus the single crystal  $\sigma$  ratio for different values of the single crystal  $\mu$  ratio calculated from a) the series model using Equation (10) and b) the parallel model using Equation (11). The square shaped data points correspond to  $\text{BaTiO}_3$ , the circular shaped to the first set of  $\text{PbTiO}_3$  data in Table I, and the triangular shaped to the second set of  $\text{PbTiO}_3$  data.
- Figure 2. The dielectric susceptibility plotted versus temperature for ceramic  $\text{PbTiO}_3$ . The data points are experimental measurements from Reference 19.
- Figure 3. The spontaneous polarization of  $\text{PbTiO}_3$  plotted versus temperature. The dashed curve is the single crystal polarization calculated from phenomenological theory in Reference 8. The solid curves represent approximations of the upper ( $= 0.5 \text{ P}$ ) and lower ( $= 0.277 \text{ P}$ ) limits of the ceramic polarization. The data point is from Reference 22.
- Figure 4. The piezoelectric voltage ( $g_{ij}$ ) and charge ( $d_{ij}$ ) coefficients plotted versus temperature for  $\text{PbTiO}_3$ . The dashed curves are the theoretical single crystal coefficients calculated from phenomenological theory in Reference 8. The solid curves A and B are the upper and lower bounds of the ceramic coefficients calculated using Equation (17) for  $g_{33}$  and similar equations for the remaining coefficients. The data points are experimental measurements from References 19 and 24.

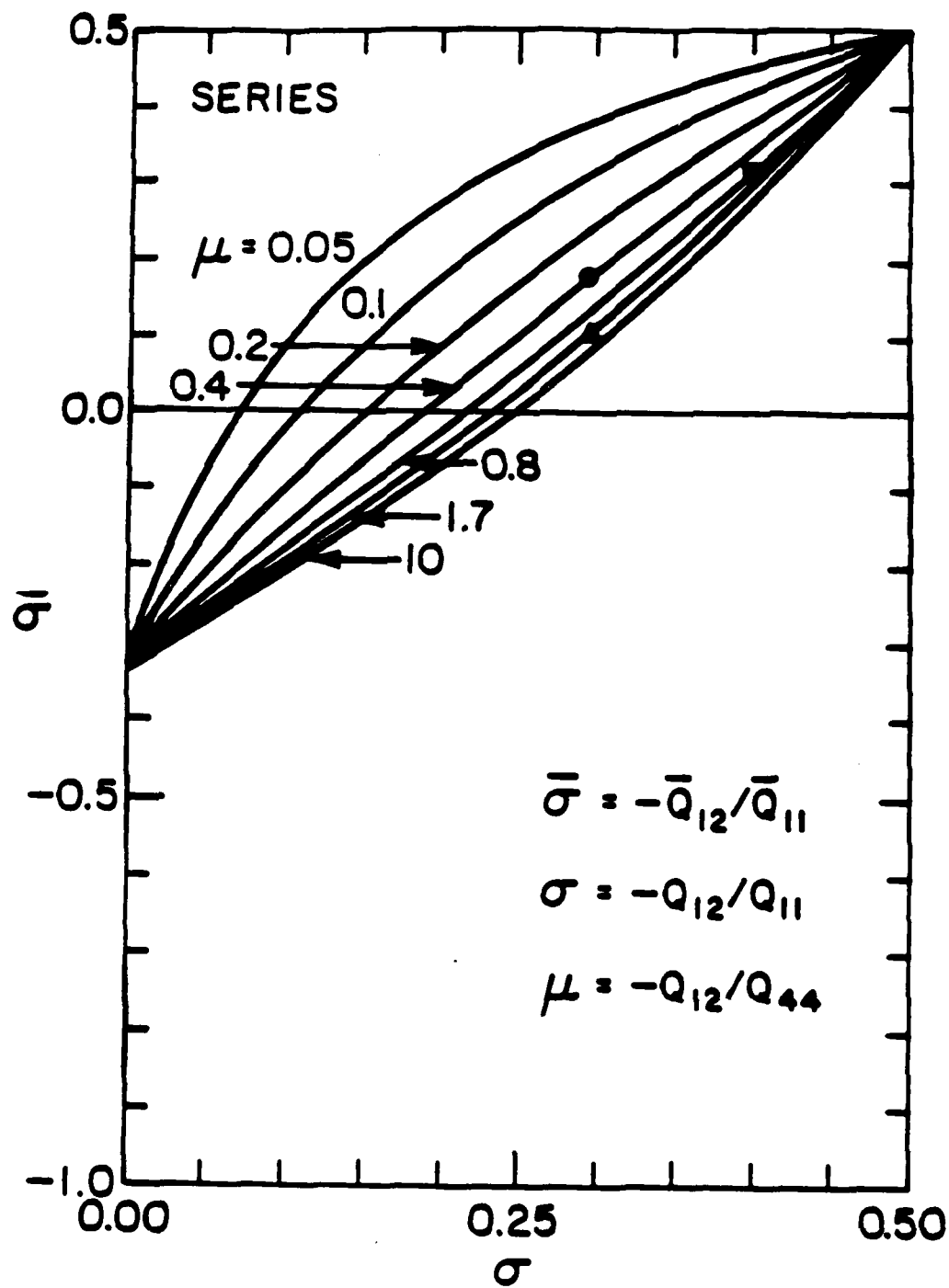


Figure 1(a)

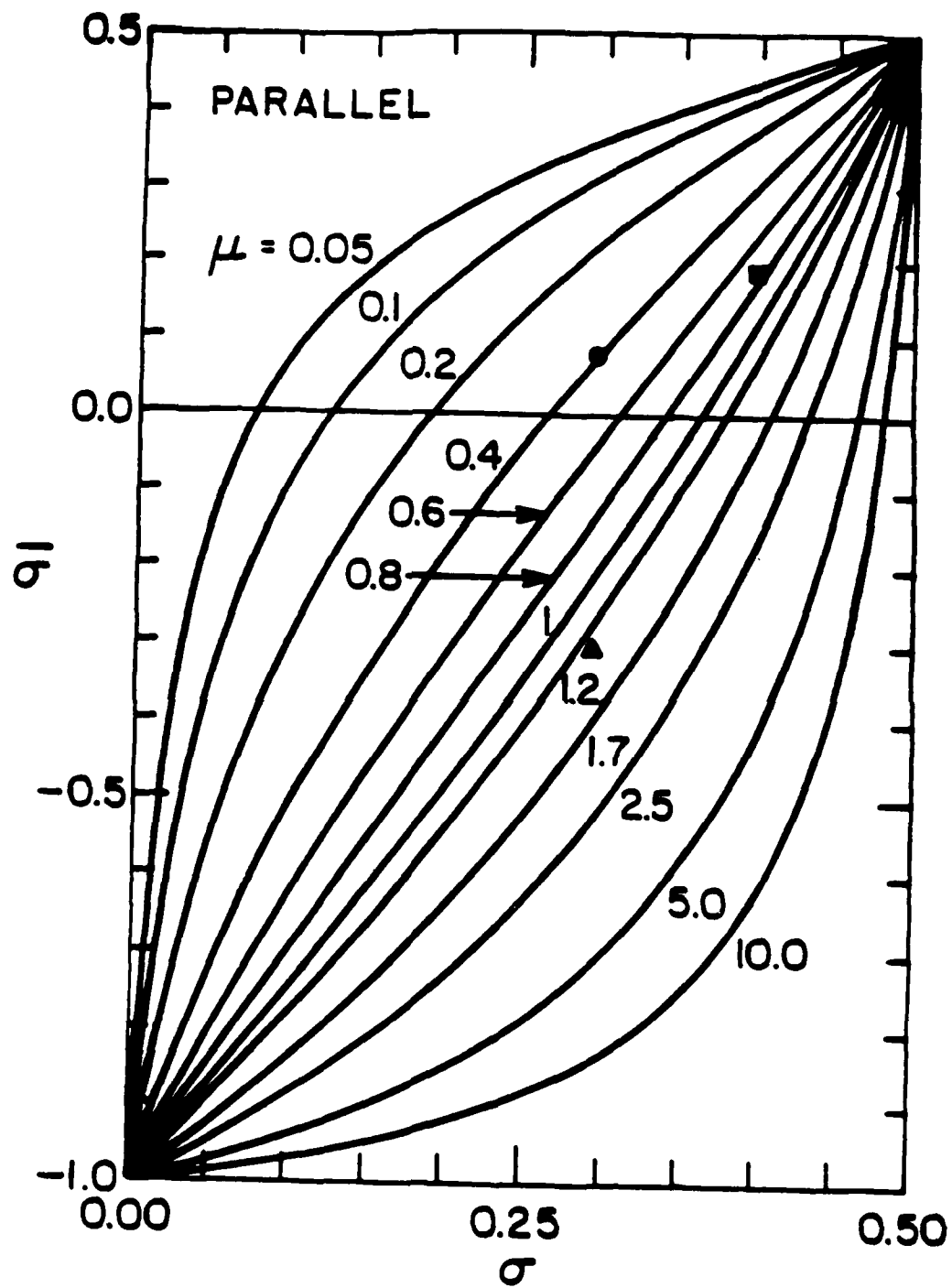


Figure 1(b)

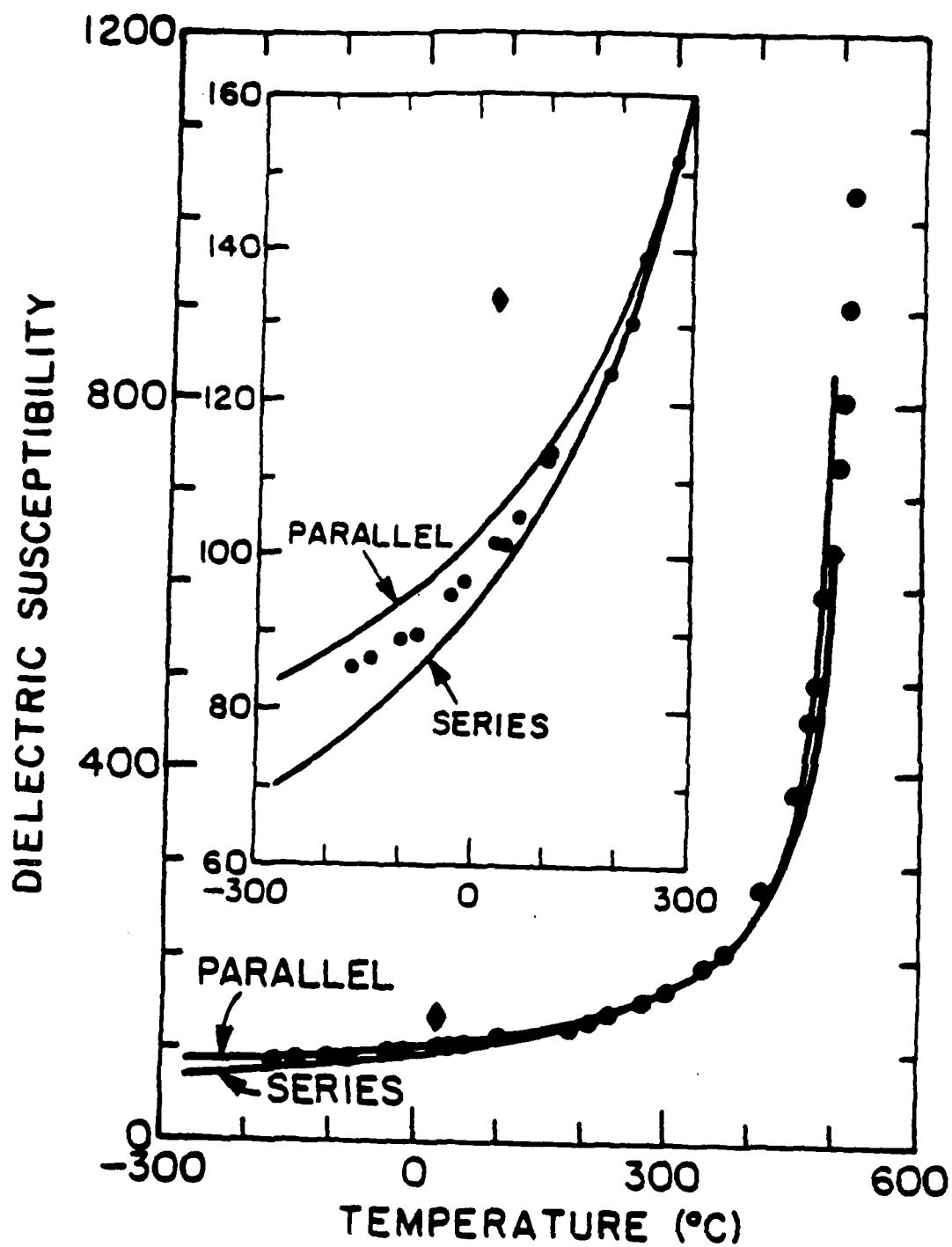


Figure 2

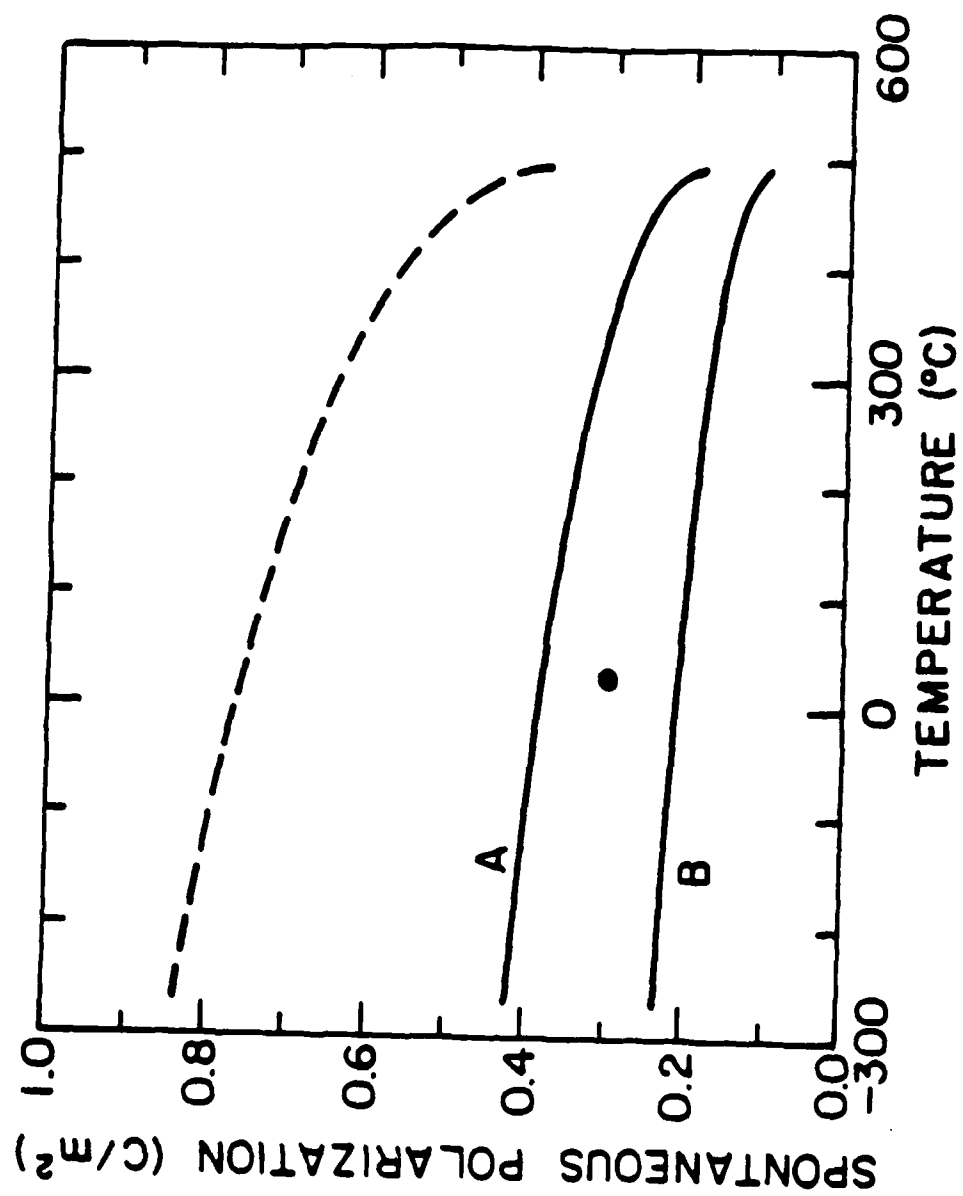


Figure 3



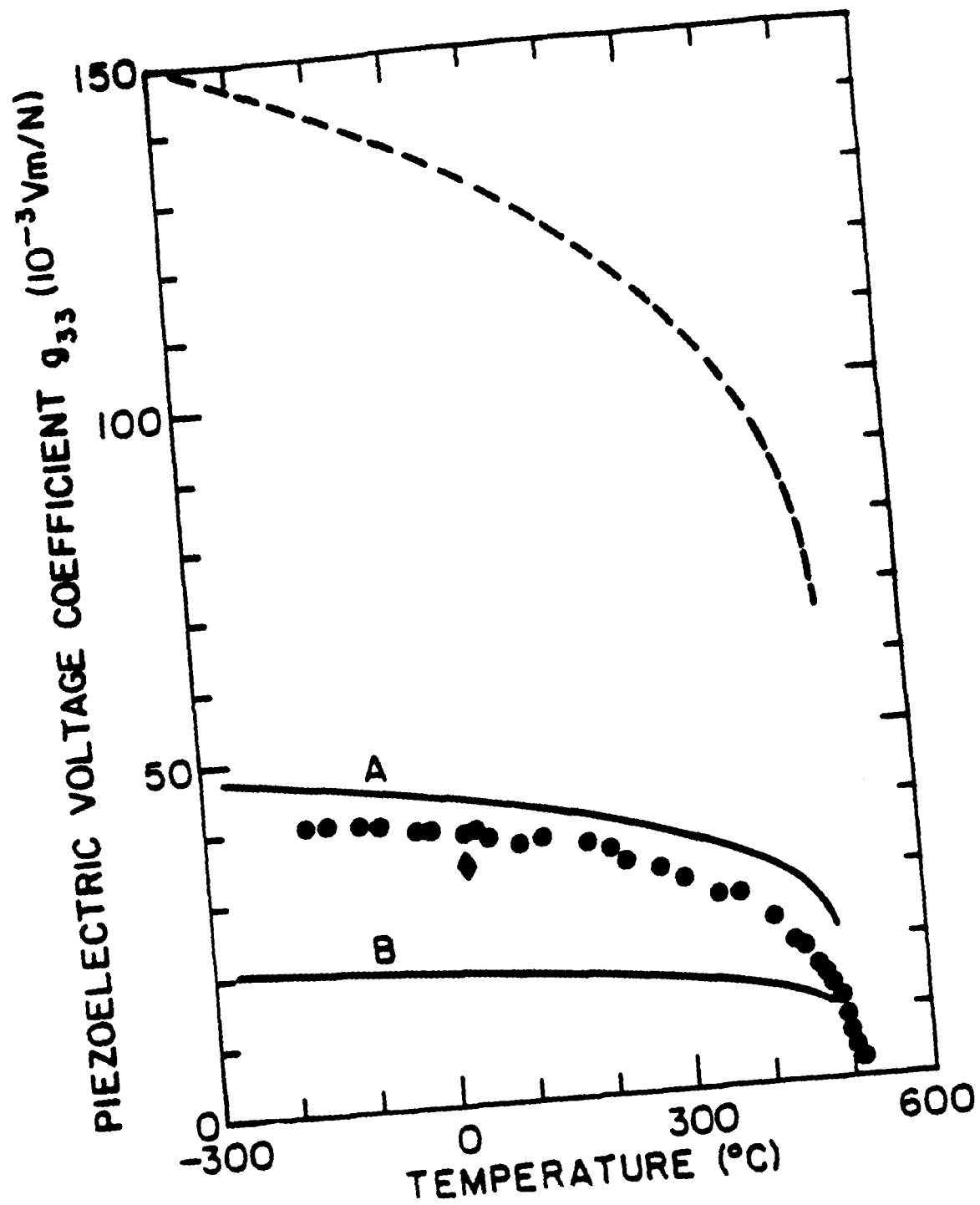


Figure 4(a)

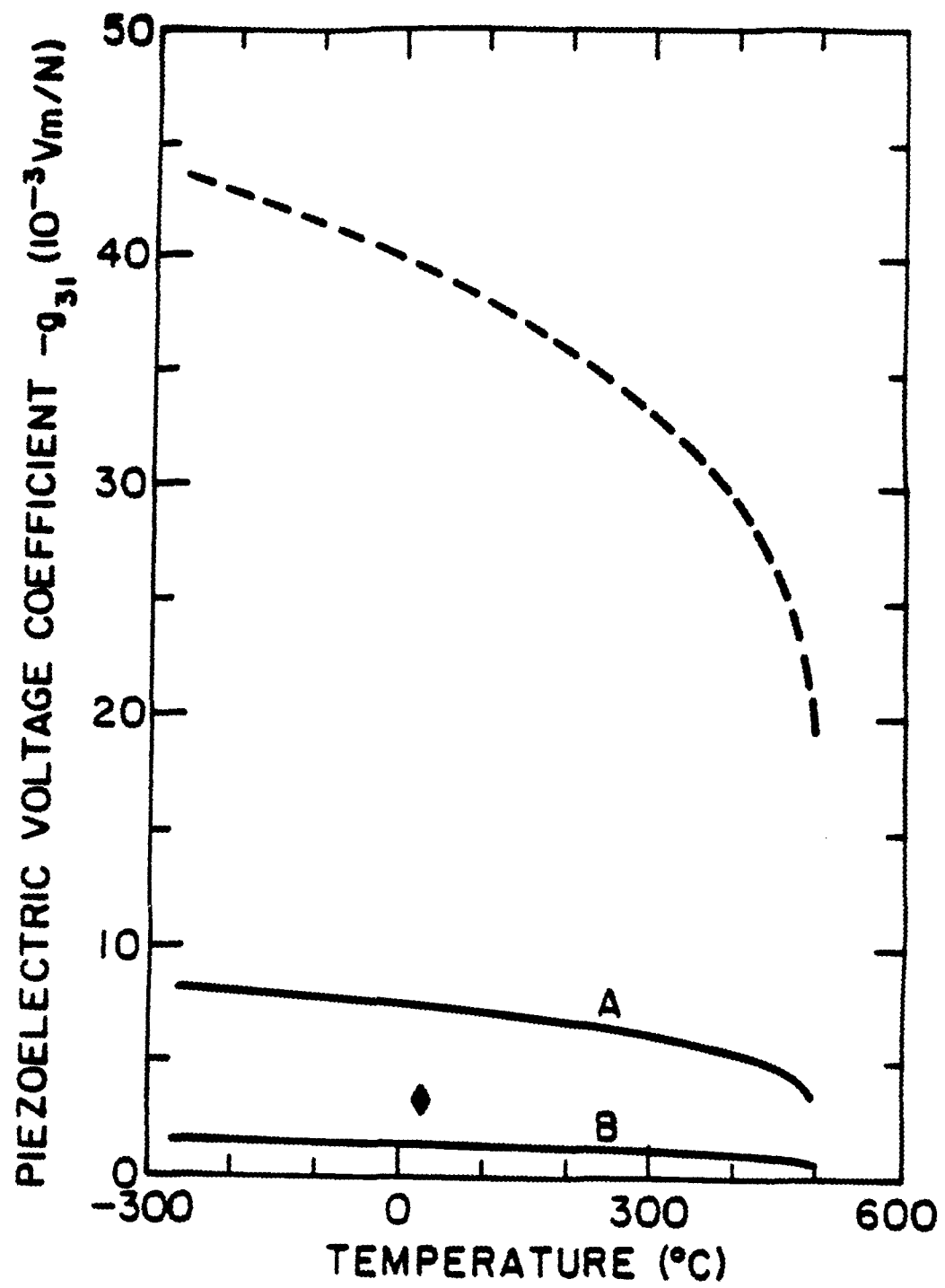


Figure 4(b)

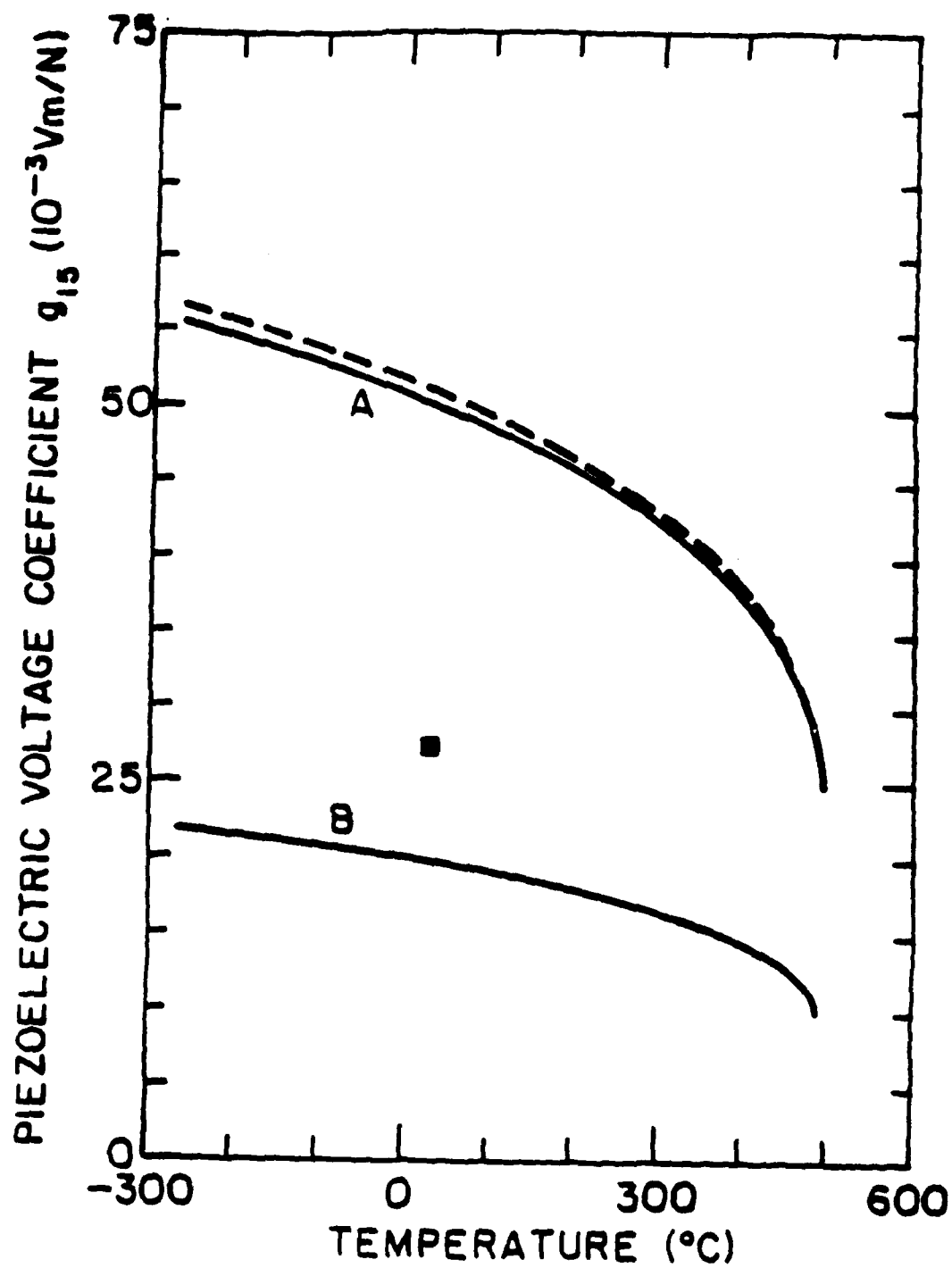


Figure 4(c)

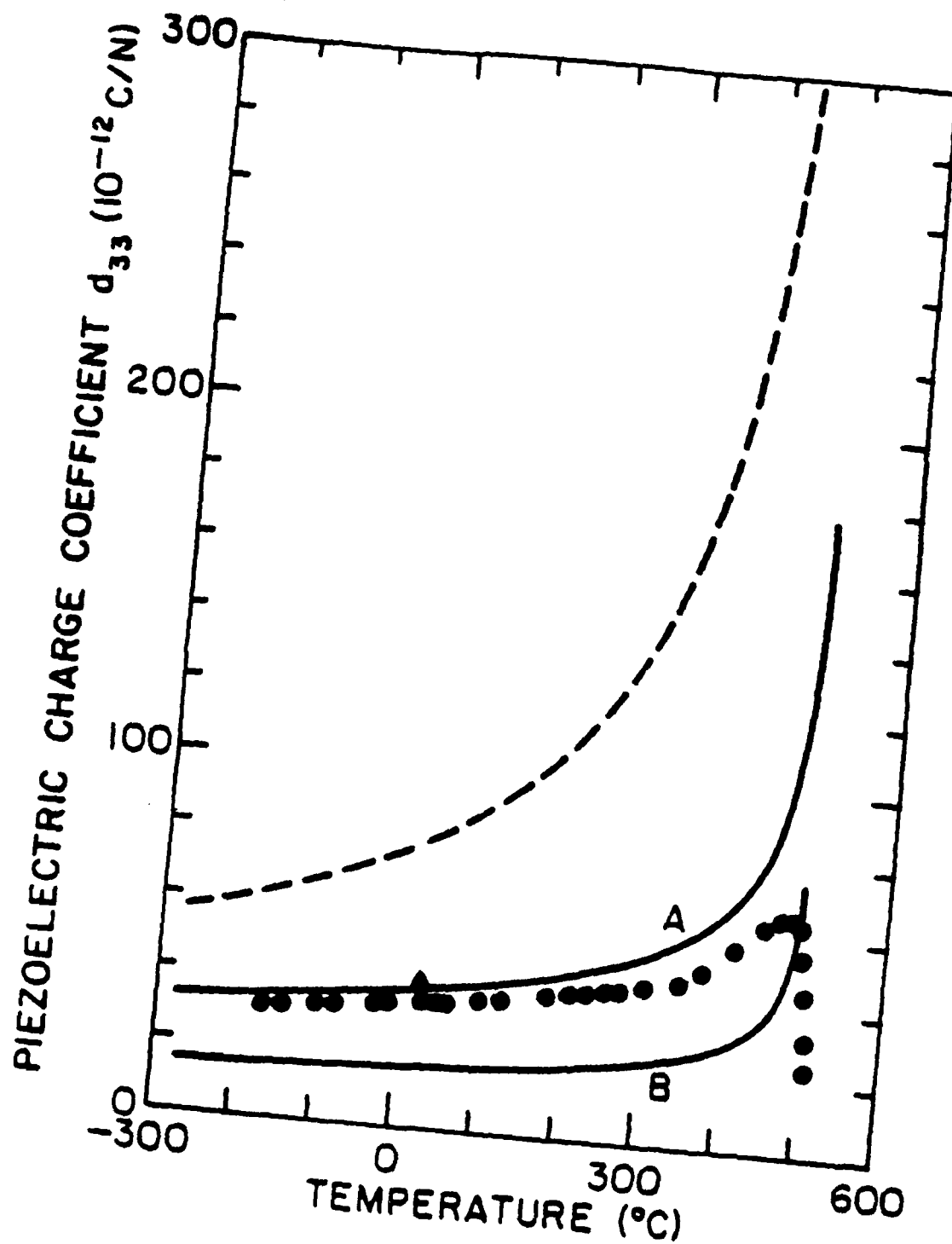


Figure 4(d)

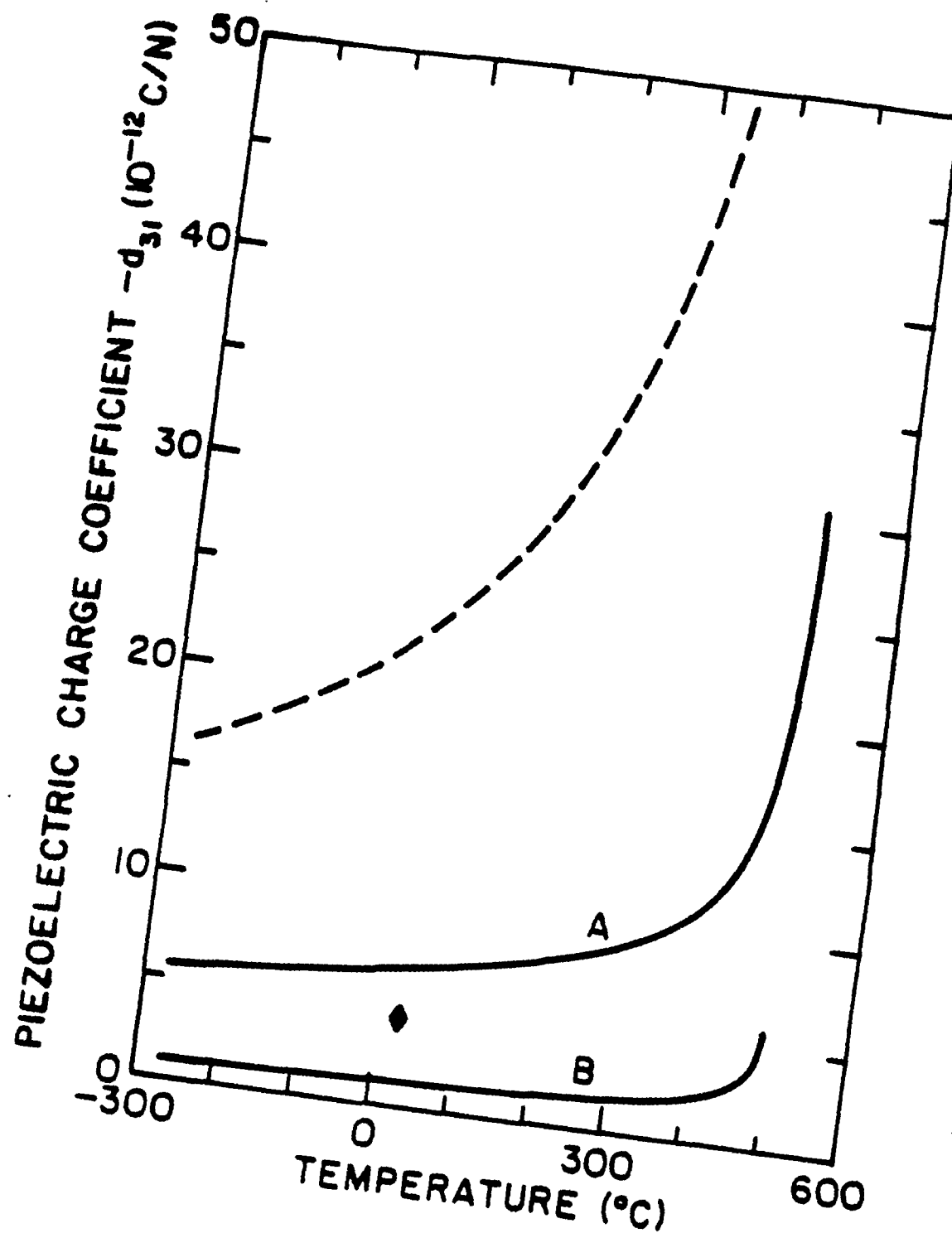


Figure 4(e)

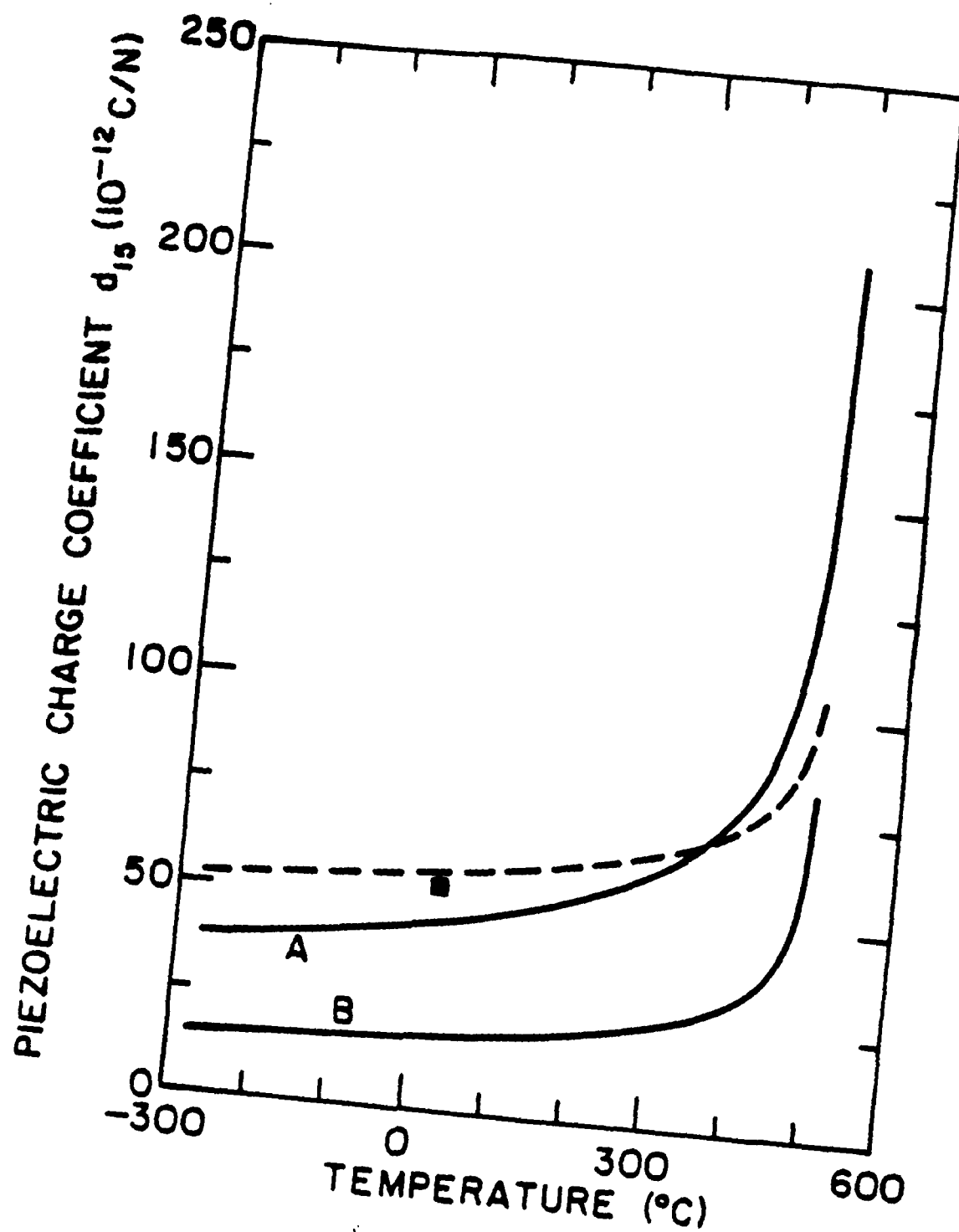


Figure 4(f)

## ELECTROSTRICTIVE PROPERTIES OF THE LEAD ZIRCONATE-TITANATE SOLID SOLUTION SYSTEM

M. J. Haun, Z. Q. Zhuang<sup>†</sup>, E. Furman<sup>††</sup>, S. J. Jang, and L. E. Cross

Materials Research Laboratory  
The Pennsylvania State University  
University Park, PA 16802

Values of the electrostrictive constants for the lead zirconate-titanate (PZT) solid solution system were required to complete the development of a thermodynamic phenomenological theory of PZT. The electrostrictive  $Q_{12}$  constant was measured as a function of composition on polycrystalline ceramic PZT samples. This data was used with additional single-crystal and ceramic data from the literature to approximate the compositional dependence of the electrostrictive constants of the PZT system. Series and parallel equations, analogous to the Voigt and Reuss models for the elastic constants, were used to relate the ceramic and single-crystal data, and to predict the upper and lower bounds of the ceramic electrostrictive constants from the single-crystal constants.

<sup>†</sup>Visiting Scientist from the Department of Inorganic Materials Science and Engineering, South China Institute of Technology, Guangzhou, The People's Republic of China.

<sup>††</sup>Now at Allied-Signal Inc., Morristown, NJ 07960.

## I. INTRODUCTION

Compositions in the lead zirconate-titanate (PZT) solid solution system have been widely used in piezoelectric transducer applications in polycrystalline ceramic form.<sup>1</sup> However, considerable difficulty has been encountered when attempting to grow single crystals of PZT.<sup>2</sup> Without single-crystal data indirect methods have been required to determine the coefficients of a thermodynamic energy function for the PZT system.<sup>3,4</sup>

In one particularly important indirect method, spontaneous strain and electrostrictive data were used to calculate the spontaneous polarization.<sup>3,4</sup> Due to the lack of experimental electrostrictive data on PZT, the electrostrictive constants were assumed to be independent of composition and temperature. Zorn et al.<sup>5</sup> used an x-ray technique to measure the composition and temperature dependence of the electrostrictive constants of crystallites in PZT (modified with strontium, barium, and niobium) ceramic samples with compositions near the tetragonal-rhombohedral morphotropic boundary. They found that the electrostrictive constants were independent of temperature, but dependent on composition.

The purpose of this study was to further investigate the composition and temperature dependence of the electrostrictive constants in the PZT system. In the next section calculations of the temperature dependence of the electrostrictive constants for three PZT compositions will be presented. In Section III the results of experimental measurements of the compositional dependence of the ceramic electrostrictive  $Q_{12}$  constant will be described. In Section IV series and parallel averaging relations, analogous to the Voigt and Reuss methods of averaging the elastic constants<sup>6</sup>, will be used to calculate the single-crystal electrostrictive constants of two PZT compositions from a combination of single-crystal and ceramic data. The data from Sections III and IV will then be used in Section V with additional data from the literature to approximate the compositional dependence of the electrostrictive constants of PZT. Finally a summary of this study will be presented in Section VI.



## II. TEMPERATURE DEPENDENCE OF THE ELECTROSTRICTIVE CONSTANTS OF PZT

Jang<sup>7</sup> and Uchino et al.<sup>8</sup> have shown that the single crystal electrostrictive constants  $Q_{11}$  and  $Q_{12}$  of  $\text{Pb}(\text{Mg}_{1/3}\text{Nb}_{2/3})\text{O}_3$  are independent of temperature, within the limits of their experimental error. Zorn et al.<sup>5</sup> found that from 150 to 200°C the electrostrictive constants  $Q_{11}$ ,  $Q_{12}$  and  $Q_{44}$  of crystallites in  $\text{Pb}_{0.83}\text{Sr}_{0.12}\text{Ba}_{0.05}[\text{Zr}_{0.6}\text{Ti}_{0.38}\text{Nb}_{0.02}]\text{O}_3$  ceramic were independent of temperature, again within the limits of the experimental error. In addition, Meng et al.<sup>9</sup> found that the  $Q_{11}$  and  $Q_{12}$  constants of ceramic PLZT (lanthanum modified PZT) were virtually independent of temperature. Thus from these measurements the electrostrictive constants of perovskite ferroelectrics appear to be fairly independent of temperature. In this section additional calculations from published data will be presented to further demonstrate that the electrostrictive constants of PZT compositions are only slightly temperature dependent.

The temperature dependence of the spontaneous polarization and strain will be used to calculate the electrostrictive constants for  $\text{PbTiO}_3$ , PZT 40/60 (40%  $\text{PbZrO}_3$  and 60%  $\text{PbTiO}_3$ ), and PZT 90/10 using the following tetragonal and rhombohedral relations<sup>3</sup>:

*Tetragonal*

$$x_1 = x_2 = Q_{12} P_3^2, \quad x_3 = Q_{11} P_3^2, \quad x_4 = x_5 = x_6 = 0 \quad (1)$$

*Rhombohedral*

$$x_1 = x_2 = x_3 = (Q_{11} + 2 Q_{12}) P_3^2, \quad x_4 = x_5 = x_6 = Q_{44} P_3^2 \quad (2)$$

The  $x_i$  ( $i = 1, 2, \dots, 6$ ) are the spontaneous strains in reduced notation.  $Q_{11}$ ,  $Q_{12}$ , and  $Q_{44}$  are the cubic electrostrictive constants.  $P_3$  is the component of the spontaneous polarization in the  $x_3$  direction, and thus is equal to the spontaneous polarization ( $P_S$ ) in the tetragonal phase. In the rhombohedral phase  $P_3 = 3^{1/2} P_S$ .

Equations (1) and (2) were derived from the Devonshire form of the elastic Gibbs free energy function under zero stress conditions<sup>3</sup>, and can be used to calculate the

electrostrictive constants from experimental spontaneous polarization and strain data.

Equation (2) represents the spontaneous strain relations for the high-temperature rhombohedral phase in the PZT system. The low-temperature rhombohedral phase will not be dealt with in this paper (see Reference 4 for strain relations for this phase). Equation (1) will be used for the  $\text{PbTiO}_3$  and PZT 40/60 compositions, which have tetragonal structures. Equation (2) will be used for the rhombohedral PZT 90/10 composition.

The only direct experimental data available on the temperature dependence of the spontaneous polarization of single crystal  $\text{PbTiO}_3$  was calculated by Remeika and Glass<sup>10</sup> from pyroelectric measurements. They found the room temperature value to be  $0.56 \text{ C/m}^2$  using liquid electrodes and a pulsed field technique. This value is smaller than Gavril'yachenko et al.'s<sup>11</sup> value of  $0.75 \text{ C/m}^2$ . For use in calculating the electrostrictive constants, Remeika and Glass's data was corrected to agree with Gavril'yachenko et al.'s value using the following relation:

$$P_s = (\Delta P + 0.17 \text{ C/m}^2) (0.75/0.56) \quad (3)$$

$\Delta P$  was the change in polarization that Remeika and Glass calculated from their pyroelectric measurements, and 0.17 is their  $P_s$  value at  $T_C$ .

Haun et al.<sup>12</sup> calculated the spontaneous strains  $x_1$  and  $x_3$  of the tetragonal structure of  $\text{PbTiO}_3$  from high-temperature x-ray diffraction cell constant data by assuming that the electrostrictive constants were independent of temperature. The following procedure was used to recalculate the spontaneous strains independent of the electrostrictive constants for use in this study. Using the data from Reference 12 the first step was to use a linear extrapolation of the cubic cell constant down to the first four sets of tetragonal cell constant data. The spontaneous strains  $x_1$  and  $x_3$  were then calculated at these four temperatures [using Equation (19) in Reference 12], and fitted with theoretical strain relations [Equations (17) and (18) in Reference 12]. Using the constants obtained from this fitting the spontaneous strain could then be extrapolated down to lower temperatures [using Equations

(17) and (18) in Reference 12].

This spontaneous strain data was then used with Remeika and Glass's corrected polarization data (described above) to calculate the temperature dependence of the electrostrictive  $Q_{11}$  and  $Q_{12}$  constants of  $\text{PbTiO}_3$ , as shown in Figure 1(a). Only a slight temperature dependence was found up to about  $300^\circ\text{C}$ . The larger increase of the electrostrictive constants above  $300^\circ\text{C}$  was probably due to the larger error in polarization and strain data near  $T_C$  where large changes occur in these quantities. The values of the percent change in  $Q_{11}$ ,  $Q_{12}$ ,  $-Q_{11}/Q_{12}$  and  $Q_h (= Q_{11} + 2 Q_{12})$  for  $\text{PbTiO}_3$  from 0 to  $100^\circ\text{C}$  are listed in Table I. All three constants change less than 2 %/ $100^\circ\text{C}$ , and the ratio  $-Q_{11}/Q_{12}$  only changes 0.37 %/ $100^\circ\text{C}$ .

Tsuzuki et al.<sup>13</sup> measured the spontaneous polarization versus temperature on a PZT 40/60 single crystal from ferroelectric hysteresis loops. This data was used with Amin et al.'s<sup>3</sup> spontaneous strain data to calculate the temperature dependence of the electrostrictive constants  $Q_{11}$  and  $Q_{12}$ , as shown in Figure 1(b). Since this strain data was calculated using the cubed root of the tetragonal volume as the extrapolation of the cubic cell constant [problems develop when using this procedure; see Reference 12 for details], it was first corrected using the value of the  $Q_{11}/Q_{12}$  ratio that was determined in Section V of this paper. As can be seen in Figure 4.1(b) the electrostrictive constants of PZT 40/60 are only slightly temperature dependent. This dependence again becomes stronger at higher temperatures approaching  $T_C$ , probably because of the larger error in this region. The % change/ $100^\circ\text{C}$  is listed in Table I. The value is larger than that of  $\text{PbTiO}_3$ , but still should be considered small.

Clarke and Glazer<sup>14</sup> measured the temperature dependence of the spontaneous polarization of PZT 90/10 single crystals from hysteresis loops. They also measured the rhombohedral cell constants using high temperature x-ray diffraction. The spontaneous strain  $x_4 [= (90 - \alpha_R)/90]$  was calculated from their rhombohedral angle ( $\alpha_R$ ) data, and used with the polarization data to calculate the electrostrictive  $Q_{44}$  constant in the high-temperature

rhombohedral state, as shown in Figure 1(c). From 140 to 190°C the  $Q_{44}$  constant was virtually independent of temperature, with only a 0.47 %change/100°C from a linear fit (listed in Table I). Above and below the plotted temperature range the  $Q_{44}$  increased significantly as the temperature approached the transitions to the cubic phase at higher temperatures, and the low-temperature rhombohedral phase at lower temperatures. This is again believed to be probably due to the larger experimental error in the measurements at temperatures close to the transitions.

The data in Figure 1 and Table I have shown that the electrostrictive constants of  $\text{PbTiO}_3$  and PZT compositions are only slightly temperature dependent in agreement with the data in the literature on perovskite ferroelectrics.

### III. EXPERIMENTAL MEASUREMENTS OF THE CERAMIC $Q_{12}$ CONSTANT

As described in the Introduction the values of the single-crystal electrostrictive constants as a function of composition are required for the development of a thermodynamic theory of PZT. Due to the difficulty of growing single-crystals of PZT very little single-crystal electrostrictive data exists. Some electrostrictive data was measured on ceramic PZT samples<sup>15</sup>, but this data is conflicting and does not provide a complete picture of the electrostrictive properties of PZT. To provide additional data to determine the compositional dependence of the electrostrictive constants in the PZT system, the  $Q_{12}$  constant was measured on a series of ceramic samples. These measurements will be described in this section.

Pure homogeneous PZT ceramic samples were fabricated from sol-gel derived powders as described in Reference 16. Thin rectangular-shaped samples with dimensions of 10 by 4 by 0.3 mm were cut from sintered disks, and sputtered with gold electrodes. The electrostrictive strain and polarization were measured simultaneously under a cycling electric field at a frequency of 0.1 Hz. A variable frequency modified Sawyer-Tower circuit<sup>17</sup> was

used to measure polarization-electric field hysteresis loops, which were used to determine values of the polarization as a function of applied electric field. A polyimide based foil strain gage\* was carefully bonded to the samples with a polyester adhesive.\*\* The gage resistance was measured using a dc bridge type dynamic strain amplifier.\*\*\* The transverse strain level,  $\epsilon_{12}$ , was then recorded on a strip chart recorder as a function of electric field.

The electrostrictive  $Q_{12}$  constant was calculated from the slope of the transverse strain plotted versus the square of the polarization using the method described in Reference 9. The resulting  $Q_{12}$  values for five PZT compositions are listed in Table II, and plotted later in this paper in Figure 3(b). The  $Q_{12}$  constant increased slightly from PZT 90/10 to 60/40, and then a large increase occurred near the PZT 50/50 composition. Zorn et al.<sup>5</sup> found similar results for  $\text{Pb}_{0.83}\text{Sr}_{0.12}\text{Ba}_{0.05}[\text{Zr}_x\text{Ti}_{0.98-x}\text{Nb}_{0.02}]\text{O}_3$  compositions with  $x$  ranging from 0.45 to 0.65, where the  $Q_{12}$  constant, as well as the  $Q_{11}$  constant, increased with increasing titanium content.

#### IV. CALCULATION OF THE SINGLE-CRYSTAL ELECTROSTRICTIVE CONSTANTS FOR PZT 50/50 AND 90/10

The ceramic  $Q_{12}$  data presented in Section III was used with additional data from the literature to determine the single-crystal electrostrictive constants using series and parallel averaging relations. PZT 50/50 and 90/10 were the only compositions where enough electrostrictive data was available to use this procedure. The methods used to calculate the constants for these compositions will be described in this section.

\*Kyowa KFR-02-C1-11, Kyowa Electronic Instruments Co., LTD., Tokyo, Japan.

\*\*Kyowa PC-12.

\*\*\*Kyowa DPM-612B.

Series and parallel electrostrictive averaging relations, analogous to the Voigt and Reuss methods of averaging the elastic constants,<sup>6</sup> were presented in Reference 18. These equations relate the polycrystalline  $Q_{11}$ ,  $Q_{12}$ , and  $Q_{44}$  constants to the single-crystal constants. However, because a polycrystalline material is isotropic, the  $Q_{44}$  equation is related to the  $Q_{11}$  and  $Q_{12}$  relations, and thus only two independent equations exist for the series or parallel models. For this reason, if values of the polycrystalline  $Q_{11}$  and  $Q_{12}$  constants are known, then a single crystal constant or some relation involving the single crystal constants will also have to be determined to be able to use these averaging equations to solve for the single crystal  $Q_{11}$ ,  $Q_{12}$ , and  $Q_{44}$  constants.

The following procedure was used to calculate the single-crystal constants of PZT 50/50 using the ceramic  $Q_{12}$  value of  $-0.0228 \text{ m}^4/\text{C}^2$  from Table II, and additional information from the literature. Zhuang et al.<sup>19</sup> measured the ceramic piezoelectric  $d_{33}$  and  $d_{31}$  charge coefficients, and found that the  $d_{33}/d_{31}$  ratio was - 2.2 for the PZT 50/50 composition. The ceramic  $Q_{11}/Q_{12}$  ratio was also assumed to have a value of - 2.2, by assuming that the boundary conditions are the same for the  $d_{33}$  and  $d_{31}$  coefficients (see Reference 18 for more details concerning this assumption). If the ceramic  $Q_{11}/Q_{12}$  ratio is close to two, then the single crystal  $Q_{11}/Q_{12}$  ratio will also have a value close to two when using either the series or parallel models.<sup>18</sup> Zorn et al.<sup>5</sup> experimentally found that the  $Q_{11}/Q_{12}$  ratio was approximately - 2 for PZT compositions (modified with strontium, barium, and niobium) close to the tetragonal-rhombohedral morphotropic boundary.

Using the ceramic  $Q_{12}$  value of  $-0.0228 \text{ m}^4/\text{C}^2$  and a ceramic  $Q_{11}/Q_{12}$  ratio of - 2.2, the single crystal  $Q_{11}/Q_{12}$  ratio was varied to obtain reasonable values of the single crystal constants using the series and parallel models. This procedure resulted in a single crystal  $Q_{11}/Q_{12}$  ratio of - 2.1, and the same single crystal  $Q_{11}$  and  $Q_{12}$  constants when using either model, but different  $Q_{44}$  values. The series model gave a  $Q_{44}$  of  $0.0532 \text{ m}^4/\text{C}^2$ , while the parallel model resulted in a value of  $0.1106 \text{ m}^4/\text{C}^2$ . The average of the two models was taken as the  $Q_{44}$  for this composition and is listed in Table III along with the

resulting  $Q_{11}$  and  $Q_{12}$  values.

The series and parallel models were also used to determine the single-crystal constants for the PZT 90/10 composition using the ceramic  $Q_{12}$  value of  $-0.006 \text{ m}^4/\text{C}^2$  from Table II, and additional data from the literature. A single crystal  $Q_{44}$  constant of  $0.049 \text{ m}^4/\text{C}^2$  was calculated in the high-temperature rhombohedral state from Clarke and Glazer's<sup>14</sup> spontaneous polarization data, and Haun et al.'s<sup>20</sup> spontaneous strain  $x_4$  data. Ujma et al.<sup>21</sup> calculated the hydrostatic electrostrictive  $Q_h (= Q_{11} + 2 Q_{12})$  constant for ceramic  $\text{PbZrO}_3$  as a function of temperature and defect concentration from measurements of the pressure Curie constant (linear slope of the inverse dielectric constant of the cubic phase versus pressure). They found that the  $Q_h$  decreased with increasing temperature above  $T_C$ . Assuming that this temperature dependence was due to their measurements close to  $T_C$ , a value of  $Q_h$  of  $0.02 \text{ m}^4/\text{C}^2$  was chosen from their highest temperature measurement above  $T_C$  on an undefected sample. The PZT 90/10 composition was also assumed to have this value of  $Q_h$ .

Using the above values of the single-crystal  $Q_{44}$  and ceramic  $Q_{12}$  and  $Q_h$  constants, the single crystal electrostrictive constants of the PZT 90/10 composition were calculated from the series and parallel models. The ceramic  $Q_{12}$  constant and ceramic  $Q_{11}/Q_{12}$  (calculated from  $Q_{12}$  and  $Q_h$ ) ratio were fixed, while the single-crystal  $Q_{11}/Q_{12}$  ratio was varied until the average of the series and parallel  $Q_{44}$ 's was equal to the experimental value. Because the single crystal and polycrystalline  $Q_{11}/Q_{12}$  ratios were used in the series and parallel models, the same values result for the  $Q_{11}$  and  $Q_{12}$ , but different  $Q_{44}$ 's result. The series model gave a  $Q_{44}$  value of  $0.0385 \text{ m}^4/\text{C}^2$ , while the parallel model gave a value of  $0.0592 \text{ m}^4/\text{C}^2$ . The average of these two values was used as the  $Q_{44}$  for the PZT 90/10 composition, and is listed in Table III along with the resulting  $Q_{11}$  and  $Q_{12}$  values.

## V. COMPOSITIONAL DEPENDENCE OF THE ELECTROSTRICTIVE CONSTANTS OF PZT

In this section the single crystal electrostrictive constants determined in the last section for the PZT 50/50 and 90/10 compositions will be used with previously determined  $\text{PbTiO}_3$  constants<sup>12,22</sup> to approximate the compositional dependence across the PZT solid solution system. The values of the constants for these three compositions were listed in Table III. This data indicates that all three constants  $Q_{11}$ ,  $Q_{12}$ , and  $Q_{44}$  have larger values at the PZT 50/50 composition, than at the  $\text{PbTiO}_3$  or PZT 90/10 compositions.

The following Cauchy type equation was used to fit the  $Q_{11}$ ,  $Q_{12}$ , and  $Q_{44}$  data:

$$Q_{ij} = \frac{a}{1 + b(x - c)^2} + dx + e, \quad (4)$$

where  $a$ ,  $b$ ,  $c$ ,  $d$ , and  $e$  are constants, and  $x$  is the mole fraction  $\text{PbTiO}_3$  in PZT. The constant  $c$  was set equal to 0.5 to cause the peaks to form at the PZT 50/50 composition. Values of the  $a$ ,  $d$ , and  $e$  constants were found by fitting the data listed in Table III. The  $b$  constant was used to control the shape (width) of the peaks. A value of 200 was found to give fairly good upper and lower bounds (series and parallel models) around the ceramic  $Q_{12}$  data listed in Table II [see Figure 3(b)].

The resulting values of the five constants for  $Q_{11}$ ,  $Q_{12}$ , and  $Q_{44}$  are listed in Table IV. These values were used to calculate the compositional dependence of the electrostrictive constants using Equation (4), as shown in Figure 2(a). At this time the cause of the increase of the electrostrictive constants in the center of the phase diagram is not understood. However, this behavior does give fairly good agreement with other experimental data. The anomalous behavior may be related to the tetragonal-rhombohedral morphotropic boundary, or possibly due to some type of ordering that occurs in the PZT structure at the PZT 50/50 composition. In addition to the peaks in the electrostrictive constants, and the well established peaks in the dielectric and piezoelectric properties near the morphotropic boundary, the Curie constant has also been found to form a peak in this region.<sup>23</sup> Studying



these properties in other solid solution systems, such as the  $\text{Pb}(\text{Mg}_{1/3}\text{Nb}_{2/3})\text{O}_3$  -  $\text{PbTiO}_3$  system where the morphotropic boundary occurs well away from the 50/50 composition, may lead to an understanding of this behavior.

The  $Q_h$  constant and  $-Q_{12}/Q_{11}$  ratio were also calculated and plotted versus composition in Figures 2(b) and (c). The  $-Q_{12}/Q_{11}$  ratio also forms a peak at the PZT 50/50 composition with the peak value approaching 0.5, the theoretical maximum value of this ratio. The  $-Q_{12}/Q_{11}$  ratio is analogous to Poisson's ratio, which is equal to  $-s_{12}/s_{11}$ , where the  $s_{ij}$  are the elastic compliance coefficients. When the value of Poisson's ratio approaches 0.5, the material becomes mechanically incompressible. In a similar way when the  $-Q_{12}/Q_{11}$  ratio approaches 0.5, the hydrostatic electrostrictive constant becomes very small [see Figure 2(b)], and it is difficult to produce a volumetric electrostrictive strain in the material.

Haun et al.<sup>18</sup> showed that as the single-crystal  $-Q_{12}/Q_{11}$  ratio increases, the ceramic  $-Q_{12}/Q_{11}$  ratio will also increase, when using either the series or parallel models. This effect is shown in Figure 2(c), where the ceramic  $-Q_{12}/Q_{11}$  ratio is plotted versus composition for the series and parallel models. The single-crystal  $-Q_{12}/Q_{44}$  ratio also controls the ceramic  $-Q_{12}/Q_{11}$  ratio, but has little effect when the single-crystal  $-Q_{12}/Q_{11}$  ratio approaches 0.5.<sup>18</sup>

The piezoelectric anisotropy ( $-d_{33}/d_{31}$ ) in PZT ceramics is of considerable importance in hydrophone and medical ultrasonic imaging applications, where a large piezoelectric anisotropy is desired for increased hydrostatic sensitivity.<sup>24</sup> The piezoelectric anisotropy in PZT ceramics is much larger for compositions near the end members  $\text{PbTiO}_3$  and  $\text{PbZrO}_3$ , than for compositions in the center of the phase diagram near the morphotropic phase boundary.

The values of the single-crystal electrostrictive ratios  $-Q_{12}/Q_{11}$  and  $-Q_{12}/Q_{44}$  have been shown to be related to the large piezoelectric anisotropy that occurs in ceramic  $\text{PbTiO}_3$ .<sup>18</sup> This same type of analysis can now be extended across the PZT system using

the electrostrictive data plotted in Figure 2. The change in the single-crystal electrostrictive ratios across the PZT system will account for the change in piezoelectric anisotropy that occurs. The dielectric anisotropy and degree of polarization have also been shown to be related to the ceramic piezoelectric anisotropy.<sup>18, 25</sup>

The single crystal electrostrictive constants were also used to calculate the compositional dependence of the upper and lower limits of the ceramic constants using the series and parallel models, as shown in Figure 3. The ceramic  $Q_{12}$  data points shown in Figure 3(b) are from Table II, and were used to determine the value of the  $b$  constant (listed in Table IV) that caused the series and parallel models to give upper and lower bounds around the data, as described earlier in this section. Larger peaks occurred in the limits of the ceramic  $Q_{12}$  constant compared to that of the  $Q_{11}$  and  $Q_{44}$  constants. The upper and lower limits of the  $Q_{11}$  constant for  $\text{PbZrO}_3$  are in good agreement with experiment ceramic measurements by Roleder.<sup>26</sup>

## VI. SUMMARY

The electrostrictive constants of PZT were shown to be only slightly temperature dependent. The electrostrictive  $Q_{12}$  constant was measured as a function of composition on pure homogeneous PZT ceramic samples fabricated from sol-gel powders. This data was used with additional single-crystal and ceramic data from the literature to approximate values of the single-crystal electrostrictive constants using series and parallel equations, analogous to the Voigt and Reuss models for the elastic constants.

Equations were then used to fit the compositional dependence of the single-crystal and ceramic  $Q_{12}$  data. These equations were used to approximate the single-crystal electrostrictive constants as a function of composition. A peak was found to occur in the electrostrictive constants in the center of the phase diagram. Additional research is needed to understand the cause of this anomalous behavior.

The change in the ratios of the single-crystal electrostrictive constants as a function of composition can be used to explain the large electromechanical anisotropy that occurs in ceramic samples with compositions near the end members  $\text{PbTiO}_3$  and  $\text{PbZrO}_3$ , but does not occur in ceramic samples with compositions in the center of the phase diagram near the morphotropic phase boundary.

A thermodynamic theory for the entire PZT system has recently been completed using the values of the electrostrictive constants that have been presented in this paper. The results of this theory will be published in the future.

Table I Temperature Dependence of the Electrostrictive Constants of PZT

<u>Composition</u>	<u>Constant</u>	<u>Temp. Range (°C)</u>	<u>% Change/100°C</u>
PbTiO <sub>3</sub>	Q <sub>11</sub>	0 - 100	1.4
PbTiO <sub>3</sub>	- Q <sub>12</sub>	0 - 100	1.8
PbTiO <sub>3</sub>	Q <sub>h</sub>	0 - 100	1.0
PbTiO <sub>3</sub>	- Q <sub>11</sub> /Q <sub>12</sub>	0 - 100	0.37
PZT 40/60	Q <sub>11</sub> , - Q <sub>12</sub>	25 - 150	5.2
PZT 90/10	Q <sub>44</sub>	140 - 190	0.47

Table II Experimental Values of the Ceramic PZT

Electrostrictive Q<sub>12</sub> Constant

<u>Zr/Ti</u>	<u>Q<sub>12</sub> (m<sup>4</sup>/C<sup>2</sup>)</u>
90/10	- 0.0060
70/30	- 0.0075
60/40	- 0.0090
52/48	- 0.0158
50/50	- 0.0228

Table III Single Crystal Electrostrictive Constants

Composition	$Q_{11}$ ( $\text{m}^4/\text{C}^2$ )	$Q_{12}$ ( $\text{m}^4/\text{C}^2$ )	$Q_{44}$ ( $\text{m}^4/\text{C}^2$ )
PbTiO <sub>3</sub>	0.089 <sup>a</sup>	- 0.026 <sup>a</sup>	0.0675 <sup>b</sup>
PZT 50/50	0.0966	- 0.0460	0.0819
PZT 90/10	0.0508	- 0.0154	0.0490

<sup>a</sup> From Haun et al.<sup>12</sup><sup>b</sup> From Turik et al.<sup>22</sup>

Table IV. Values of the Constants used in Equation (4) to calculate the Compositional Dependence of the Electrostrictive Constants of PZT

Constant	a	b	c	d	e
Q <sub>11</sub>	0.029578	200	0.5	0.042796	0.045624
Q <sub>12</sub>	- 0.026568	200	0.5	- 0.012093	- 0.013386
Q <sub>44</sub>	0.025325	200	0.5	0.020857	0.046147

## REFERENCES

- <sup>1</sup>B. Jaffe, W. J. Cook, and H. Jaffe, *Piezoelectric Ceramics*, Academic Press, London (1971).
- <sup>2</sup>R. Clarke, and R. W. Whatmore, "The Growth and Characterization of  $\text{PbZr}_x\text{Ti}_{1-x}\text{O}_3$  Single Crystals," *J. of Crystal Growth*, **33**, 29-38 (1976).
- <sup>3</sup>A. Amin, M. J. Haun, B. Badger, H. A. McKinstry, and L. E. Cross, "A Phenomenological Gibbs Function for the Single Cell Region of the  $\text{PbZrO}_3\text{:PbTiO}_3$  Solid Solution System," *Ferroelectrics*, **65**, 107-130 (1985).
- <sup>4</sup>M. J. Haun, Z. Q. Zhuang, S. J. Jang, H. A. McKinstry, and L. E. Cross, "A Phenomenological Theory for the Second Order Transition Region of the PZT Solid Solution System," in *Proc. of the 6th IEEE International Symposium on the Applications of Ferroelectrics*, Lehigh, PA, edited by Van Wood, IEEE, New York, 398-401 (1986).
- <sup>5</sup>G. Zorn, W. Wersing, and H. Gobel, "Electrostrictive Tensor Components of PZT-Ceramics Measured by X-Ray Diffraction," *Jpn. J. App. Phys.*, **24** Supplement 24-2, 721-723 (1985).
- <sup>6</sup>R. F. S. Hearmon, *An Introduction to Applied Anisotropic Elasticity*, Oxford University Press, Oxford, pp. 41-44 (1961).
- <sup>7</sup>S. J. Jang, *Electrostrictive Ceramics for Transducer Applications*, Ph.D. Thesis in Solid State Science, The Pennsylvania State University (1979).
- <sup>8</sup>K. Uchino, S. Nomura, L. E. Cross, S. J. Jang, and R. E. Newnham, "Electrostrictive Effect in Lead Magnesium Niobate Single Crystals," *J. Appl. Phys.*, **51**[2] 1142-1145 (1980).
- <sup>9</sup>Z. Y. Meng, U. Kumar, and L. E. Cross, "Electrostriction in Lead Lanthanum Zirconate-Titanate Ceramics," *J. Am. Ceram. Soc.*, **68** [8] 459-62 (1985).
- <sup>10</sup>J. P. Remeika and A. M. Glass, "The Growth and Ferroelectric Properties of High Resistivity Single Crystals of Lead Titanate," *Mat. Res. Bull.*, **5**, 37-46 (1970).

- <sup>11</sup>V. G. Gavril'yachenko, R. I. Spinko, M. A. Martynenko, and E. G. Fesenko, "Spontaneous Polarization and Coercive Field of Lead Titanate," *Fiz. Tverd. Tela.*, **12** [5] 1532-1534 (1970); *Sov. Phys. - Solid State*, **12** [5] 1203-1204 (1970).
- <sup>12</sup>M. J. Haun, E. Furman, S. J. Jang, H. A. McKinstry, and L. E. Cross, "Thermodynamic Theory of  $\text{PbTiO}_3$ ", *J. Appl. Phys.*, **62** [8] 3331-3338 (1987).
- <sup>13</sup>K. Tsuzuki, K. Sakata, M. Wada, "Dielectric Properties of Single Crystals of  $\text{Pb}(\text{Zr}_x\text{Ti}_{1-x})\text{O}_3$  Solid Solutions ( $x \approx 0.5$ )," *Ferroelectrics*, **8**, 501-503 (1974).
- <sup>14</sup>R. Clarke, and A. M. Glazer, "The Ferroelectric-Ferroelectric Transition in Rhombohedral Lead Zirconate-Titanate," *Ferroelectrics*, **12**, 207-209 (1976).
- <sup>15</sup>Landolt-Bornstein Numerical Data and Functional Relationships in Science and Technology New Series, Group III: Crystal and Solid State Physics, Vol. 18 Supplement to Volume III/11, Elastic, Piezoelectric, Pyroelectric, Piezooptic, Electrooptic Constants, and Nonlinear Dielectric Susceptibilities of Crystals, Editors in Chief: K.-H. Hellwege and O. Madelung, Springer-Verlag, New York, p.274 (1984)
- <sup>16</sup>Z. Q. Zhuang, M. J. Haun, S. J. Jang, and L. E. Cross, "Fabrication and Characterization of Pure Homogeneous PZT Ceramics From Sol-Gel Derived Powders," *Am. Ceram. Soc.* (submitted for publication).
- <sup>17</sup>J. K. Sinha, "Modified Sawyer and Tower Circuit for Investigation of Ferroelectric Samples," *J. Phys. E.*, **42**, 696-701 (1965).
- <sup>18</sup>M. J. Haun, E. Furman, S. J. Jang, and L. E. Cross, "Modeling of the Electrostrictive, Dielectric and Piezoelectric Properties of Ceramic  $\text{PbTiO}_3$ ," *Trans. IEEE Ultrasonics, Ferroelectrics and Frequency Control Soc.*, (submitted for publication).
- <sup>19</sup>Z. Q. Zhuang, M. J. Haun, S. J. Jang, and L. E. Cross, "Low Temperature Dielectric, Piezoelectric, and Elastic Properties of Pure (Undoped) PZT Ceramics", in Proc. of the 6th IEEE International Symposium on the Applications of Ferroelectrics, Lehigh, PA, edited by Van Wood, IEEE, New York, 394-397 (1986).

<sup>20</sup>M. J. Haun, Y. H. Lee, H. A. McKinstry, and L. E. Cross, "High Temperature X-ray Diffraction Study of Sol-gel Derived  $\text{Pb}(\text{Zr}_x\text{Ti}_{1-x})\text{O}_3$  Powders", Proc. of the Thirty-fifth Annual Conference on Applications of X-ray Analysis, Aug. 4-8, 1986, Denver, CO, in *Advances in X-ray Analysis*, Vol. 30, 473-481 (1987).

<sup>21</sup>Z. Ujma, J. Handerek, and M. Pisarski, "Changes in Phase Transition Temperatures in  $\text{PbZrO}_3$  with Pb and O Vacancies under the Influence of Hydrostatic Pressure," *Ferroelectrics*, **64**, 237-245 (1985).

<sup>22</sup>A. V. Turik, E. G. Fesenko, V. G. Gavrilyachenko, and G. I. Khasabova, "Anisotropy of the Dielectric and Piezoelectric Properties of Lead Titanate," *Kristallografiya* **19**, 1095-1097 (1974); *Sov. Phys.-Crystallogr.* **19**, 677-678 (1974).

<sup>23</sup>A. Amin, L. E. Cross, and R. E. Newnham, "Calorimetric and Phenomenological Studies of the  $\text{PbZrO}_3\text{:PbTiO}_3$  System," *Ferroelectrics*, **37**, 647-650 (1981).

<sup>24</sup>H. Takeuchi, S. Jyomura, C. Nakaya, "New Piezoelectric Materials for Ultrasonic Transducers," Proc. IMF-6, Jpn. J. App. Phys., **24** Supplement **24-2**, 36-40 (1985).

<sup>25</sup>W. Wersing, K. Lubitz, and J. Mohaupt, "Anisotropic Piezoelectric Effect in Modified  $\text{PbTiO}_3$  Ceramics," Presented at the 6th IEEE International Symposium on the Applications of Ferroelectrics, Lehigh, PA (1986).

<sup>26</sup>K. Roleder, "Measurement of the High-Temperature Electrostrictive Properties of Ferroelectrics," *J. Phys. E: Sci. Instrum.*, **16**, 1157-1159 (1983).



## FIGURE CAPTIONS

Figure 1. The single crystal electrostrictive constants plotted versus temperature for (a)  $\text{PbTiO}_3$ , (b) PZT 40/60, and (c) PZT 90/10.

Figure 2. The electrostrictive constants and ratios plotted versus composition. The single crystal constants  $Q_{11}$ ,  $-Q_{12}$ ,  $Q_{44}$ , and  $Q_h$  are plotted in (a) and (b). The single crystal and ceramic  $Q_{11}/Q_{12}$  ratios (upper and lower limits labeled 1 and 2) were plotted in (c). A bar over a symbol refers to polycrystalline ceramic constants. The data points in (a) are from Table III.

Figure 3. The upper and lower limits of the polycrystalline ceramic electrostrictive constants plotted versus composition. Series and parallel models were used to calculate the curves labeled 1 and 2, respectively. The data points shown in (b) are from the ceramic measurements listed in Table II. A bar over a symbol refers to polycrystalline ceramic constants.

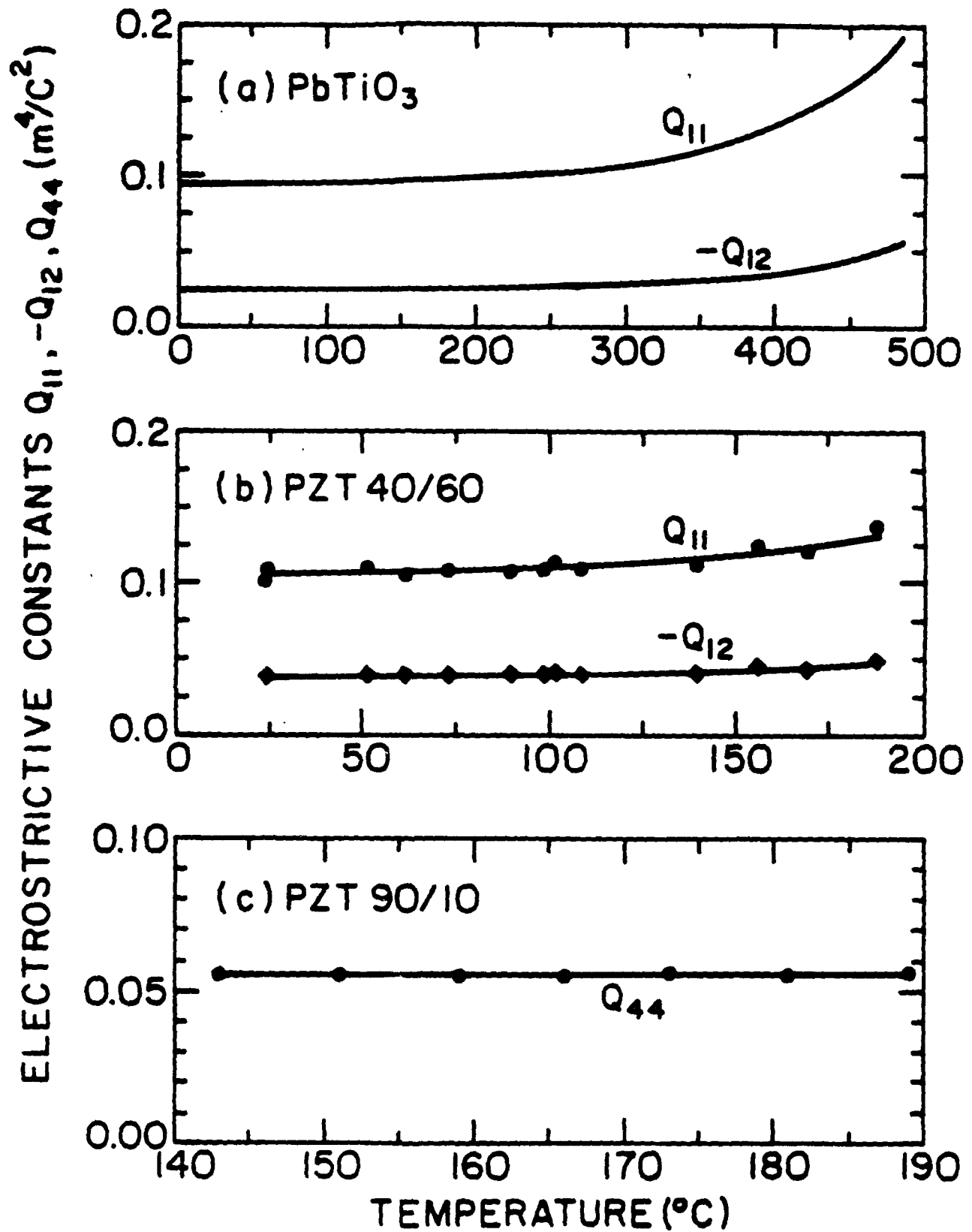


Figure 1

ELECTROSTRICTIVE CONSTANTS  $Q_{11}, -Q_{12}, Q_{44}, Q_h$  ( $\text{m}^4/\text{C}^2$ )  
AND RATIOS  $-Q_{12}/Q_{11}, -\bar{Q}_{12}/\bar{Q}_{11}$

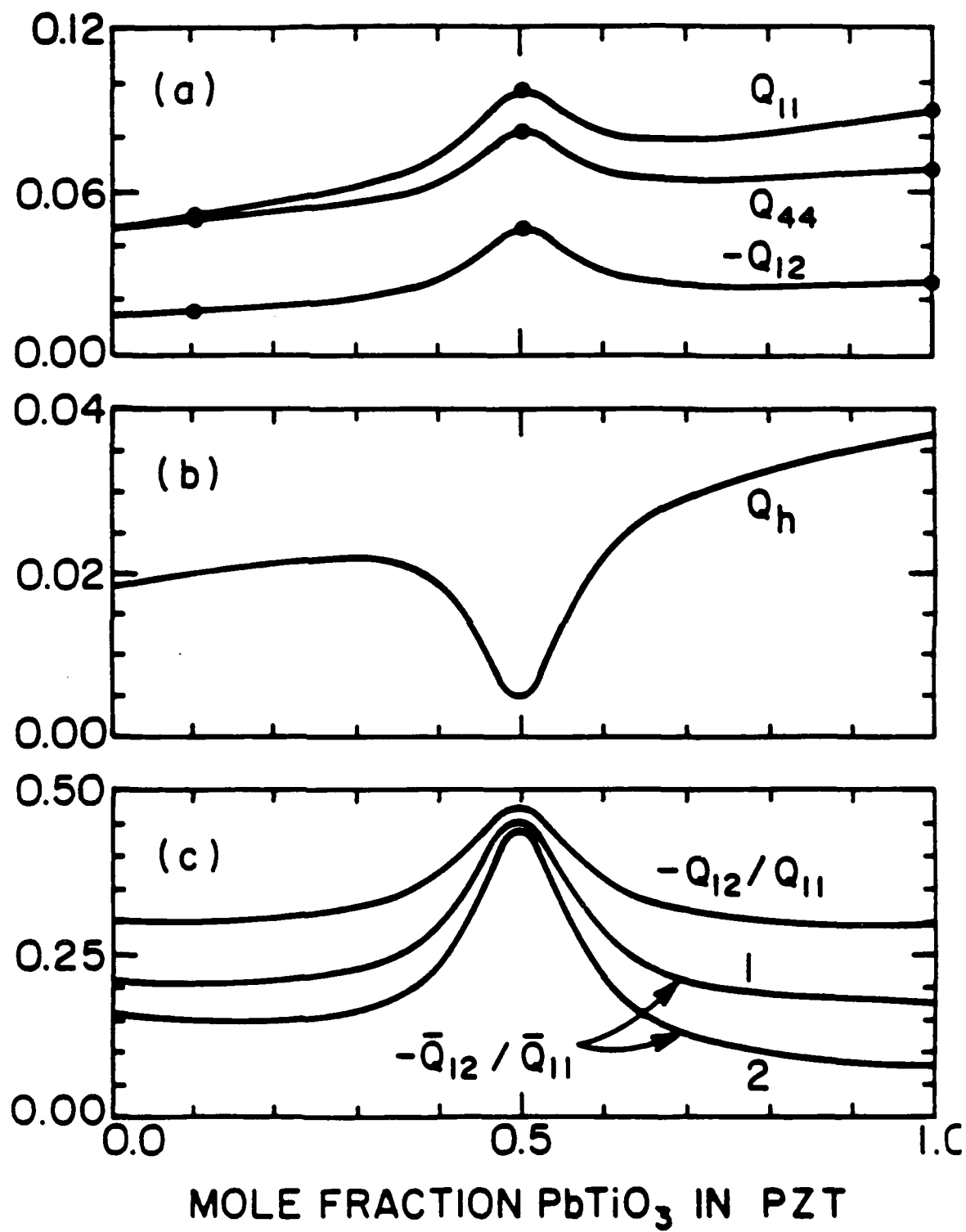


Figure 2

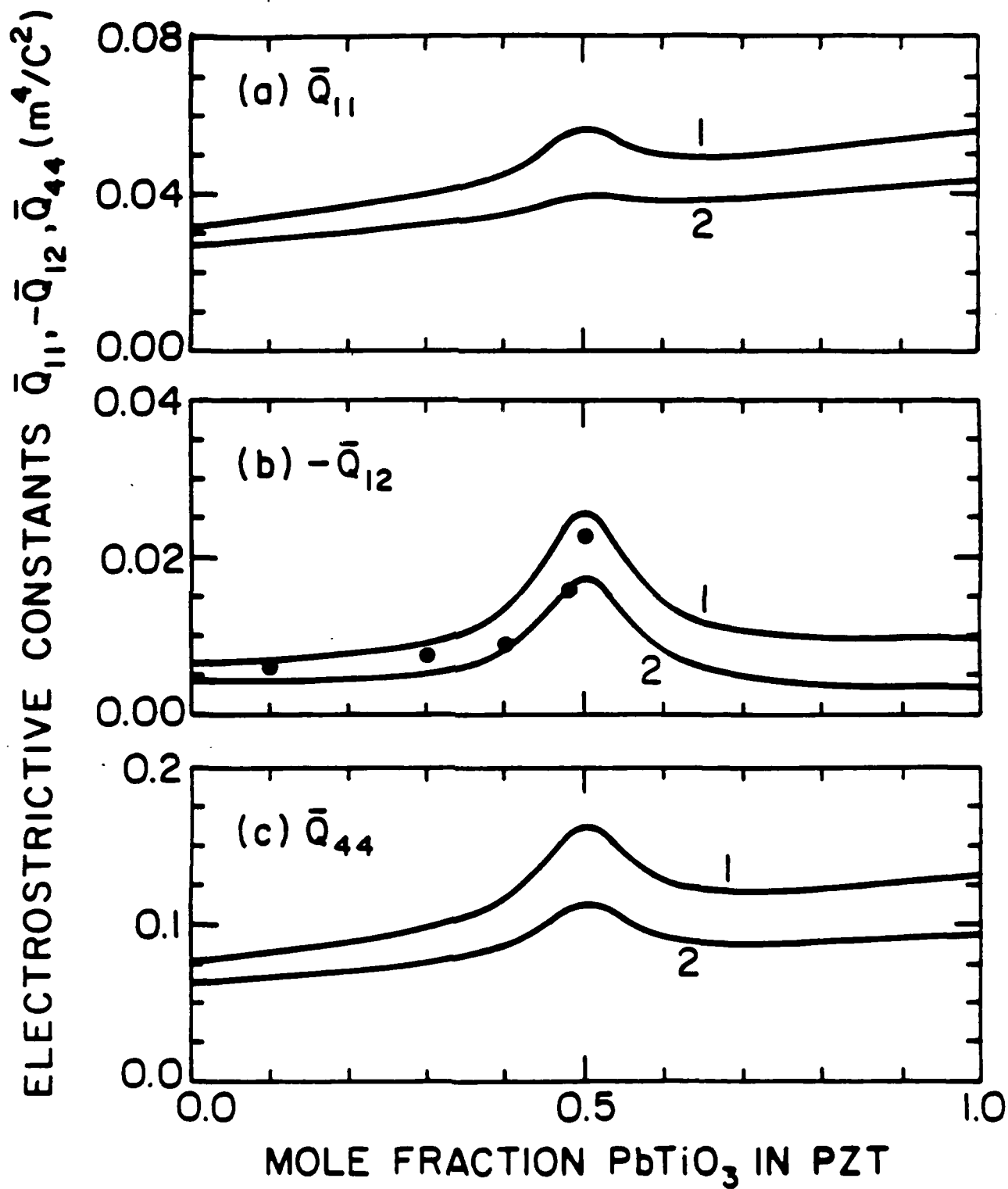


Figure 3

# TEMPERATURE BEHAVIOR OF DIELECTRIC AND PIEZOELECTRIC PROPERTIES OF SAMARIUM DOPED LEAD TITANATE CERAMICS

J.N. Kim  
Physics Department  
Pusan University  
Pusan, Korea

M.J. Haun, S.J. Jang and L.E. Cross  
Materials Research Laboratory  
The Pennsylvania State University  
University Park, PA 16802

X.R. Xue  
Nanjing Institute of Chemical Technology  
The Peoples Republic of China

## ABSTRACT

The dielectric and electromechanical coupling properties of Sm- and Mn-doped  $\text{PbTiO}_3$  ceramics were investigated from 4.2 to 300°K. The upper and lower limits of the ceramic dielectric and piezoelectric properties were calculated by averaging the single-domain constants which were determined from a phenomenological theory. Comparisons of the measured and calculated properties were then made.

The measured dielectric permittivity  $\epsilon_{33}^T$  and piezoelectric strain coefficient  $d_{33}$  appear to be mainly due to the averaging of the intrinsic single-domain response. The large piezoelectric and electromechanical anisotropies present in modified  $\text{PbTiO}_3$  ceramics also appears to be an intrinsic property of the material. The piezoelectric coefficient  $d_{31}$ , as well as the planar coupling coefficient  $k_p$ , were found to have very small values over two temperature regions, from 120 to 170°K and from 240 to 270°K.

## INTRODUCTION

Modified  $\text{PbTiO}_3$  ceramics which show large anisotropic piezoelectric coupling at room temperature were recently reported<sup>(1-4)</sup>. The temperature behavior of the piezoelectric properties of Sm- and Mn-doped  $\text{PbTiO}_3$  were also investigated<sup>(5)</sup>. It is interesting as well as important to understand why these modified  $\text{PbTiO}_3$  ceramics have such a large anisotropic electromechanical coupling property.

In this study, the dielectric properties,  $\epsilon_{33}^T$  and  $\tan \delta$ , and electromechanical coupling properties,  $d_{31}$ ,  $d_{33}$ ,  $k_p$ , and  $k_t$ , of 10 mole% Sm- and 2 mole% Mn-doped  $\text{PbTiO}_3$  ceramics were

investigated from 4.2 to 300°K. At low temperatures, the thermally activated contributions to the dielectric and coupling properties "freeze out." The observed temperature behavior of the material properties,  $\epsilon^{T_{33}}$ ,  $d_{33}$  and  $d_{31}$ , were compared with the predicted values of the intrinsic contributions to the upper and lower limits of the ceramic properties<sup>(6)</sup> which were calculated from the single crystal constants determined from a phenomenological theory of  $\text{PbTiO}_3$ <sup>(7)</sup>. The unusually small values of piezoelectric coefficient  $d_{31}$  were also explained according to the recent results of Damjanovic et al.<sup>(9,10)</sup>.

#### EXPERIMENTAL PROCEDURE

The composition investigated in this study was  $(\text{Pb}_{0.85}\text{Sm}_{0.10})(\text{Ti}_{0.98}\text{Mn}_{0.02})\text{O}_3$ . Reagent grade oxides,  $\text{PbO}$ ,  $\text{Sm}_2\text{O}_3$ ,  $\text{TiO}_2$ , and  $\text{MnO}$  were mixed and milled for 6 hours using zirconia balls, then dried and calcined in a closed alumina crucible at 900°C for 1 hour. The calcined powder was pressed in a die at 5000 psi to form green disks. These disks were fired at 1200°C for 1 hour in a closed crucible with a lead source. The final density of the ceramic samples was better than 95% of the theoretical value. Disks were cut to several different shapes and dimensions to measure the dielectric and electromechanical coupling coefficients. Reshaped samples were electroded with sputtered gold and poled in silicone oil with a field of 60 kV/cm applied for 5 minutes at 150°C. All of the samples satisfied the dimensional requirements of the IRE standards on piezoelectric crystals<sup>(8)</sup>. The samples were carefully connected with very fine silver wire and suspended in a vacuum in an in-house made holder on an Air Products and Chemicals Model LT-3-110 cryogenics system. The dielectric properties were measured on a Hewlett Packard automatic capacitance bridge model 4270A. The electromechanical coupling properties were investigated by the resonance method using a Hewlett Packard spectrum analyzer model 3585A.

#### RESULTS AND DISCUSSION

Two samples with the same composition and fabricated by the same procedure were studied. The relative dielectric permittivity  $\epsilon^{T_{33}}$  and dissipation factor  $\tan \delta$  were measured at 1 KHz from 4.2 to 300°K. These measurements are plotted in Figures 1(a) and 1(b).

The intrinsic dielectric permittivity of ceramic  $\text{PbTiO}_3$  was calculated using series and parallel models in Reference 7. These calculations were adjusted by shifting the Curie temperature  $T_C$  to 300°C to match that of the samples fabricated in this study. In Figure 1(a), the experimental and

intrinsic theoretical permittivities are compared. At low temperatures where the extrinsic contributions have "frozen out," the agreement is fairly good. As the temperature is increased, only a small difference develops between the experimental and theoretical permittivities, indicating that the polarizability is still largely due to the intrinsic averaging of the single-domain response.

The dielectric loss measurements are shown in Figure 1(b). Below about 50°K the loss decreases very rapidly, which suggests that the thermally activated contributions to the dielectric properties freeze out quickly at low temperatures.

The measured piezoelectric coefficients,  $d_{33}$  and  $d_{31}$ , are shown in Figures 2(a) and 2(b) along with the calculated upper and lower limits of the intrinsic ceramic piezoelectric coefficients. These calculations were made by shifting the Curie temperature to 300°C, as was done with the dielectric data, using the results of Reference 7. The experimental  $d_{33}$  data falls between the predicted upper and lower limits with a similar temperature dependence. This indicates that the measured  $d_{33}$  is mostly due to the intrinsic single domain response.

The  $d_{31}$  measurements also fall between the predicted upper lower limits, except over two temperature regions, from 120 to 170°K and from 240 to 270°K. Over these temperature regions, the resonance spectrum displaced upon the HP 3585A analyzer was too weak to measure, as shown in Figure 3, with the resonance at 300°K for comparison. This suggests that the IRE standard method may not be adequate near these two temperature regions.

The exceedingly small frequency differences between parallel ( $f_p$ ) and series ( $f_s$ ) resonances may not be close enough to the differences between the maximum ( $f_n$ ) and minimum ( $f_m$ ) impedance frequencies. The vector impedance method is more accurate in obtaining greater precision in the case of immeasurably small resonance regions like these.

Damjanovic, et al.<sup>(9,10)</sup> used this method to measure the complex values of the material constants ( $d_{ij}^*$ ,  $s_{ij}^*$ , and  $\epsilon_{ij}^*$ ). They found that the real part of the  $d_{31}$  coefficient changes sign and becomes positive at high temperatures. This result is illustrated in the insert in Figure 2(b) by the dashed curve (note that the negative  $d_{31}$  is plotted). The sign of  $d_{31}$  could not be measured using the resonance method in this study, and therefore was not assumed to change sign at  $T_2$ . However, a change in sign would account for the immeasurably small resonance region at  $T_2$ . Damjanovic, et al.<sup>(10)</sup> also found that below  $T_2$  the  $d_{31}$  coefficient formed a peak (when plotting

the negative  $d_{31}$  as in Figure 2(b), this would be a minimum with a value approaching zero) at about 125°K. This behavior probably accounts for the small resonance region at  $T_1$ .

The change in sign of the  $d_{31}$  coefficient at  $T_2$  to positive values at high temperature was explained by Damjanovic, et al.<sup>(10)</sup> as being due to the positive extrinsic contributions which dominate the negative intrinsic contribution. This appears to be possible, since the intrinsic  $d_{31}$  is very small. In Reference 7, the small values of the  $d_{31}$  coefficient and thus large piezoelectric anisotropy ( $d_{33}/d_{31}$ ) of PbTiO<sub>3</sub> ceramics were shown to be due to the intrinsic averaging of the single crystal electrostrictive constants. The possibility of a change in sign of the intrinsic  $d_{31}$  due to a slight variation in the single crystal electrostrictive anisotropies ( $Q_{11}/Q_{12}$  and  $Q_{44}/Q_{12}$ ) was also demonstrated.

The planar coupling coefficient,  $k_p$ , is plotted as a function of temperature in Figure 4(a). In two temperature regions, as discussed for  $d_{31}$ ,  $k_p$  becomes extremely small. The thickness coupling coefficient,  $k_t$ , is weakly dependent on temperature and has a value of about 46%. Figure 4(b) shows the ratio  $k_t/k_p$  plotted versus temperature. This ratio becomes very large in two temperature regions, 120 to 170°K and 240 to 270°K. These large electromechanical anisotropies indicate that this material would be useful in ultrasonic transducer applications.

### CONCLUSIONS

The relative dielectric permittivity,  $\epsilon_{33}^T$ , of the modified PbTiO<sub>3</sub> ceramics fabricated in this study appears to be largely due to the averaging of the intrinsic single-domain response. The calculated values of the upper and lower limits of the ceramic permittivity agree fairly well at low temperatures with the measured values, and only a small difference develops as the temperature increases. The piezoelectric  $d_{33}$  and thickness coupling  $k_t$  coefficients are weakly dependent on temperature and have values of about  $30 \times 10^{-12}$  C/N and 46%, respectively. The planar coupling  $k_p$  and piezoelectric  $d_{31}$  coefficients exhibit very interesting temperature behaviors. In two temperature regions, from 120 to 170°K and from 240 to 270°K (or  $T_1$  and  $T_2$  in Figure 2(b)),  $|d_{31}|$  and  $k_p$  become too small to measure using the resonance method.

Damjanovic, et al.<sup>(9,10)</sup> used a vector impedance method and found that the  $d_{31}$  coefficient changes sign at  $T_2$  to positive values at high temperatures. The low values of the  $|d_{31}|$  at  $T_1$  were found to be due to a minimum in the  $|d_{31}|$  which occurs in this temperature region.



The values of the measured  $d_{33}$  and  $d_{31}$  coefficients were within the predicted upper and lower bounds which were calculated by averaging the intrinsic single-domain properties. The generally large piezoelectric and electromechanical anisotropies present in modified  $\text{PbTiO}_3$  ceramics appear to be an intrinsic property of the material.

#### ACKNOWLEDGEMENT

The authors wish to thank D. Damjanovic for the valuable discussions. This work was supported by North American Philips Corporation.

## REFERENCES

1. H. Takeuchi, S. Jyomura, E. Yamamoto and Y. Ito, "Electromechanical Properties of  $(\text{Pb,Ln})(\text{Ti,Mn})\text{O}_3$  Ceramics (Ln = rare earths)," J. Acoust. Soc. Am., 72(4):1114-1120 (1982).
2. T. Takahashi and Y. Yamashita, "Anisotropic Piezoelectric Properties of Modified Lead Titanate Ceramics," Proc. Second U.S.:Japan Seminar on Dielectric and Piezoelectric Ceramics, Williamsburg, VA, Vol. 1, pp. 20-25 (1984).
3. H. Takeuchi and S. Jyomura, "Piezoelectric Ceramics with Large Electromechanical Anisotropy," Proc. Second U.S.:Japan Seminar on Dielectric and Piezoelectric Ceramics, Williamsburg, VA, Vol. 2, pp. 324-329 (1984).
4. H. Takeuchi, S. Jyomura and C. Nakaya, "New Piezoelectric Materials for Ultrasonic Transducers," Jpn. J. Appl. Phys., Vol. 24, Suppl. 24-2, pp. 36-40 (1985).
5. X.R. Xue, J.N. Kim, S.J. Jang, L.E. Cross and R.E. Newham, "Temperature Behavior of Dielectric and Electromechanical Coupling Properties of Samarium Modified Lead Titanate Ceramics," Jpn. J. Appl. Phys., Vol. 24, Suppl. 24-2, pp. 718-720 (1985).
6. M.J. Haun, E. Furman, S.J. Jang and L.E. Cross, "Modeling of the Electrostrictive, Dielectric and Piezoelectric Properties of Ceramic  $\text{PbTiO}_3$ ," Trans. IEEE Ultrasonics, Ferroelectrics and Frequency Control Society (submitted).
7. M.J. Haun, E. Furman, S.J. Jang, H.A. McKinstry and L.E. Cross, "Thermodynamic Theory of  $\text{PbTiO}_3$ ," J. Appl. Phys. (submitted).
8. "IRE Standards on Piezoelectric Crystals: Measurements of Piezoelectric Ceramics, 1961," Proc. IRE Vol. 49, pp. 1161-1169 (1961).
9. D. Damjanovic, T.R. Gururaja, S.J. Jang and L.E. Cross, "Temperature Behavior of the Complex Piezoelectric  $d_{31}$  Coefficient in Modified Lead Titanate Ceramics," Materials Letters Vol. 4, 414-419 (Sept. 1986).
10. D. Damjanovic, T.R. Gururaja, S.J. Jang and L.E. Cross, "Possible Mechanisms for the Electromechanical Anisotropy in Modified Lead Titanate Ceramics," Proc. IEEE Ultrasonic Symposium, Williamsburg, VA, Nov. 1986 (in press).

NO-A194 955

PIEZOELECTRIC AND ELECTROSTRICTIVE MATERIALS FOR  
TRANSDUCER APPLICATIONS. (U) PENNSYLVANIA STATE UNIV  
UNIVERSITY PARK MATERIALS RESEARCH LAB.

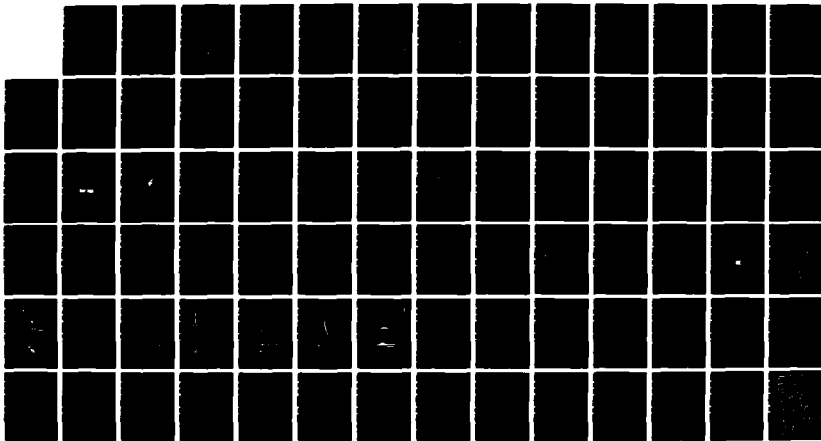
2/2

UNCLASSIFIED

L E CROSS ET AL MAR 88 N00014-82-K-0339

F/G 20/3

NL



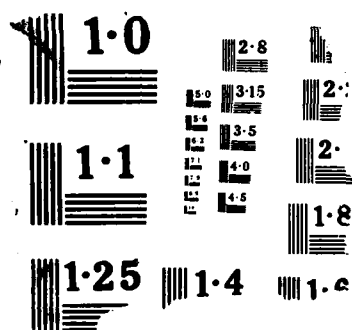


### FIGURE CAPTIONS

- Figure 1. The a) relative dielectric permittivities  $\epsilon_{33}^T$  and b) dissipation factor  $\tan \delta$  at 1 kHz plotted versus temperature. The data points are experimental measurements. The solid curves in a) are calculation of the upper and lower limits of the intrinsic ceramic permittivity.
- Figure 2. The piezoelectric strain coefficients a)  $d_{33}$  and b)  $d_{31}$  plotted versus temperature. The data points are experimental measurements and the solid curves are calculations of the upper and lower limits of the intrinsic piezoelectric response. The insert in b) illustrates the measured temperature dependence (solid curve) compared with the results of Damjanovic, et al.<sup>(9,10)</sup> (dashed curve).
- Figure 3. The admittance plotted versus frequency at 300°K (curve 1) and at a temperature within the temperature regions where the resonance was too weak to measure (curve 2).
- Figure 4. The a) planar coupling coefficient  $k_p$  and b) ratio  $k_t/k_p$  plotted versus temperature.

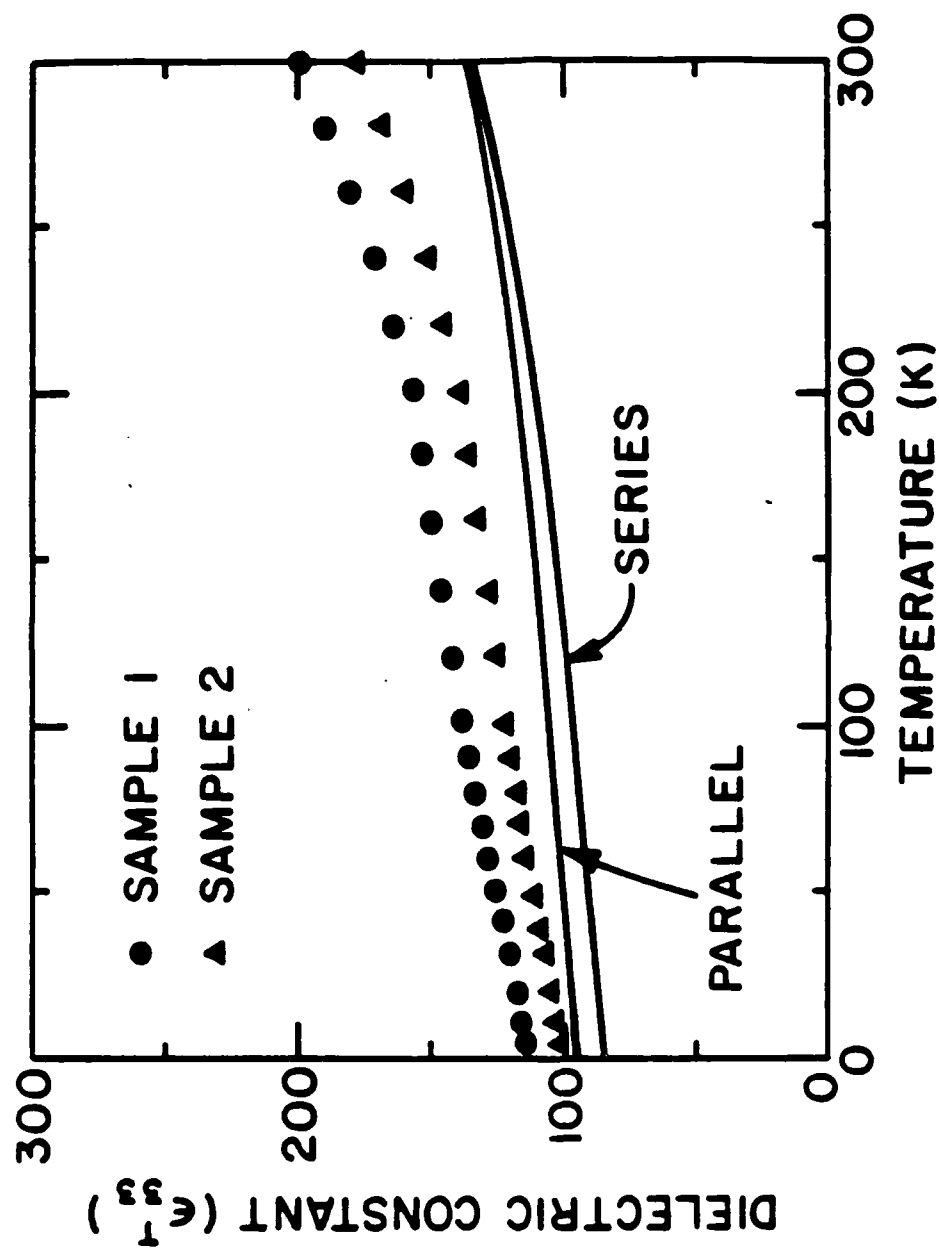


Figure 1(a)

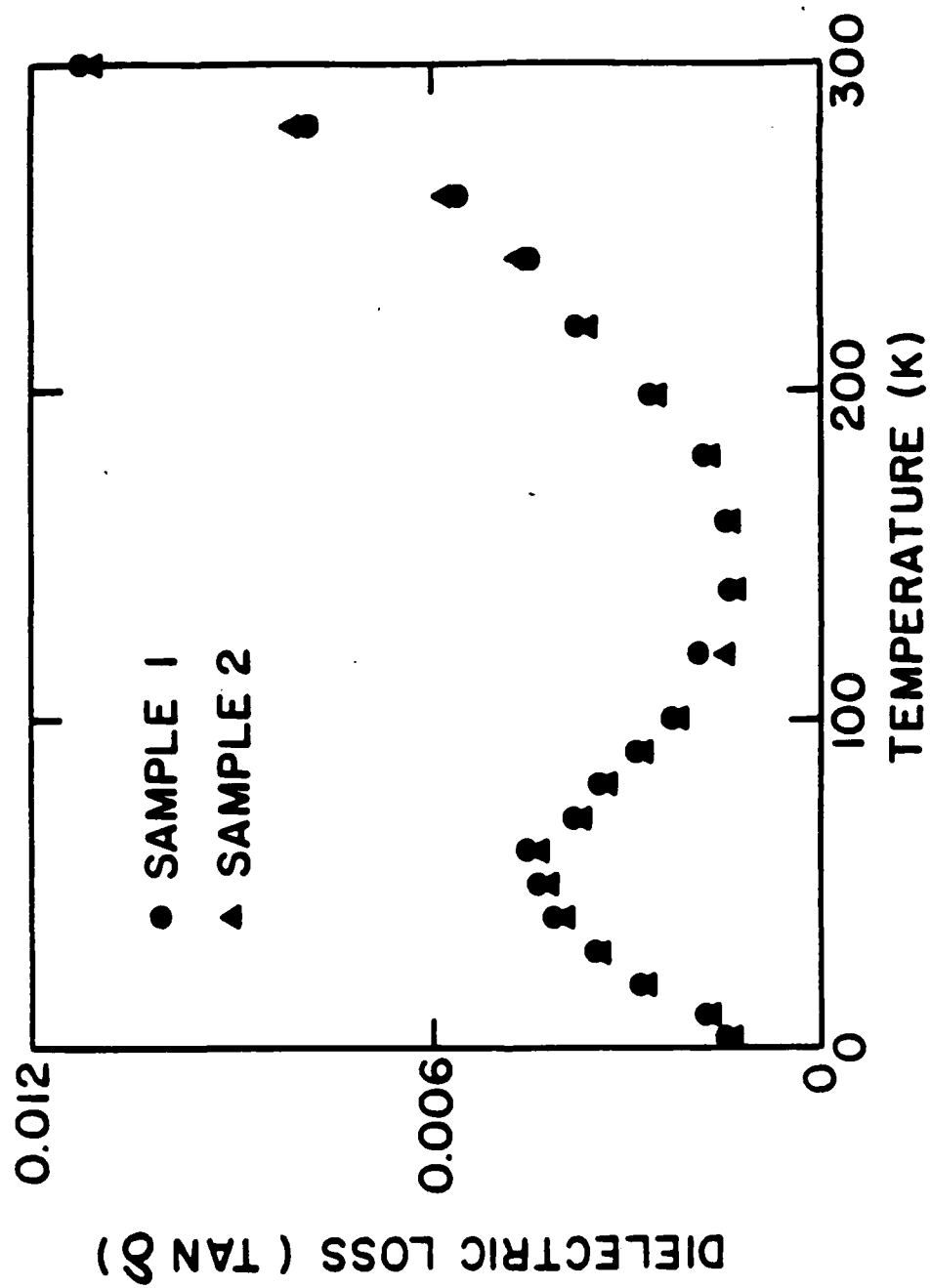


Figure 1(b)

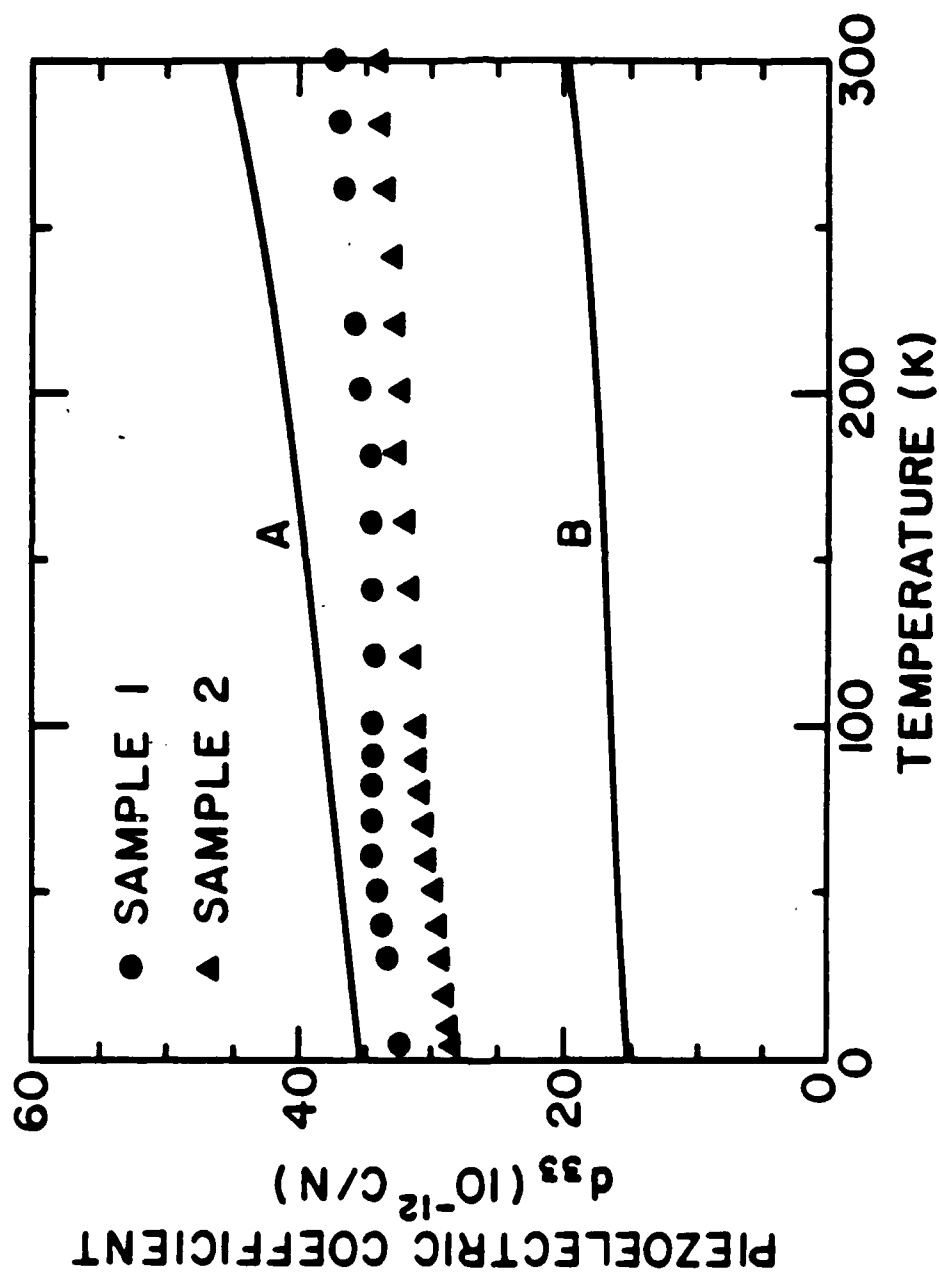


Figure 2(a)



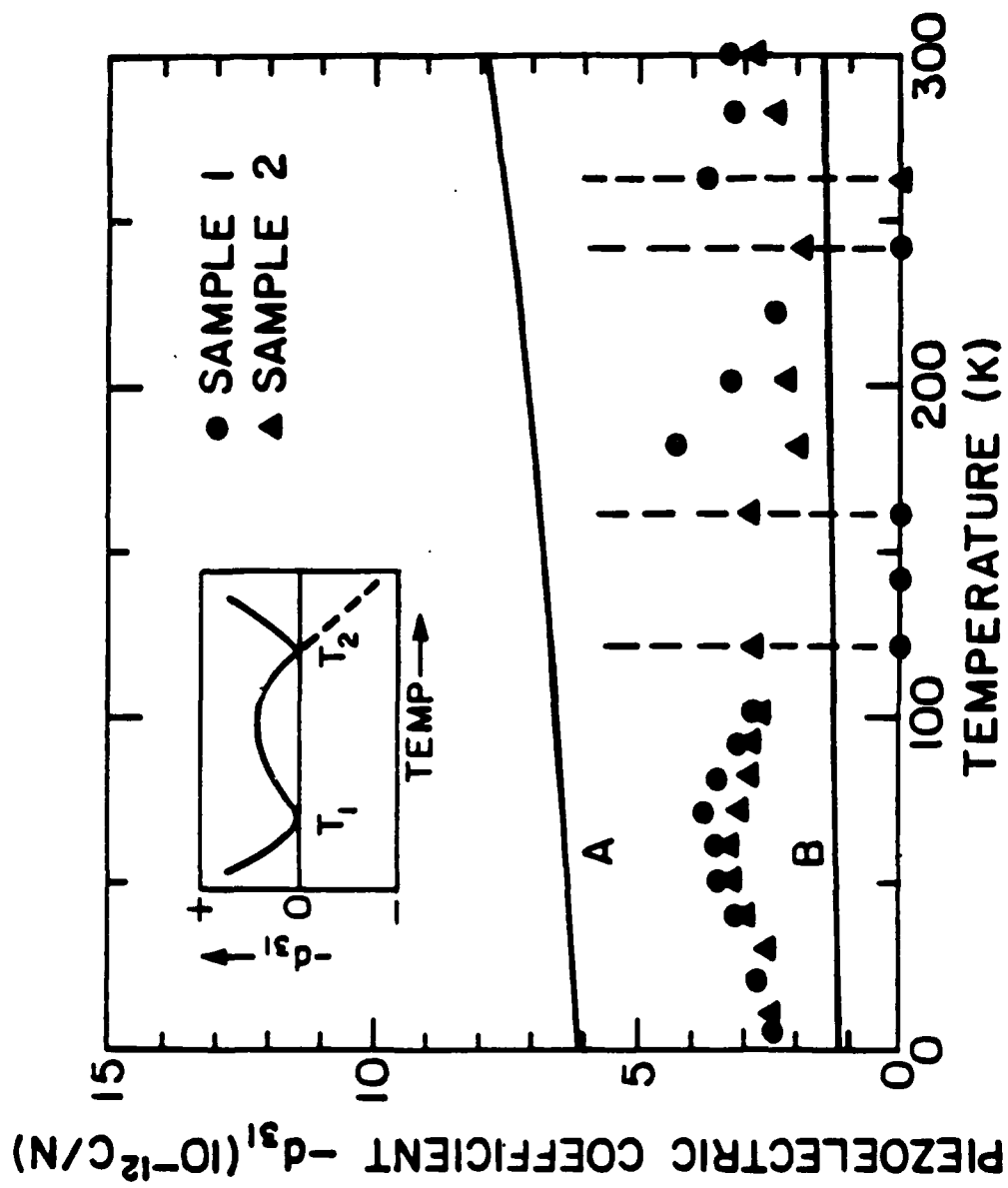
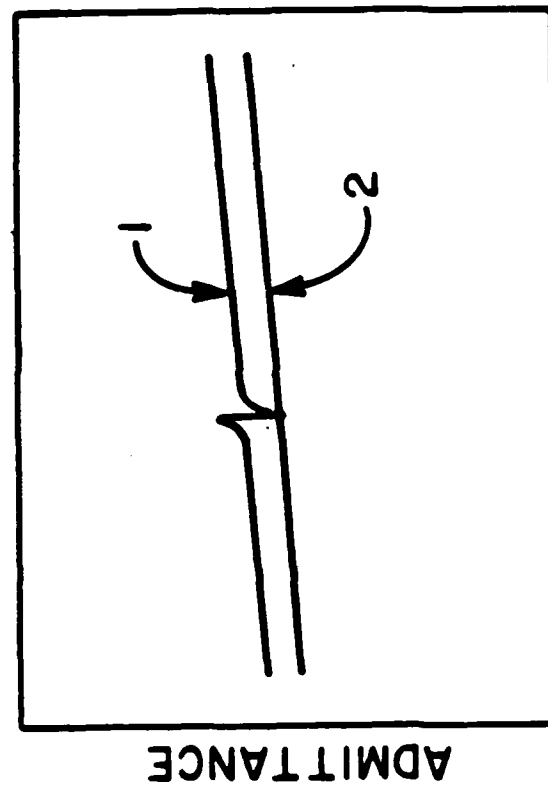


Figure 2(b)



*Figure 3*

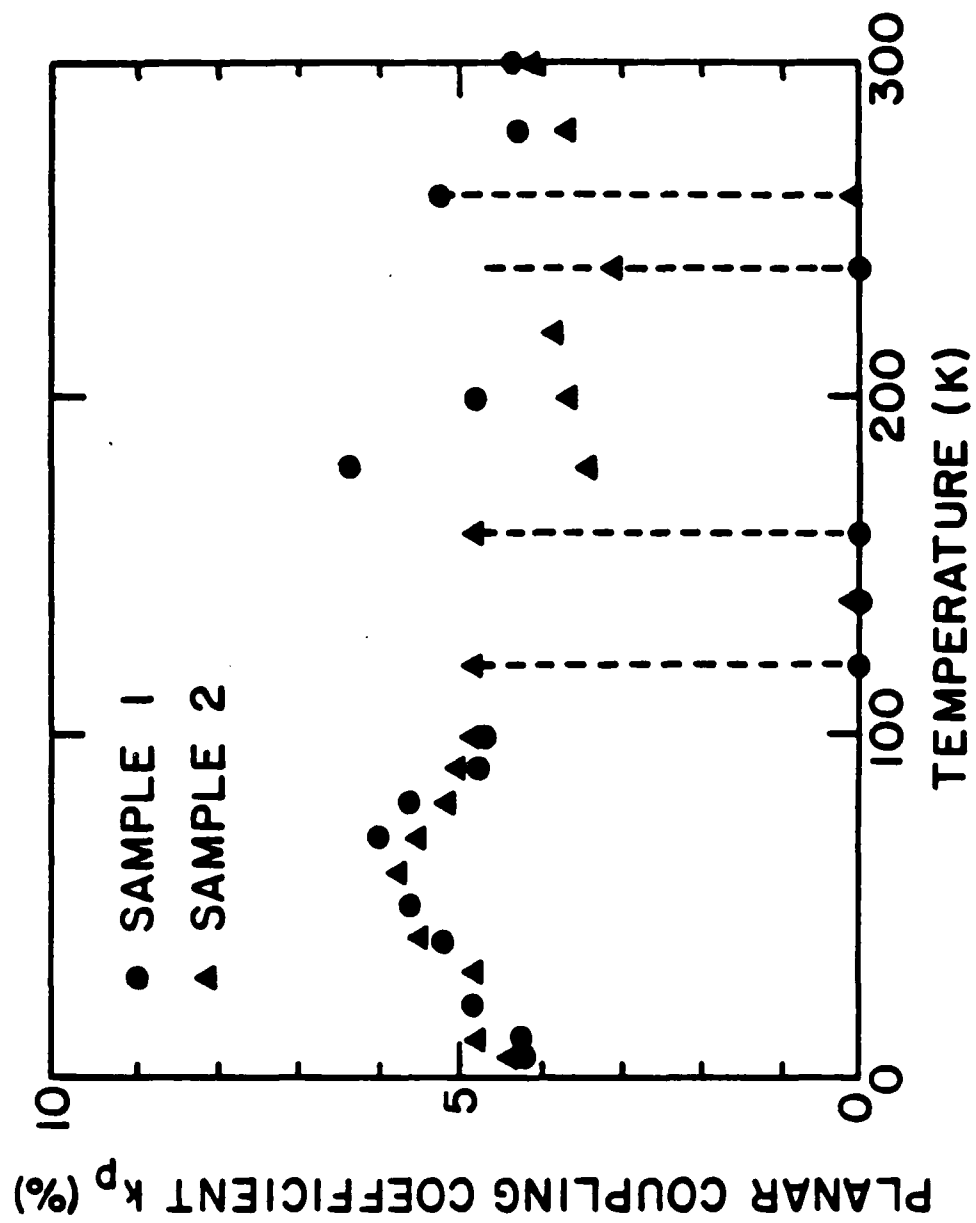


Figure 4(a)

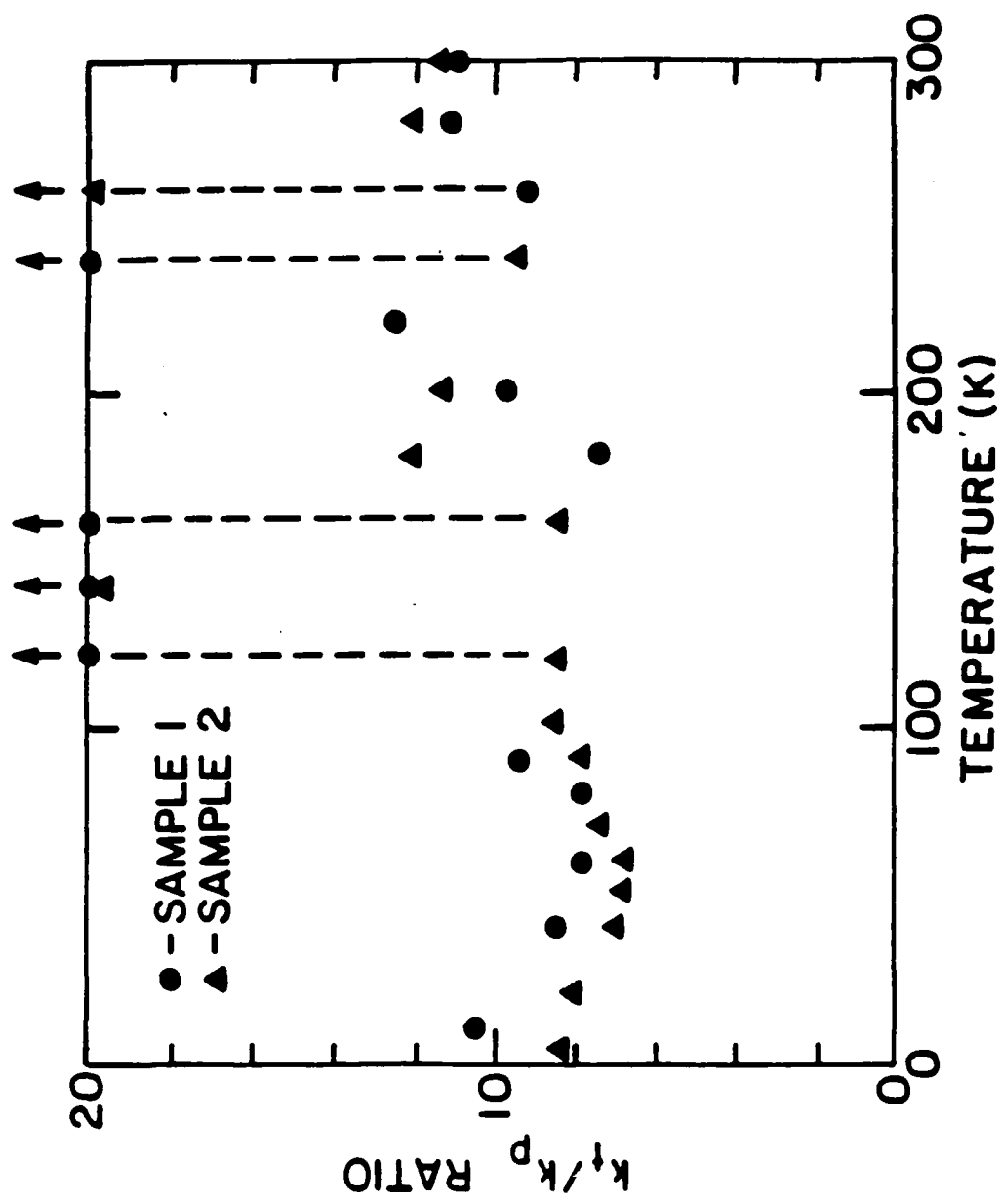


Figure 4(b)

## Associated Programs

## MICROWAVE DIELECTRIC PROPERTIES OF ANTIFERROELECTRIC LEAD ZIRCONATE

M.T. Lanagan, J.H. Kim, S.J. Jang, and R.E. Newnham  
Pennsylvania State University, University Park, PA 16802

## ABSTRACT

The dielectric properties of ceramic lead zirconate and rutile are presented at microwave frequencies. Several techniques are required to span the frequency range from 100 Hz to 26 GHz, and rutile is utilized as a reference material to determine the consistency between measurement methods. A significant relaxation was seen for lead zirconate. At 10 GHz, the dielectric constant decreased 20 percent from the 1 MHz value of 160, and the dielectric loss increased by more than three times the low frequency value of 0.007.

## INTRODUCTION

The requirement of rapid data transmission has lead to an increased interest in the gigahertz region ( $10^9$  Hz), and has prompted research of dielectric materials at microwave frequencies. Material properties in the microwave range have become important to several industries during the past decade. Packaging technology<sup>1</sup> and communication systems<sup>2</sup> rely on dielectric materials with low loss and high temperature stability.

Lead zirconate was selected as a candidate material for high frequency use because of its high dielectric constant and low loss at 1 MHz. The purpose of this study is to develop techniques for the microwave dielectric measurement of lead zirconate, and to determine its utility as a high frequency dielectric material. Ferroelectric materials such as  $\text{BaTiO}_3$  have high dielectric constants, but go through a dielectric relaxation in the microwave region<sup>3</sup>. The large dielectric loss at microwave frequency renders barium titanate undesirable for many applications. It was hypothesized that antiferroelectric lead zirconate would not experience a dielectric relaxation, and the dielectric loss would be small at microwave frequencies.

A survey was made to determine the most suitable microwave techniques for the dielectric property characterization of  $\text{PbZrO}_3$  (herein designated PZ). Reviews of dielectric measurement at high frequency have been made by several authors<sup>4-8</sup>. The selection of a proper technique

depends upon the dielectric properties, frequency range, sample geometry, and available equipment. Theory as well as practical limitations are discussed to provide a basis for method selection.

High frequency dielectric measurement techniques can be divided into two basic categories. Transmission techniques measure dielectric properties through a broad frequency range, and are useful for observing dielectric relaxation in materials. Advanced technology and design have increased the accuracy and speed of transmission techniques to a useful level<sup>9</sup>. Resonant techniques determine dielectric properties at fixed frequencies, which are limited by the type and geometry of the resonant cavity. The accuracy of these techniques is usually higher than transmission methods, particularly for materials with low loss.

The dielectric properties of PZ have been studied by other authors<sup>10-12</sup>. One feature of the reviewed literature is the large variation of dielectric constants reported at room temperature (dielectric constants range from 62 to 110 at 1 MHz). This discrepancy gives strong evidence that consistent processing of PZ is difficult. In this study, the range of dielectric constant values between samples is 14 percent.

#### SAMPLE PREPARATION

Lead zirconate specimens were produced by the mixed oxide method, and the starting powders were electronic grade  $\text{PbO}^*$  and  $\text{ZrO}_2^{**}$ . An excess of 2.9 percent zirconia was added to account for ignition losses and the added weight of the hafnium impurity concentration (2 percent). Vibratory milling was carried out in alcohol for 8 hours with zirconia grinding media. The alcohol was removed, and the powder calcined at 900 °C for 8 hours.

Disks 3.5 cm diameter and 0.3 - 0.7 cm thick were pressed, and sintered at 1300 °C for 2 hours. The high firing temperature made lead atmosphere control crucial for maintenance of a stoichiometric compound. The samples were placed between two platinum foils in an alumina

---

\* Hammond Lead Co.

\*\* Magnesium Elektron E10 grade

crucible, and the foil-sample system was buried in PZ powder. The pellets had a weight loss during sintering, and PZ powders were batched with 1.5 weight percent excess PbO to account for the lead loss. The surface of the samples had a lighter color than the bulk, which signified that more lead was lost at the surface. The specimens were machined until color gradients in the specimens were no longer observed. All samples were sintered to above 95 percent theoretical density.

All peaks in the X-ray diffraction pattern correspond to the PZ structure as shown in Fig. 1. The average grain size was determined from scanning electron microscope images to be 5 microns. The calcined powder was examined for impurities by semi-quantitative spectrographic analysis and no trace elements (Si, Ti, Al, Mg, Fe) were observed above 0.02 percent.

## MEASUREMENT METHODS

Dielectric constant and loss measurements between 100 Hz and 1 MHz were carried out by conventional LCR bridge measurements. The sintered samples were polished, and sputtered gold electrodes were placed on the disk faces. Capacitance and loss measurements were obtained from Hewlett-Packard (abbreviated HP) 4274A and 4275A LCR bridges. Dielectric constant was calculated from the sample dimensions and capacitance data. The dielectric constant and loss at 1 MHz were determined for rutile ( $\epsilon'_r = 95$ ,  $\tan \delta = 0.005$ ) and PZ ( $\epsilon'_r = 160$ ,  $\tan \delta = 0.007$ ).

The lumped impedance method was introduced by von Hippel<sup>7</sup> and was further developed by other authors<sup>13-15</sup>. The lumped capacitance method is used primarily between 10 MHz and 2 GHz, which makes the conventional circuitry of an LCR bridge undesirable. Impedance cannot be determined from measured voltage and current parameters, and must be obtained from a complex reflection coefficient.

The sample holder is designed to be compatible with commercially available coaxial air lines, which have center and shield conductor diameters of 3.04 and 7.00 mm respectively. The sample holder and 50 ohm coaxial line are attached by an APC-7 connector, as shown in Fig. 2. Lumped impedance measurements are carried out by placing a sample on the end of a coaxial line, and shorting the opposite side by a moveable plunger. The piston is made of brass, and is positioned by



a screw for retaining sample placement. The sample diameter is equivalent to the center conductor diameter for all of the lumped impedance measurements. Typical sample geometries are disks 3 mm in diameter and 1 mm thick, which are sputtered with gold on the two disk faces to ensure proper electrical contact.

The coaxial air line assembly is adjoined to a vector measurement system. An HP 4191A impedance analyzer is used to measure the complex reflection coefficient from 45 MHz to 1 GHz. The complex reflection coefficient  $\Gamma^*$  can be expressed in terms of a magnitude  $\Gamma$  and angle  $\theta$ . Before measurement, a calibration is performed by placing known standards (short, open, and a matched load) on the end of the coaxial air line. The dielectric properties are calculated from the following equations:

$$\epsilon_r' = \frac{2\Gamma \sin \theta}{\omega C_0 Z_0 (\Gamma^2 + 2\Gamma \cos \theta + 1)} - \frac{C_f}{C_0} \quad (1)$$

$$\epsilon_r'' = \frac{1 - \Gamma^2}{\omega C_0 Z_0 (\Gamma^2 + 2\Gamma \cos \theta + 1)} \quad (2)$$

The complex reflection coefficient (magnitude,  $\Gamma$ , and angle,  $\theta$ ) is obtained directly from the impedance analyzer. The capacitance  $C_0$  equals  $A\epsilon_0/t$ , where  $A$  is the sample area,  $t$  is the sample thickness, and  $\epsilon_0$  is the permittivity of free space. The impedance of the coaxial air line  $Z_0$  equals 50 ohms, and  $\omega$  is the angular frequency. Complex permittivity ( $\epsilon^* = \epsilon' - j\epsilon''$ ) can be related to the dielectric constant ( $\epsilon'/\epsilon_0 = \epsilon_r'$ ) and the dielectric loss ( $\tan \delta = \epsilon''/\epsilon'$ ). A correction,  $C_f$ , is made for the real part of the permittivity<sup>15</sup> to account for the fringe fields around the sample.

The dielectric properties of rutile and lead zirconate are plotted on Fig. 3 as a function of frequency. The dielectric constant of rutile was 91.7 at 300 MHz, which was within 5 percent of the 1 MHz value. The dielectric loss of rutile was significantly higher than measurements reported by other authors<sup>7</sup>. A dielectric loss of 0.0002 at 10 GHz has been reported<sup>7</sup>, thus showing the difficulty of low loss measurement by the lumped impedance method. The dielectric loss of rutile

demarcated the lower limit of the lumped impedance technique, and the loss values of PZ were higher than those for rutile at an equivalent frequency.

The error in dielectric property measurement became significant for higher frequencies. This was due to the inadequate modeling of the electric field within the sample. The utility of the lumped impedance technique is limited because the electric field in the sample must be uniform, and the assumption loses validity at high frequency and dielectric constant due to wave compression. The useful measurement range of the lumped impedance method is between 10 MHz and 300 MHz for ceramic lead zirconate.

The distributed transmission method does not require the uniform field assumption, and has been used up to 26 GHz in this study. Microwave propagation through a dielectric slab is measured in terms of attenuation and phase, from which the dielectric properties are calculated. The measurement apparatus is illustrated in Figs. 4 and 5.

The transmission coefficient,  $S_{21}$ , is a complex number that can be separated into magnitude,  $|S_{21}|$ , and phase. The S-parameter,  $S_{21}$ , is described as the ratio of the incident wave voltage on port 2 divided by the voltage departing port 1. The magnitude of  $S_{21}$  is measured for rutile and lead zirconate samples loaded in a waveguide. The frequency range of interest is dependent upon the waveguide geometry. The bands used in this study are the X-band ( $h=1.27$ ,  $w=2.29$  cm) and the K-band ( $h=0.43$ ,  $w=1.07$  cm) with frequency ranges of 8.2-12.4 and 18-26.5 GHz respectively.

A response calibration with a through connection is required to obtain accurate  $|S_{21}|$  measurements. Special calibration kits are not needed for this type of calibration, and any band can be used within the frequency range of the HP 8510T system (0.045 to 26.5 GHz). The ports are attached to flange adapters by coaxial cables, and the system is interfaced with an HP 9816 computer for data acquisition and manipulation. The sample holder assembly is shown on Fig. 5. and consists of a dielectric sample completely filling a waveguide flange. Air gaps between sample and waveguide have a deleterious effect on the measured dielectric properties.

A relationship is derived between the complex scattering parameter,  $S_{21}$ , and the dielectric properties of a material<sup>16,17</sup>.

$$S_{21} = \frac{(1 - \rho^2) \exp(-\gamma l)}{1 - \rho^2 \exp(-2\gamma l)} \quad (3)$$

Dielectric property information is contained in the  $\rho$  and  $\gamma$  coefficients as shown in equations 4 and 5. The thickness of the dielectric slab is  $l$ .

$$\rho = \frac{1 - (\epsilon_r^*)^{1/2}}{1 + (\epsilon_r^*)^{1/2}} \quad (4)$$

The propagation coefficient,  $\gamma$ , can be expressed in terms of the real and imaginary parts of the permittivity for low loss materials<sup>7</sup>.

$$\gamma = \alpha + j\beta = j(\mu^* \epsilon^*)^{1/2} \quad (5)$$

where,

$$\alpha = (\pi(\epsilon'')^{1/2} \tan \delta) / \lambda_0 \quad (6)$$

$$\beta = (2\pi(\epsilon')^{1/2}) / \lambda_0 \quad (7)$$

In equations 5-7,  $\epsilon'$  is the real part of the permittivity,  $\lambda_0$  is the free space wavelength, and  $\mu^*$  is the complex permeability. Equations 3-7 are derived for a transverse electromagnetic wave propagating through a nonmagnetic material.

Figure 6 is a plot of  $|S_{21}|$  for rutile loaded in an X-band waveguide. The  $|S_{21}|$  measured data are depicted as points, and theoretically calculated values from equation 3 are shown as a curve. The theoretical fit of Fig. 6 is made by assuming a dielectric constant of 96.0 and a dielectric loss of 0.001, and an excellent correlation is made with actual data. Lead zirconate was also measured by this technique and the results are shown on Fig. 7. The peaks are not as sharp as in Fig. 6, because lead zirconate has a higher dielectric loss than rutile ( $\epsilon'_r = 129.1$ ,  $\tan \delta = 0.026$ ).

The  $|S_{21}|$  peak frequency is a function of dielectric constant, and the position is extremely sensitive to small variations. The peak values correspond to an integral number of half waves contained within the thickness of the sample. Dielectric constant is determined by measuring the frequency of  $|S_{21}|$  maxima, and the sample thickness. The method is accurate for materials that do not experience a significant relaxation in the frequency range of interest, in this case from 8 to 12 GHz. The dielectric constant is calculated from the electromagnetic wavelength contained in the sample along the thickness direction.

$$\epsilon'_r = \left( \frac{\lambda_0}{\lambda_d} \right)^2 + \left( \frac{\lambda_0}{\lambda_c} \right)^2 \quad (8)$$

In the above equation,  $\lambda_0$ , the free space wavelength is determined from  $|S_{21}|$  maxima. The wavelength in the dielectric,  $\lambda_d$ , is obtained from the sample thickness,  $th$ , and the estimated number of half waves,  $n$ , in the sample ( $\lambda_d = 2 \cdot th/n$ ). The cutoff wavelength of the waveguide is  $\lambda_c$ . Equation 8 has an eigenvalue solution, and it is desirable to have several  $|S_{21}|$  peaks for confirmation of the dielectric constant. The frequency difference between two maxima defines a half wavelength contained within the sample. Similar methods have been presented earlier by other authors 18-20.

The magnitude of the transmission peak decreases as the dielectric loss increases. The real part of the permittivity is substituted into equation 3 to find the imaginary part. An iterative technique is performed by estimating a loss value and calculating  $|S_{21}|$ . The estimated dielectric loss is changed to reduce the difference between calculated and measured  $|S_{21}|$  values. In summary, the peak frequency determines the dielectric constant, and the loss is calculated from the transmission magnitude.

A perturbation resonance method was developed for high dielectric constant samples<sup>21</sup>, which utilizes a cylindrical cavity with a transverse magnetic mode ( $TM_{010}$ ) resonance. The TM cavity is depicted in Fig. 8. Coupling loops are placed at opposite sides of the TM cavity to maximize interaction with the magnetic field. The sample is a one centimeter long rod with a cross

section area of one square millimeter, which is positioned at the cavity center. The length was adjusted by a moveable plate at the bottom, and the top plate is detached for sample removal. The dielectric constant and the loss tangent are obtained by the following equations:

$$\epsilon_r' = 1 + 0.539 \frac{A_c}{A_s} \frac{f_2 - f_1}{f_2} \quad (9)$$

$$\tan \delta = \frac{0.269 A_c}{\epsilon_r' A_s} \left( \frac{1}{Q_2} - \frac{1}{Q_1} \right) \quad (10)$$

In equations 9 and 10,  $A_c$  is the cross sectional area of the cavity and  $A_s$  is the specimen area. The subscripts 1 and 2 refer to the cavity and cavity-plus-sample systems, respectively. The variable  $Q$  is the quality factor, which is determined from the resonant frequency  $f_c$  and the peak width  $\Delta f$ , ( $Q=f_c/\Delta f$ ), where  $\Delta f$  is the difference between the 3dB points.

Two cavities were made for dielectric measurement at 3.04 and 5.60 GHz, and had diameters of 77 and 41 mm respectively. The resonant frequencies were determined from the HP 8510T network analyzer, and the dielectric properties were calculated. An important contribution to error is resonant cavity stability. The cavity has to be disturbed to remove the sample, and it is difficult to return the cavity to its previous state. This causes a measurable change in resonant frequency and quality factor. Other contributions to error include measurement of the sample dimensions, which can be as high as 5 percent for small samples. Dielectric loss accuracy was a function of the dielectric constant error and the quality factor of the cavity. Sample dielectric losses below 0.002 were difficult to measure by this method.

A resonant post technique<sup>4,22</sup> was studied, and it was found that the dielectric loss of PZ is too large for dielectric property determination. However, rutile was measured at 7.3 GHz ( $\epsilon_r'=97.5$ ,  $\tan \delta=3.6 \times 10^{-4}$ ).

## RESULTS AND DISCUSSION

Microwave dielectric data of rutile are gathered from the presented techniques, and shown on Fig 9. The dielectric constant and loss of ceramic rutile decrease with frequency up to 1 MHz due to conductivity, and are independent of frequency in the GHz range. High frequency dielectric loss is measured most accurately by the resonant post method. The lumped impedance, TM cavity, and distributed transmission methods give higher loss values for rutile. The dielectric loss for rutile was set as a lower limit below which the accuracy of these techniques was questionable. The dielectric constants measured by the TM cavity and lumped impedance methods are within 5 percent of the 1 MHz value, and the resonant post and distributed transmission methods are within 2 percent.

The same high frequency dielectric measurement methods for rutile were also utilized for PZ, with the exception of the resonant post technique. The most accurate technique for the dielectric measurement of PZ at microwave frequency is the distributed transmission method. A dielectric relaxation is found for lead zirconate in the microwave region. Figure 10 portrays a decrease in the dielectric constant with a corresponding increase in the dielectric loss.

Similar dielectric relaxations have been observed for single crystal<sup>3</sup> and ceramic  $\text{BaTiO}_3$ <sup>23</sup>, which is a ferroelectric material. Devonshire<sup>24</sup> proposed a piezoelectric grain or domain resonance as a relaxation mechanism. The model was strongly supported by the work of Yao<sup>25</sup> on ferroelectric  $\text{LiNbO}_3$ . Kittel<sup>26</sup> has proposed domain wall motion as a possible explanation for the dielectric relaxation of barium titanate in the microwave region.

The dielectric relaxation caused by piezoelectric grain resonance is not expected for PZ, which has centric symmetry<sup>27</sup> (space group  $\text{Pbam}$ ). The ferroelectric effect is a possible mechanism for domain wall movement under an applied field for antiferroelectric  $\text{PbZrO}_3$ . The ferroelectric effect is defined as an inequality of domain state energies caused by anisotropy in permittivity. Attempts were made to detect ferroelectricity through electric field dependence of the dielectric constant, which was found to be independent of field up to 11 Kv/cm. The effect is usually weak, and it is therefore concluded that the domain wall motion contribution to permittivity is small.

Possible contributions to the dielectric relaxation of PZ include both intrinsic and extrinsic mechanisms. A low lying far infrared lattice mode has been observed for lead zirconate, and Kramers-Kronig analysis has shown it to contribute over 90 percent of the dielectric constant<sup>28</sup>. The observations in microwave region may suggest that the relaxation of the low lying lattice mode is just beginning to occur. Other authors have found a correlation of lattice defect concentration with dielectric loss at microwave frequency<sup>29,30</sup>. The lead species is volatile at the temperatures needed to process PZ, and vacancies are probable. A correlation between lattice defects and the magnitude of dielectric relaxation for PZ is a subject for future study.

The dielectric properties of antiferroelectric PZ at microwave frequency are compared with paraelectric  $\text{Ba}(\text{Zn}_{1/3}\text{Ta}_{2/3})\text{O}_3$  and ferroelectric  $\text{BaTiO}_3$  in Table 1. The large dielectric loss exhibited by barium titanate is due to a large relaxation in the microwave region. Paraelectric materials such as  $\text{Ba}(\text{Zn}_{1/3}\text{Ta}_{2/3})\text{O}_3$  have very low loss, and are suitable for microwave resonator applications. Lead zirconate has a smaller dielectric loss than barium titanate, but the loss is too large for a useful resonator material.

## CONCLUSIONS

Several techniques were necessary to measure dielectric constant and loss of lead zirconate up to 26 GHz. Rutile was used as a control material to ensure accuracy and consistency between the measurement techniques. The LCR bridge method was utilized up to 1 MHz, and the lumped impedance measurement between 10 MHz and 300 MHz. Accuracy of the lumped impedance technique became questionable above 300 MHz, due to the inability to fully characterize the electromagnetic fields in the sample region. Dielectric properties were determined by the TM cavity method at fixed frequencies of 3.0 and 5.4 GHz, and by the transmission technique in the X and K-bands. The dielectric loss of PZ was found to be too high for the resonant post measurement.

A definite dielectric relaxation was seen for  $\text{PbZrO}_3$  at microwave frequencies. It was difficult to calculate the magnitude of intrinsic and extrinsic contributions to the microwave relaxation, and there is a possibility that both may exist. Identification of possible loss mechanisms for lead zirconate is a subject of further research.

#### ACKNOWLEDGEMENTS

The authors are grateful to Dr. L.E. Cross and Dr. D.C. Dube for their helpful suggestions, to Mr. P. Moses for his computer programming, to Ms. J. Yamamoto and Mr. D. Brenneman for their help. The project was sponsored by the Center for Dielectric Studies.



## REFERENCES

- 1) L.E. Cross and T.R. Gururaja, "Ultra-low dielectric permittivity ceramics and composites for packaging applications," *Proc. of the Mater. Res. Soc.*, **72**, 53-65 (1986)
- 2) K. Wakino, "High frequency dielectrics and their applications," *Proc. of the sixth IEEE Int. Sym. on App. of Ferroelectrics*, 97-106 (1986)
- 3) T.S. Benedict, and J.L. Durand, "Dielectric properties of single domain crystals of  $\text{BaTiO}_3$  at microwave frequencies," *Phys. Rev.*, **109**, [4], 1091-1092, (1958)
- 4) M.T. Lanagan, "Microwave Dielectric Properties of Antiferroelectric Lead Zirconate," Ph. D. Thesis, The Pennsylvania State University, (1987)
- 5) J. Chamberlain and G.W. Chantry ed., "High frequency dielectric measurement," *Proceedings of a Tutorial Conference on Measurement of High Frequency Dielectric Properties of Materials*, Teddington, UK: IPC Science and Technology Press.(1973)
- 6) A.C. Lynch, "Precise measurements on dielectric and magnetic materials," *IEEE Trans. on Instrument. and Meas.*, **IM-23**, [12], 425-431, (1974)
- 7) A.R. von Hippel, *Dielectric Materials and Applications*, Cambridge, MA: MIT Press. (1966)
- 8) H. M. Altschuler, Chapter 9. In M. Sucher and J. Fox (Eds.) *Handbook of Microwave Measurements*, **2**, (3rd ed.) NY: Polytechnic Press. (1963)
- 9) Hewlett-Packard, "Measuring dielectric constant with the HP 8510T network analyzer," Product Note 8510-3
- 10) Y.M. Poplavko, "Study of microwave dielectric dispersion in ferroelectrics of various types," *Proc. of the Int. Meeting on Ferroelectrics.*, **2**, 171-179. (1966)
- 11) Y.M. Poplavko and V.G. Tsykalov, "Investigation of antiferroelectrics at millimeter wavelengths," *Sov. Phys.-Solid State*, **9**, [11], 2600-2603 (1968)
- 12) S. Roberts, "Dielectric properties of lead zirconate and barium-lead zirconate," *J. Am. Ceram. Soc.*, **33**, [2], 63-66 (1950)
- 13) M.A. Stuchly and S.S. Stuchly, "Coaxial line reflection methods for measuring dielectric properties of biological substances at radio and microwave frequencies - A review," *IEEE Trans. on Instrument. and Meas.*, **IM-29**, [3], 176-183 (1980)
- 14) S.S. Stuchly, M.A. Rzepecka, and M.F. Iskander, "Permittivity measurements at microwave frequencies using lumped elements," *IEEE Trans. on Instrument. and Meas.*, **IM-23**, [1], 56-62 (1974)
- 15) M.F. Iskander and S.S. Stuchly, "Fringing field effect in the lumped-capacitance method for permittivity measurement," *IEEE Trans. on Instrument. and Meas.*, **IM-27**, [1], 106-107 (1978)
- 16) M.J.C. van Gemert, "High-frequency time-domain methods in dielectric spectroscopy," *Phillips Res. Repts.*, **28**, [R844], 530-572 (1973)
- 17) L.P. Ligthart, "A fast computational technique for accurate permittivity determination using transmission line methods," *IEEE Trans. on Microwave Theory and Tech.*, **MTT-31**, [3], 249-254. (1983)

- 18) D. Rytz, M.B. Klein, B. Bobbs, M. Matloubian, and H. Fetterman, "Dielectric properties of  $\text{KTa}_{1-x}\text{Nb}_x\text{O}_3$  at millimeter wavelengths," Proc. of the Sixth Inter. Meeting on Ferroelectrics., Supplement of Jap. J. of App. Phys., **24**, [2], 1010-1012. (1985)
- 19) A. Rost and O. Kersten, "Messung komplexer dielektrizitätskonstanten im X-band," Hermsdorfer Tech. Mitt. Heft., **57**, 1826-1831 (1981)
- 20) J.G. Powles and W. Jackson, "The measurement of the dielectric properties of high-permittivity materials at centimetre wavelengths," Proc. Inst. Elect. Engrs., **96**, [856], 383-389 (1949)
- 21) E. Nakamura and J. Furuichi, "Measurement of microwave dielectric constants of ferroelectrics: Part 1 dielectric constants of  $\text{BaTiO}_3$  single crystal at 3.3 kMc/s," J. Phys. Soc. Jap., **15**, [11] 1955-1960 (1960)
- 22) B.W. Hakki and P.D. Coleman, "A dielectric resonator method of measuring inductive capacities in the millimeter range," IRE Trans. on Microwave Theory and Tech., MTT-8, [7], 402-410 (1960)
- 23) A.R. von Hippel, "Ferroelectricity, domain structure, and phase transitions of barium titanate," Revs. Modern Phys., **22**, [3], 221-237 (1950)
- 24) A.F. Devonshire, "Theory of barium titanate: Part II," Phil. Mag., **42**, [333], 1065-1079 (1951)
- 25) X. Yao, H. McKinstry, and L.E. Cross, "The influence of piezoelectric grain resonance on the dielectric spectra of  $\text{LiNbO}_3$  ceramics," J. Am. Ceram. Soc., **66**, [9], 637-641 (1983)
- 26) C. Kittel, "Domain boundary motion in ferroelectric crystals and the dielectric constant at high frequency," Phys. Rev., **83**, [2], 458 (1958)
- 27) H. Fujishita, Y. Shiozaki, N. Achiwa, and E. Sawaguchi, "Crystal structure determination of antiferroelectric  $\text{PbZrO}_3$ -application of profile analysis method to powder method of x-ray neutron diffraction," J. of the Phys. Soc. of Japan, **51**, [11], 3583-3591 (1982)
- 28) C.H. Perry, D.J. McCarthy, and G. Rupprecht, "Dielectric dispersion of some perovskite zirconates," Phys. Rev., **138**, [5a], 1537-1538 (1965)
- 29) K. Wakino, M. Murata, and H. Tamura, "Far infrared reflection spectra of  $\text{Ba}(\text{Mn}_{1/3}\text{Ta}_{2/3})\text{O}_3$  -  $\text{BaZrO}_3$  dielectric resonator material," J. Am. Ceram. Soc., **69**, [1], 34-37 (1986)
- 30) B.D. Silverman, "Microwave absorption in cubic strontium titanate," Phys. Rev., **125**, [6], 1921-1930 (1962)

## FIGURE CAPTIONS

- Figure 1. Indexed X-ray powder pattern of Lead Zirconate sintered at 1300 °C for 2 hours.
- Figure 2. Schematic of the sample holder assembly for lumped impedance measurement.
- Figure 3. The dielectric properties of PZ and Rutile measured by the lumped impedance method. The solid line is dielectric constant and the broken line is loss.  
(o = Rutile and  $\Delta$  = Lead Zirconate)
- Figure 4. The HP 8510T network analyzer system with sample holder for use with the distributed transmission method.
- Figure 5. Sample holder assembly with specimen for waveguide measurement.
- Figure 6.  $|S_{21}|$  measured for an X-band waveguide loaded with a rutile sample.  
Comparison is made between data (points) and theoretical calculation (solid line).
- Figure 7.  $|S_{21}|$  measured for an X-band waveguide loaded with a PZ sample.  
Comparison is made between data (points) and theoretical calculation (solid line).
- Figure 8. Schematic of the TM cavity with specimen.
- Figure 9. Dielectric properties of rutile measured by various microwave techniques.  
The solid line is dielectric constant and the broken line is loss. Bars are not shown for points that have error within the area of a marker.  
( $\square$  = LCR,  $\diamond$  = Lumped Impedance,  $\Delta$  = TM Cavity, o = Resonant post, and X = Transmission)
- Figure 10. Dielectric properties of PZ measured by various microwave techniques.  
The solid line is dielectric constant and the broken line is loss.  
Bars are not shown for points that have error within the area of a marker.  
( $\square$  = LCR,  $\diamond$  = Lumped Impedance,  $\Delta$  = TM Cavity, and X = Transmission)

TABLE I

Dielectric Property Comparison between Antiferroelectric, Ferroelectric,  
and Paraelectric Ceramics

Material	Frequency GHz	Dielectric Constant	Dielectric Loss	Reference
PbZrO <sub>3</sub>	10	128	0.04	
BaTiO <sub>3</sub>	9.5	300	0.53	20
Ba(Zn <sub>1/3</sub> Ta <sub>2/3</sub> )O <sub>3</sub>	7	30.4	0.0001	29

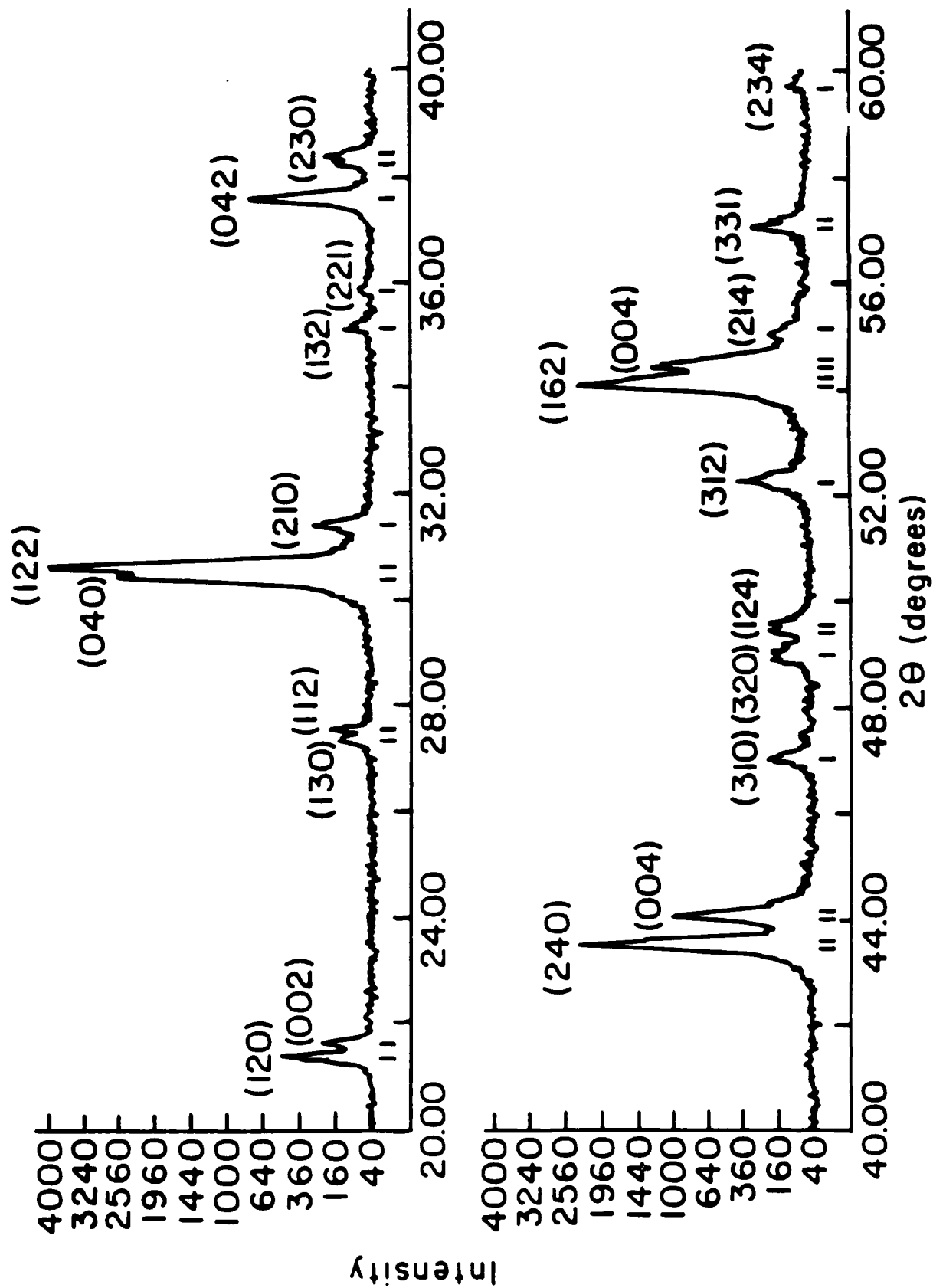
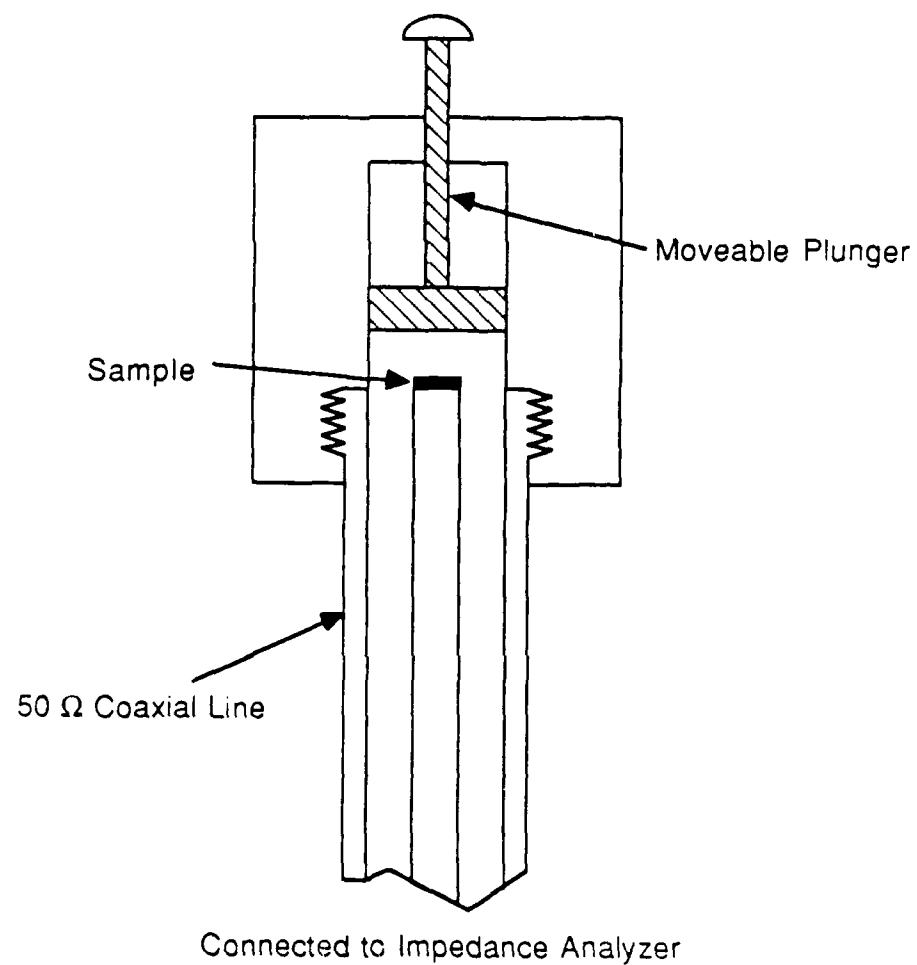


Fig 1



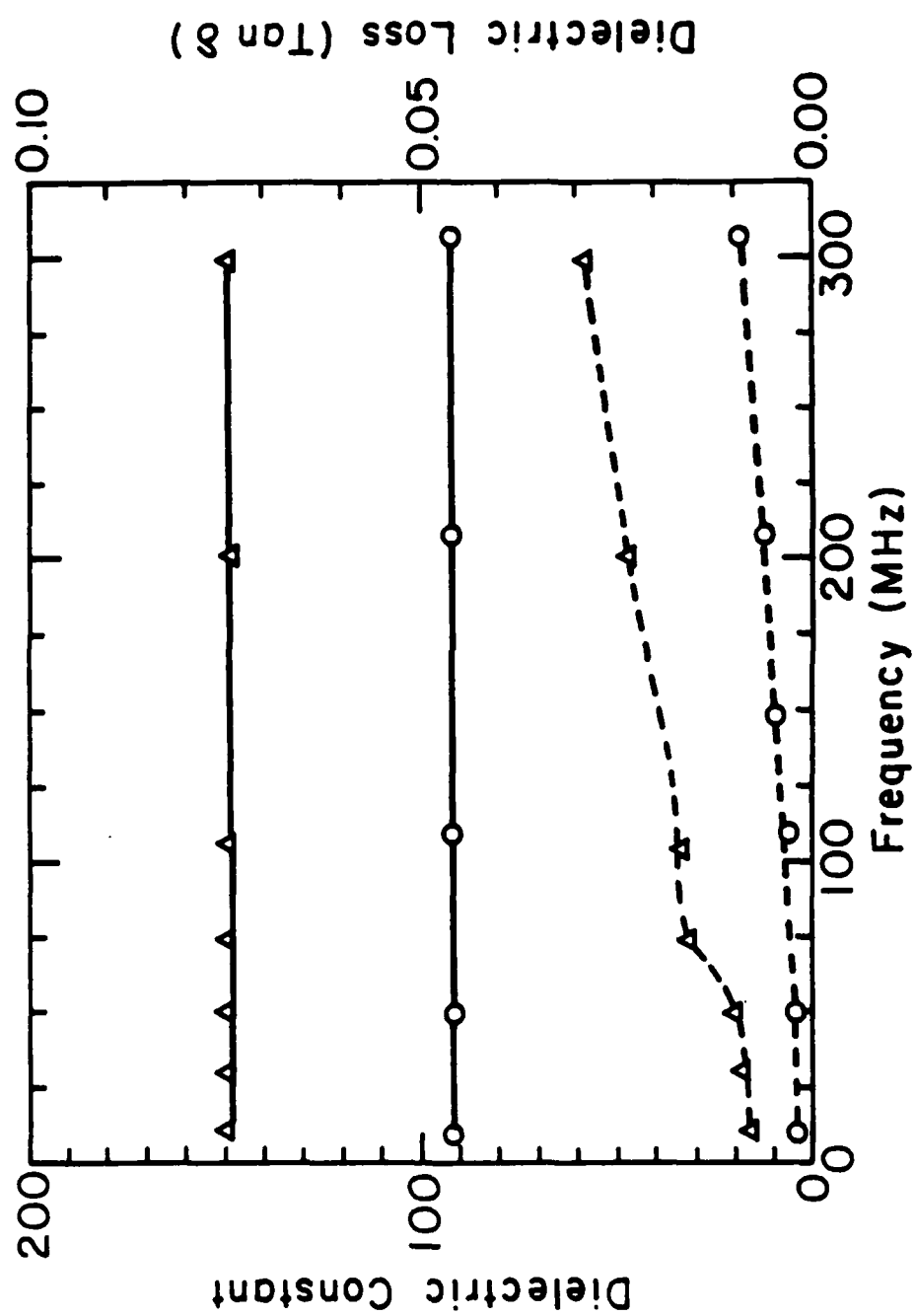


Fig. 3

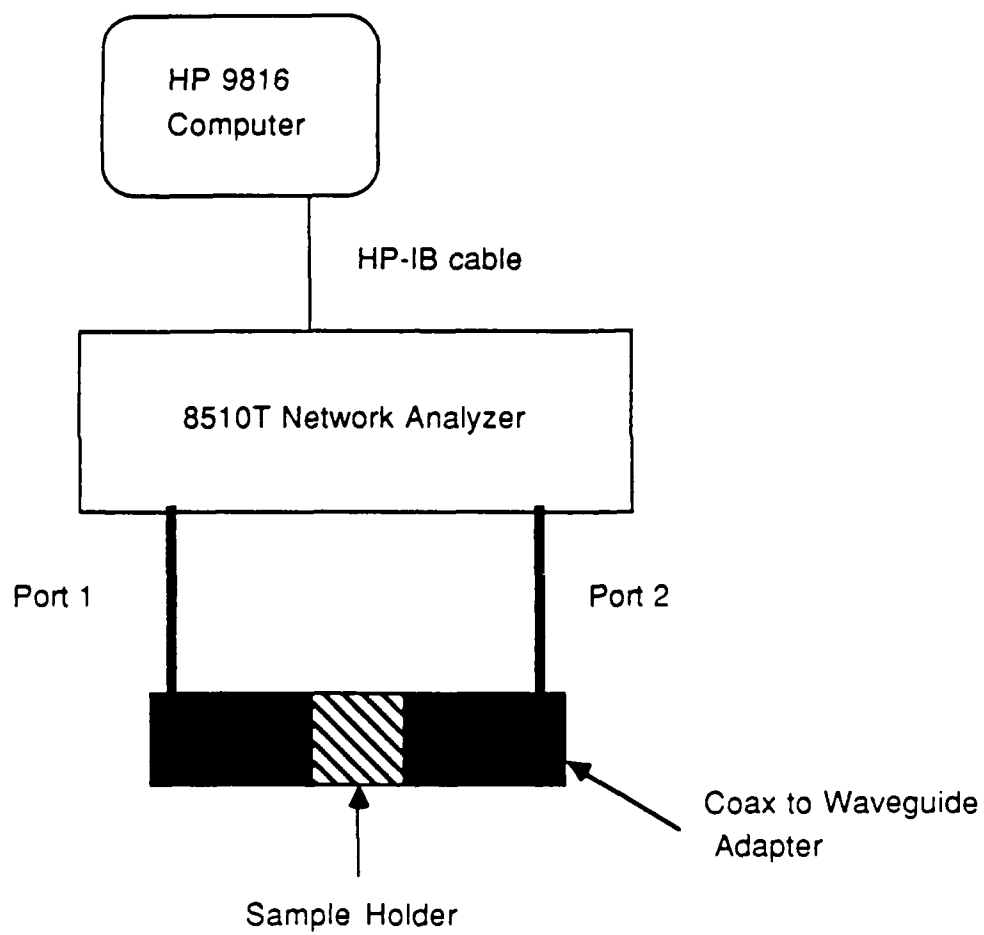


Fig 4



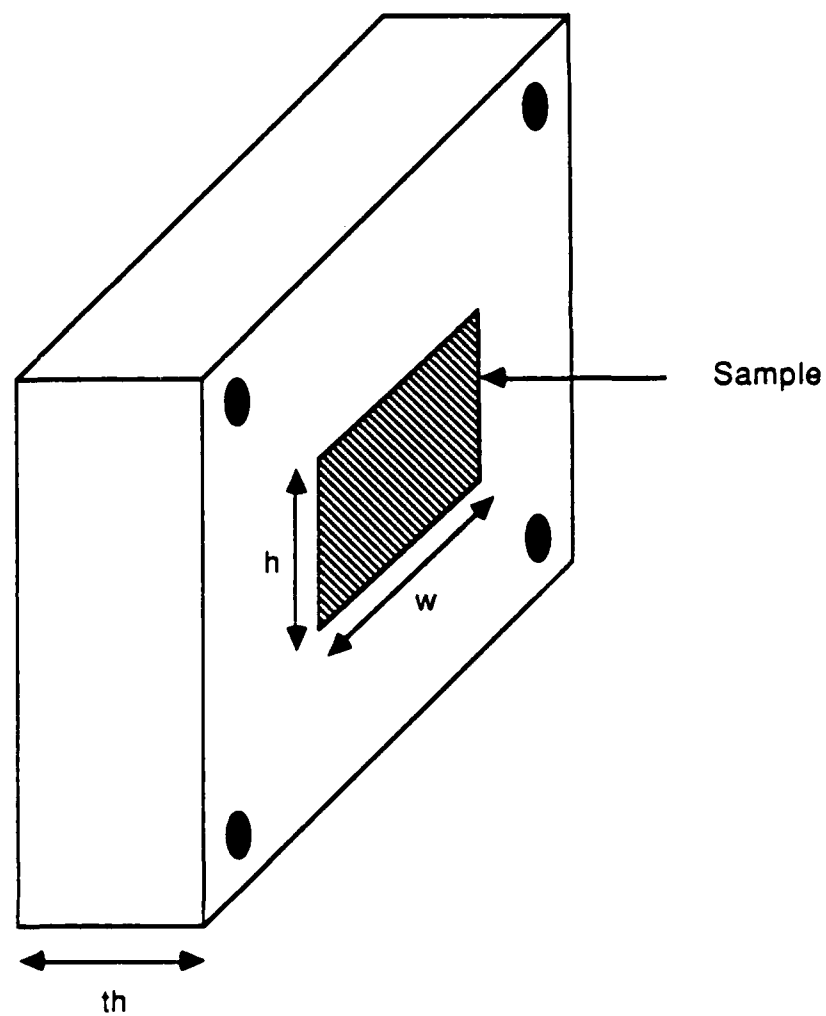


Fig 15

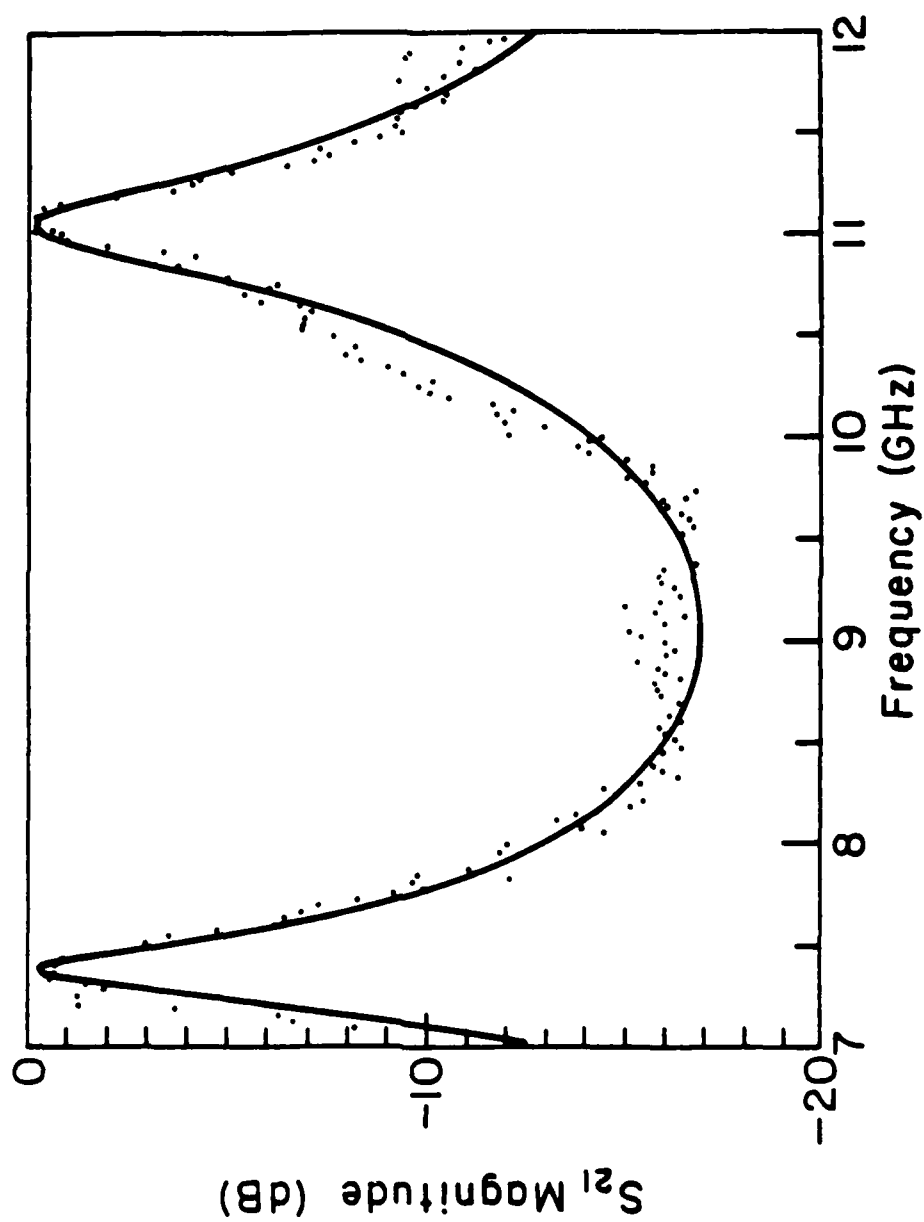


Fig 6

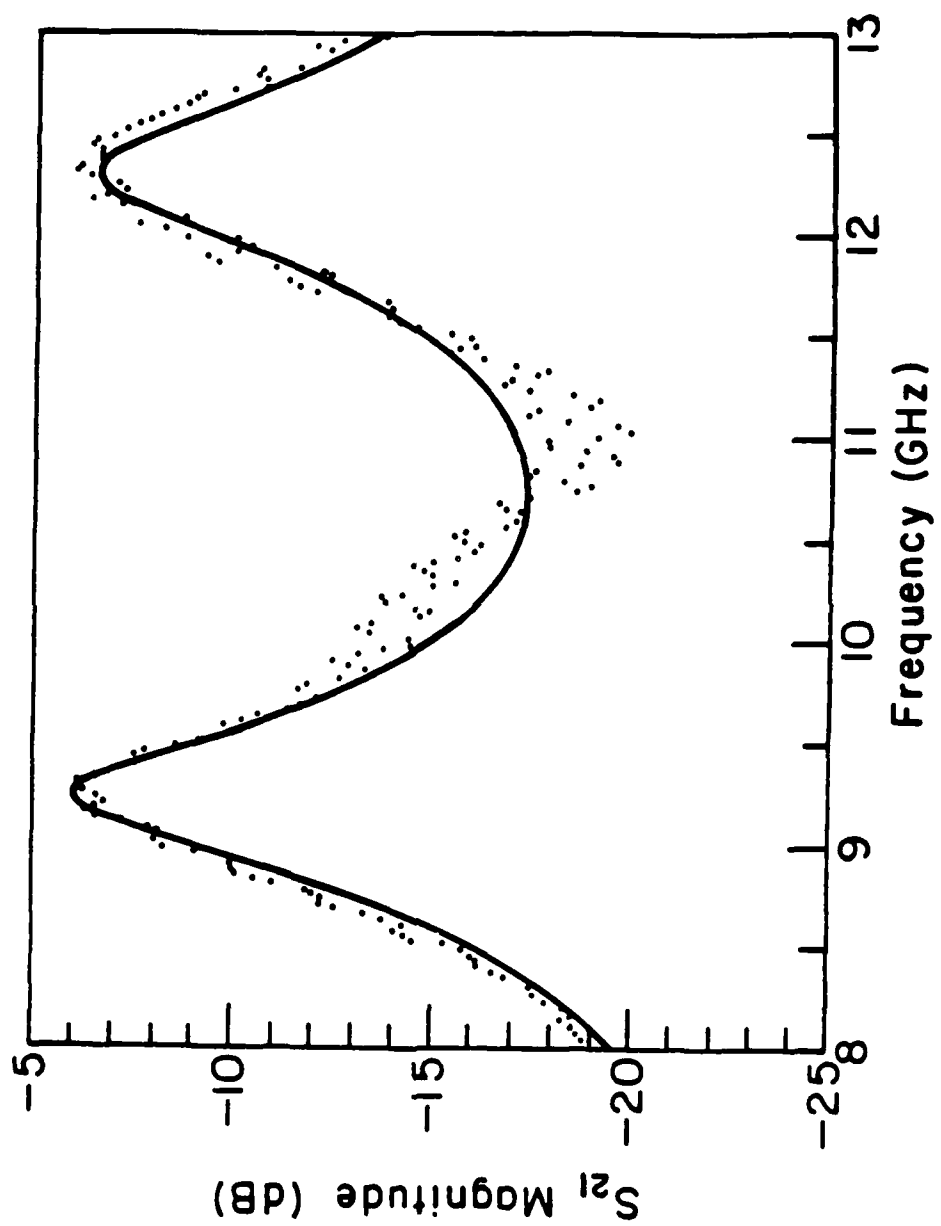


Fig 7

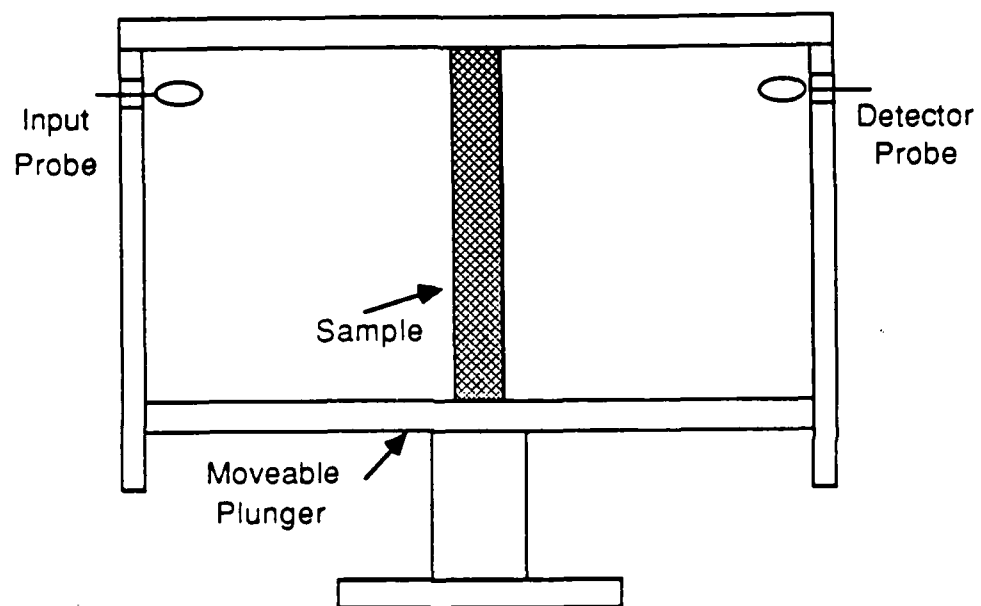


Fig 8

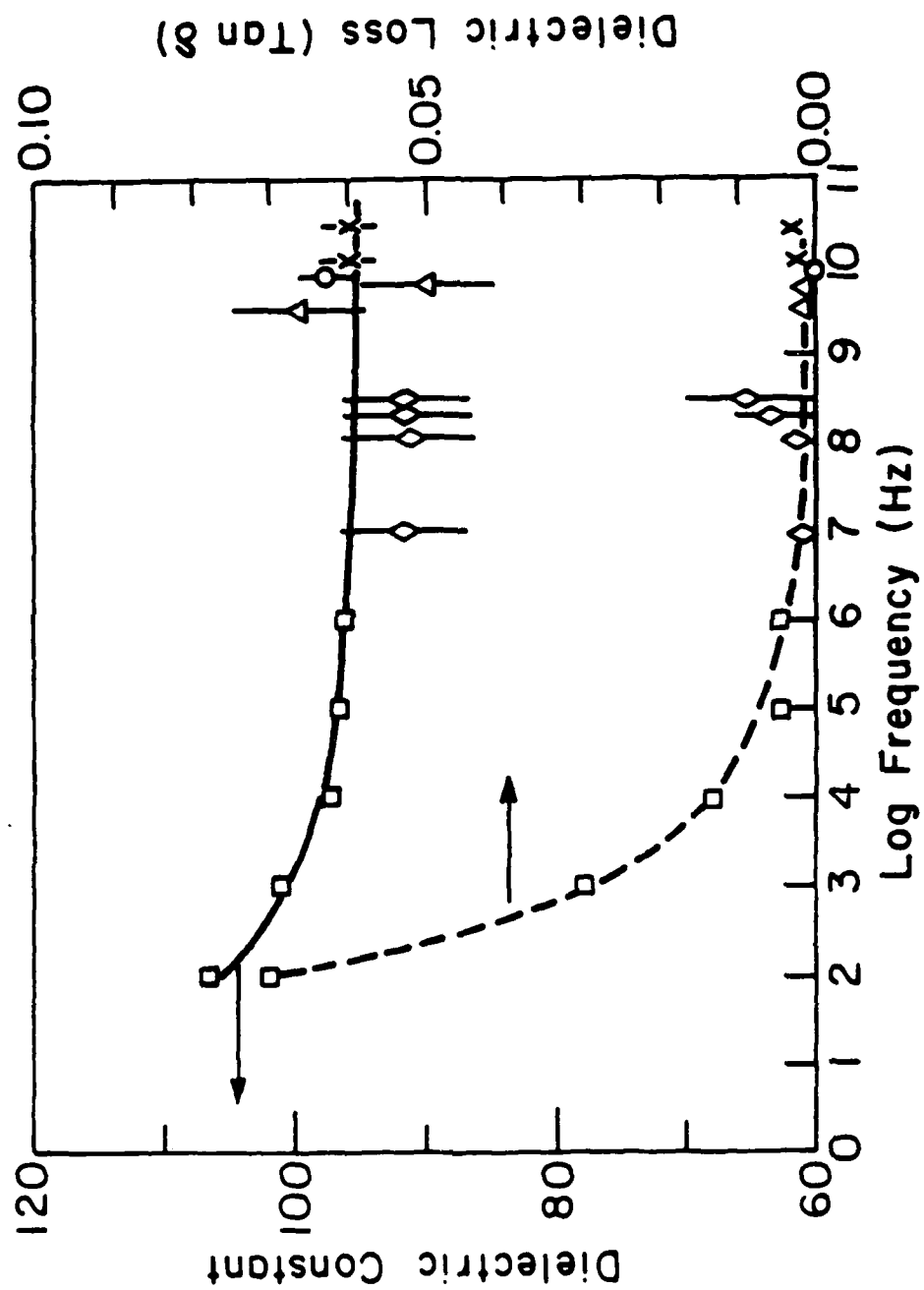


Fig 9

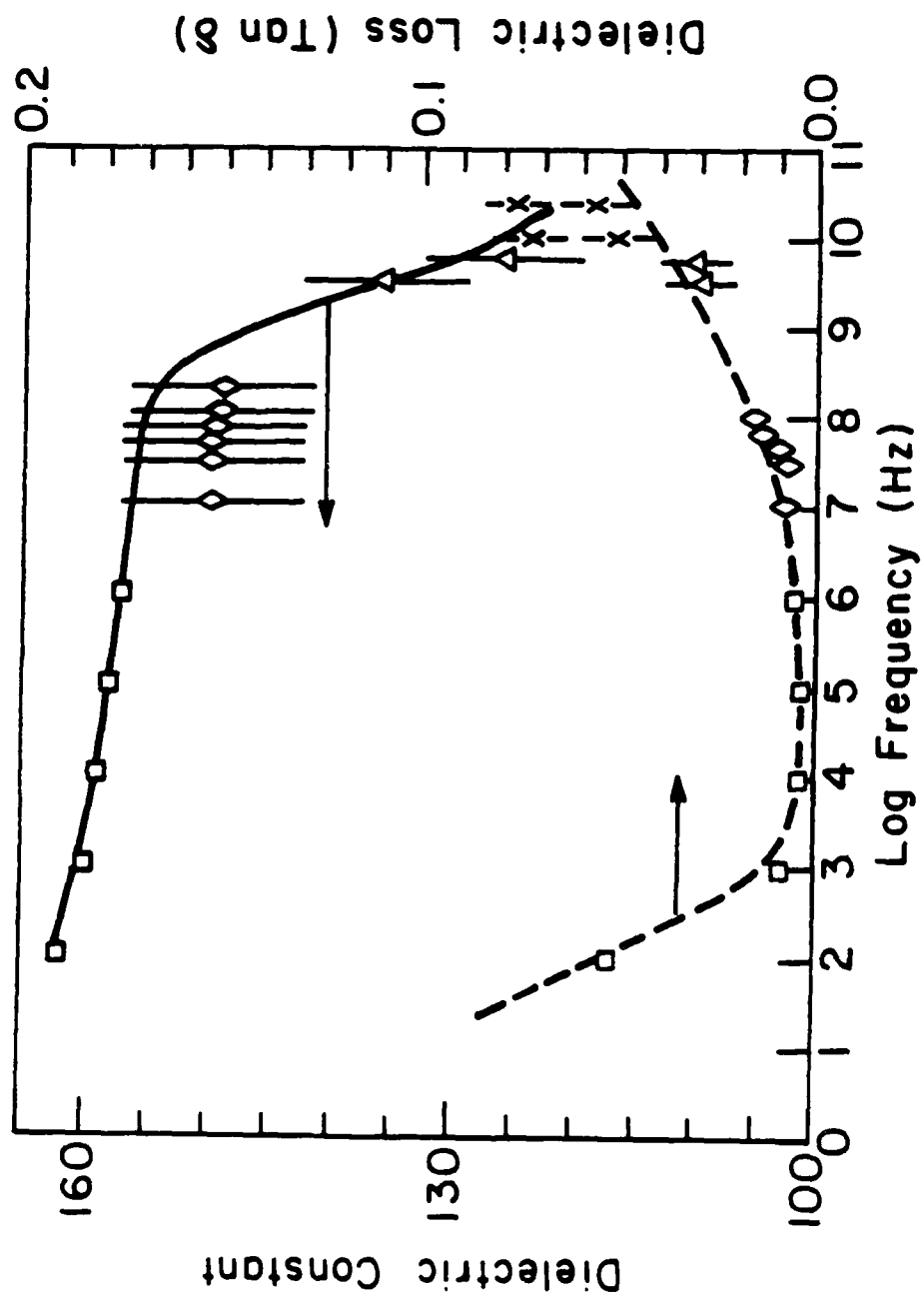


Fig 10

# EXPERIMENTAL ANALYSIS OF FERROELECTRIC DOMAIN LAYER WAVE

Xing-Jiao. Li\*, Wuyi. Pan and L. E. Cross

Materials Research Laboratory

The Pennsylvania State University

University Park , PA 16802

## 1 INTRODUCTION

The concept of a ferroelectric domain layer wave FDLW and a theoretical analysis about the nature of the wave in a  $180^\circ$  domain structure were published in earlier papers<sup>1,2,3</sup>. In this paper, experimental evidence about the FDLW in  $180^\circ$  ferroelectric domain structure is obtained by using contra-poled PZT ceramics as a model structure. The existence of the wave is verified from the attenuation and dispersion characteristics of the observed propagation. In the demonstration, low frequencies were used to avoid problems with the grainy nature of the walls in the PZT ceramic.

## 2 THE EQUATIONS OF FERROELECTRIC DOMAIN LAYER WAVE

From the theoretical analysis, there exists a ferroelectric domain layer mode in a two layer  $180^\circ$  ferroelectric domain structure. For convenience, the thickness of the first layer substrate will be assumed to be infinite and the thickness of the second layer is equal to  $h$ . The equations for the amplitudes of displacement and potential of the FDLW will be:<sup>1</sup>

\* Visiting professor from Huazhong University of science and Technology,  
P.R.China

In type I Domain (thin plate)

$$U_3^I = C^{(5)} \exp(\beta k x_1) + C^{(6)} \exp(-\beta k x_1)$$

$$= (-\beta B / eA - 1) C^{(6)} \exp(\beta k x_1) + C^{(6)} \exp(-\beta k x_1), \quad (1)$$

$$\Phi^I = (B/A + e/e) C^{(6)} \exp(\beta k x_1) - e/e C^{(6)} \exp(-\beta k x_1)$$

$$- (B/A + C\beta/e) C^{(6)} \exp(k x_1) - B/AC^{(6)} \exp(-k x_1) \quad (2)$$

In type II domain (substrate)

$$U_3^{II} = C^{(5)} \exp(\beta k x_1) = -(eB/eA) C^{(6)} \exp(\beta k x_1) \quad (3)$$

$$\Phi^{II} = B/AC^{(6)} \exp(\beta k x_1) - C\beta/e C^{(6)} \exp(k x_1) \quad (4)$$

where

$$A = 2e \sinh(hk) - (e/e) \exp(\beta hk),$$

$$B = 2C\beta \cosh(\beta hk) - C\beta \exp(hk),$$

$$\bar{C} = 2e \sinh(hk) - 2e_0 \cosh(hk) + e_0 \exp(\beta hk),$$

$$D = 2(e_0 e / e) \sinh(\beta hk) + (e_0 + e) \exp(hk) C\beta / e \quad (5)$$

Where  $e$  is  $e_{11}$  (the dielectric permittivity perpendicular to the polar direction,  $e$  is  $e_{15}$  (the piezoelectric matrix component,  $C$  is  $\bar{C}_{44}$  (the elastic matrix component),  $\beta = (1 - \rho v^2 / C_{44})$  (where  $\rho$  is the density of the material and  $v$  is the velocity of the acoustic wave),  $C^{(6)}$  corresponds to the amplitude of M-T mode and  $C^{(5)} = (Be/eA - 1)C^{(6)}$ . (Readers may referred to reference 1 for the detail physical meaning of the symbols).



In order to have nontrivial solution, the following compatibility condition must be satisfied

$$\begin{vmatrix} A & B \\ \bar{C} & D \end{vmatrix} = 0$$

This is the dispersion equation of the ferroelectric domain layer wave in the 2 layer  $180^\circ$  ferroelectric domain structure.

### 3 TRANSMISSION ATTENUATION OF PZT FDLW GUIDE

In FDLW system, if the input is a sinusoidal function of known frequency and constant amplitude, then the output will also be a sinusoidal function of the same frequency but with modified amplitude and phase. So, the FDLW is a linear system. The information about the displacement amplitude and the electric potential from transfer function of the waveguide can be obtained from the output signal of the waveguide. But, these quantities in the above equation are complicated. For simplicity, we consider only the relation between the displacement amplitude of FDLW in the domain wall and  $hk$  and that between the magnitude of voltage generated by the FDLW in the wall and  $hk$ . When  $x_f=0$ , the equations are :

$$U_3^I|_{x_1=0} = U_3^{\Pi}|_{x_1=0} = (-\epsilon B/eA)C^{(6)} \quad (7)$$

$$\Phi^I|_{x_1=0} = \Phi^{\Pi}|_{x_1=0} = -(B/A)C^{(6)} - (C\beta/e)C^{(6)} \quad (8)$$

Figure 1 is the illustration of equations (7) and (8). The material parameters for a typical

PZT sample are  $\rho=7526 \text{ kg/m}^3$ ,  $\epsilon_{11}/\epsilon_0=1000$ ,  $e_{15}=8.83 \text{ C/m}^3$ ,  $C_{44}=3.9 \times 10^{11} \text{ N/M}^2$

In Figure 1, the amplitude of displacement has been normalized to  $C^{(6)}$  which is the displacement amplitude of the Bleustein-Gulyaev surface wave on the free surface.

It should be noted that when  $hk=0.05$ , there exists a maximum amplitude for the domain layer mode in the domain wall. It is two times that of the B-G surface wave and that of the Maerfeld-Tounois domain wall wave. As the  $hk$  value continues to increase, the amplitude at the domain wall will decrease. Until as  $hk$  approaches infinity,

$U_3$  is asymptotic to  $C^{(6)}$  which correspond to the amplitude of M-T mode, or of the domain wall mode.

The amplitude of the electric potential has been normalized arbitrarily to  $(e/\epsilon - C\beta/e)C^{(6)}$ . The change in electric potential patterns due to an increasing  $hk$  has a maximum at  $hk = .009$ . As  $hk \rightarrow \infty$  it is equivalent to that of the M-T mode, or of the domain wall wave. It should be noted that the potential amplitude of the FDLW in the domain wall is not equal to zero, while that of domain wall wave is always equal to zero.

The shaded region represents the region of  $hk$  within which the measurements were carried out and is determined by the thickness of the layer, the central frequency which is layer thickness dependent and the band width of the interdigital transducer used, which is also layer thickness dependent. One of the reasons for selecting this region is that the layer plate can not be made so thin that  $hk \ll 1$  in the present device. If the layer is a film, for which the thickness is of the order of  $\mu\text{m}$ , then the operating frequency may be raised into the MHz region.

We use two uniformly polarized PZT ceramics plates to make up the wave guide. The structure consists of a 13 mm thick PZT plate and a 1 mm thick PZT layer (the length and width are 60 mm and 13 mm respectively). The plates are "gluebonded" together with their polar axes oriented antiparallel to each other. The FDLW wave is a shear-type wave which travels perpendicular to the polar axis with the displacement along the polar direction. The guided wave is confined to ferroelectric domain layer, as shown in Figure 2A. The length of wave guide is 4.2cm. The length of the transducer is 1.2cm. The sample for the ferroelectric domain wall wave is shown in Figure 2B. The

sample for the B-G wave is shown in Figure 2C

According to the special needs of our experiment, we made the following selections in the design of the interdigital transducer used :

(a). In order to select the region of  $hk$  around that of the velocity valley for the FDLW, we picked the center frequency  $F=380$  kHz. For the PZT, SAW velocity  $v=2240$  m/s,

then  $\lambda = 6 \cdot 10^{-3}$  m if the dispersion is ignored

(b) The design of the interdigital finger structure for the transducer is shown in Figure 3.

The number of the interdigital periods selected is 2 to have large frequency band width

around the minimum velocity.

(c) To reduce the interdigital transducer reflection, wave front distortion and coupling efficiency, we selected the single-double IDT. The space between neighbouring fingers is

equal to  $\lambda/6$ .

(d) Because of the size of the sample (substrate), The aperture is not theoretically optimum. This will yield more diffraction and triple-transit signals and result in larger ripples within the pass band. The sidelobe level only degrades slowly. Because the number of the interdigital periods of the transducer is only two, this may also yield more bulk wave.

The IDTs that launch and receive the waves are designed to operate at a wavelength of approximately one half the plate(substrate) thickness. This would normally cause higher order plate modes or bulk waves which would interfere with the experiment. However, in our experiment, the input transducer was evaporated on the substrate. Taking this step, we can damp the plate mode in the thick substrate.

In order to illustrate three cases for the device configurations in Figure 2 A, 2B and 2C, we put three curves of frequency response shown Figure 4. These curves are obtained from a HP 3570 A network analyzer and a HP 3330 automatic frequency synthesizer, where  $B-A = 20 \log(V_{out}/V_{in})$ . Figure 4 shows the traces of FDLW, B-G surface wave and M-T wave. The solid curve in Figure 4 is a manifestations of

equation(1),(2),(3) and (4) in the case of finite  $hk$ , the dashed curve in the case of  $hk \rightarrow \infty$  and the dotted curve in the case of  $hk \rightarrow 0$ . The amplitudes and frequencies of the input signals generated in the network analyzer are the same for all of these three waves. We can see directly from the Figure that the attenuation of the frequency response of the FDLW( even though in region  $hk \sim 1$ ) is much less than that of the B-G and the M-T waves. The peak values of FDLW is -10.6 dB, M-T domain wall wave -14 dB and B-G surface wave -17 dB.

In the pass band of the frequency response curves shown in Figure 4, there are some large ripples. These are due to diffraction effect, bulk wave and terminal reflection as already described.

In order to analyze the characteristics of the FDLW waveguide transmission, Obviously, we should level out the piezoelectric transformation loss from the whole attenuations, so that we can compare the waveguide transmission characteristics.

To calculate the piezoelectric transformation loss, we manufactured two B-G wave delay lines with same material and IDT but different delay distances then we measured the whole attenuations (B-A) near the center frequency respectively. Since B-G wave transmission attenuation per unit length should be fixed. So we have

$$(B-A)_1 - A_T/L_1 = (B-A)_2 - A_T/L_2 \quad (9)$$

where  $A_T$ ,  $L_1$  and  $L_2$  are piezoelectric transformation loss and delay distances of the two B-G wave delay lines respectively.

From equation(9), we can obtain the piezoelectric transformation loss  $A_T$ . Then we can also obtain the relation between waveguide transmission and the frequency of the acoustic wave.

The transmission attenuation of the B-G wave near the center frequency is about 2 dB/cm and the ripple of attenuation near the center frequency is rather large, this may be caused by diffraction effect from the transducers with the rather small transducer

aperture.

The transmission attenuation of the M-T wave near the center frequency is about 1.64 dB/cm. The ripple of the transmission attenuation for the M-T wave is less than that of the B-G wave. The reason for this phenomenon is probably due to the energy concentration near the domain wall so that the open acoustic wave transmission is avoided.

The transmission attenuation of the domain layer wave near the central frequency is about 1.2 dB/cm which is much smaller than that of the B-G wave or the M-T wave. Furthermore, the attenuation ripple of the domain layer wave is also much smaller than those of the B-G and the M-T waves. This demonstrates that the transmission characteristics of domain layer wave is significantly better than that of the B-G waveguide or the M-T waveguide and the domain layer waveguide have small divergence and better coincidence.

#### 4 THE INSERTION LOSS AND BANDWIDTH OF THE FDLW WAVEGUIDE

When the smoothness of the waveguide interface is degraded, the damping of the waveguide increases. Then, besides the decreased ripples, PZT FDLW waveguide has lower insertion loss, larger relative bandwidth and sharper transition band as shown in Figure 5. The peak value of frequency response curve is -11.6 dB. Its 3 dB relative bandwidth is above 40%, regardless of the large ripple. The length of waveguide of the sample is 4.2 cm and that of transducer is 1.2 cm. when the transmission attenuation 6 dB is leveled out, the realizable minimum insertion loss approaches -6dB. The ratio between the realizable minimum insertion loss and the relative bandwidth is very good. It may be considered as the pre-shape of the frequency response of a passband filter. It may be considered that PZT ceramics FDLW waveguide has a "plastic" function of frequency response.

For comparison, let us look into the cases of SAW delay. According to the relation between the insertion loss of SAW delay and the maximum relative band width.

$$IL = 10 \log [\pi/k^2 (\Delta f/f_0)^2_{\max}] \quad (10)$$

where  $IL$  represents the insertion loss,  $K^2$  stands for the coupling coefficient and  $\Delta f/f_0$  is the relative bandwidth.

If the realizable maximum bandwidth of saw delay is 40%, the minimum insertion loss is -10.4 dB for  $\text{LiNbO}_3$ , -10.6dB for PZT, -24.9 dB for quartz and -15dB for  $[011]\text{Bi}_{12}\text{GeO}_{20}$ . These ratios ( $IL/(\Delta f/f_0)$ ) are larger than that of FDLW waveguide measured

This phenomenon can be explained as following: the realizable maximum relative bandwidth of a SAW delay line is

$$(\Delta f/f_0)_{\max} = 2[(k^2/\pi)(G/\hat{G}_a + 1)^2]^{1/2} \quad (11)$$

where  $\hat{G}_a$  is the acoustic radiation conductance of transducer at the center frequency,  $G$  is the shunt conductance in the electrical circuit which will be equivalent to the series damping in the waveguide here. This damping includes mechanical and electric dampings. So, if  $G$  is increased or the damping of waveguide is increased as a result, then  $(\Delta f/f_0)_{\max}$  will increase.

At the same time, it should be noted that in the shaded region of Figure 1,  $U_3$  and  $\Phi$  are larger than that of B-G surface wave and the domain wall wave. The signal will be modulated by the amplitude of hyperbolic function of FLDW, Then the tail of the signal will be cut off.

Therefore, a wide relative bandwidth, low insertion loss and sharp transition bands frequency response are obtained.

We may ask a question here. Can one use these behaviours of the electronic information of waveguide to study the state of the domain walls and the grain boundaries (more energy will be concentrated in the layer). Since different mechanical

and electric states of the domain wall, domain layer and grain boundary result in different frequency responses. This study should belong to the area of electronics of ferroelectrics.

## 5 THE ANALYSIS OF DISPERSION CHARACTERISTICS OF FDLW WAVE

Another main property of the guide structure is its dispersive feature. It is worthwhile to note that it is a measure of the interaction between the antiparallel domains. The fact that the "depth" of the dispersion curve is the measure of the

interaction between the antiparallel domains and the possibility of utilizing such a mode in practical electronic devices have stimulated interest in the basic investigation on guidance dispersion. In addition, experiments on the dispersive relation have been conducted leading to the demonstration of the existence of the FDLW itself.

### (1) The experimental analysis of dispersion characteristics of FDLW

We obtained the dispersion curve through measuring the phase velocity of the domain layer wave at different frequencies. There are many kinds of methods to measure the acoustic velocity. We adopted the phase-shift method, namely, we measured the phase shift between the input signal and the output signal using the network analyzer and automatic frequency synthesizer. Obviously

$$v_p = 360 Lf / \phi \quad (12)$$

where  $L$  is the delay distance of FDLW delay line,  $f$  is the signal frequency,  $v_p$  is the phase velocity measured and  $\phi$  is the phase shift.

The curve of velocity vs frequency of B-G wave and M-T wave for poled PZT ceramic measured is approximately undispersed as shown in Figure 6.

The measurement of the velocity vs frequency curves must be made carefully. Because the number of the interdigital periods of the IDT is only two and the

piezoelectric plate is rather thin, the effects of bulk and plate waves must be considered. The experiments have shown that the wave propagating in the above waveguide are not obviously dispersive in the frequency band measured, thus the interference of the bulk wave is considered to be insignificant and therefore not taken in to account. Besides, when these wave guides are with two pairs of interdigital electrodes, the power distribution ratio of surface wave and bulk wave are 72% and 24% respectively. Because the IDT can only excite the bulk wave with frequencies higher than the synchronous frequency, most of the points measured belong to B-G waves and M-T waves. The effect of bulk wave appears only at the upper bound of frequency band as shown in Figure 6. But at the same time, in Figure 4, the sidelobe of the curve of frequency response may be considered to be the effect of diffraction and bulk wave interference.

From equation (6), the theoretical dispersion relation of FDLW is:

$$AD - B\bar{C} = 0 \quad (13)$$

According to this equation, the theoretical dispersion curve of FDLW calculated with the parameters of our PZT samples is shown in Figure 7

The phase difference between the phase of input signal (phase A) and that of output signal (phase B) at different frequencies were measured by the network analyzer. Since the network analyzer only display the phase difference within  $180^\circ$ , the phase shift due to the transducer and to all full cycles must be added.

The theoretical results of the dispersion curve of FDLW indicates that the minimum of the wave velocity appears when  $hk$  equals to 1.1, as shown in Fig.7. We find experimentally that when  $hk = .96$  the velocity reaches a minimum point. The experimental results are in good agreement with the theoretical prediction for the whole frequency range measured, Therefore we believe we have verified the existence of the FDLW. The small difference in phase velocity in the low frequency range is partially due to the fact that the dielectric dispersion was not taken into account for the calculation of the theoretical curve.

(2) The relationship between the material parameter and the dispersion of FDLW waveguide in the 2-layer structure



To explore the manner in which the characteristic parameter of the FDLW will change for different material parameter we consider the situations for the parameters of the piezoelectric constant  $e_{15}$  the dielectric constant  $\epsilon_{11}$  and the elastic constant  $\bar{C}_{44}$ . To simplify consideration each parameter is normalized to the equivalent value for BaTiO<sub>3</sub>. The parameters for the hypothetical materials from M1 through M9 are shown in table 1. The dispersion curves in two layer structures for these hypothetical materials are shown in Figure 8(A) and (B). From the shapes of the curves, it is easily seen that the less  $\epsilon_{11}$  is and the greater  $e_{15}$  is, the deeper is dispersion.

### (3) The effects of number of layers on the dispersion of FDLW waveguide

Starting from general piezoelectric equations, we can formulate the dispersion equation in the N-layer 180° domain structure by a series matrix manipulations. (the detail derivation is too complicated and will be published soon). Let 0-th plane is the infinite distance plane of the substrate, nth plane is free surface, the dispersion equation of the nth interface is:

$$W_{21}(W_{33} - \epsilon_{11}/\epsilon_0 W_{43}) = W_{23}(W_{31} - \epsilon_{11}/\epsilon_0 W_{41}) \quad (14)$$

where  $W_{ij}$  is the element of matrix  $W_a$

$$W_a = (G(h) \cdot G_0^{-1} G^{-1}(h) G_0^{-1})^k G_0 \quad \text{when } N=2k+1, K=1,2,\dots$$

$$= (G(h) G_0^{-1} G(h) G_0^{-1} G(h) G_0^{-1})^k G_0 \quad \text{when } N=2k, K=0,1,\dots$$

$$G(h) = \begin{vmatrix} \exp(bkh) & \exp(-bkh) & 0 & 0 \\ g_1 \exp(bkh) & -g_1 \exp(-bkh) & g_3 \exp(kx) & -g_3 \exp(-kx) \\ g_2 \exp(bkh) & g_2 \exp(-bkh) & g_2 \exp(kx) & g_2 \exp(-kx) \\ 0 & 0 & -g_4 \exp(kx) & g_4 \exp(-kx) \end{vmatrix}$$

$$g_1 = C_{44} \cdot bk$$

$$g_2 = e_{15} / \epsilon_{11}$$

$$g_3 = e_{15}^2 / \epsilon_{11}$$

$$g_4 = e_{15} \cdot k$$

$$G'(x) = \begin{vmatrix} 1 & & & \\ & 1 & & \\ & & -1 & \\ & & & -1 \end{vmatrix} \quad G(x) = E_0 G(x)$$

From equation(14 ) for the poled PZT ceramics, the curve of the dispersion function in an N-layer structure is illustrated in Figure 9 . It is worthwhile to note that the more layers there are, the lower is the minimum of the dispersion curve. For the five layer structure, the velocity of FDLW changes from 2100 m/s to 1900 m/s, decreasing by 20%. For 2-layer structure, it decreases by 16%. Therefore the " depth " of dispersion is related to the number of layers.

#### (4) The measure of the interaction between domains

As the material parameters of the antiparallel domain are identical, the decrease in wave velocity with increase in  $hk$  is not due to the mass loading but to a perturbation interaction, i.e. the mechanical and electric interloading which are corresponding to perturbation in wave number  $(\Delta k/k)_M$  and  $(\Delta k/k)_E$ . This perturbation loading may be considered as an interaction between domains. It is well known  $|\Delta v/v| = \Delta k/k^4$ . from above reason, we may say that the " depth " of dispersion  $\Delta v/v$  is the measure of interaction between 180 domains which is related to material parameters, thickness of domain and the number of the domain layers .

In 2-layer structure <sup>1</sup>, when  $hk \ll 1$   $\Delta k/k = [e^4/(C \epsilon^2(\epsilon_0 + 1))]hk$

From this equation, it is seen that the relation between the interaction of 180 domain and material parameter and thickness of domain In a word, the interaction between the two domain may be changed with the 4 th power of the parameter  $e$ , the 2nd power of the parameter  $\epsilon$  and negative first power of the elastic coefficient  $C$ .

## (5) Discussion

(a) The depth of the dispersion of FDLW, or the interaction between 180 domains, is not only a function of material parameters, a function of the thickness of domain layer  $h$ , but also a function of the number of layers and of the frequency of the FDLW.

(b) From phase shift measurement as shown in Figure 10, group delay  $\tau = d\phi/d\omega$  was calculated. It is shown that in the range of frequency of pass band shown in Figure 5, group delay decrease rapidly from 33  $\mu s$  to 23  $\mu s$ , that is when a signal in this band of frequencies propagating in this waveguide, the time of the signal will be expanded by 10  $\mu s$ . From Figure (9) and (10), if we use the multiple structure or new materials like M4 and M6, The group delay time will be further expanded. As described above, if the operating frequency is raised above meg Hz, the future application should exists.

## 7 SUMMARY AND CONCLUSIONS

Poled PZT ceramics were used to make FDLW, B-G and M-T waveguides. The frequency dependence of the attenuation of these waveguides was measured and compared. It is confirmed that FDLW waveguide has the lowest transmission attenuation in the frequency range (200-800 kHz) of these measurements. Due to its low transmission loss and function of modulating of amplitude, the FDLW waveguide has a better ratio of the realizable minimum insertion loss to relative maximum bandwidth than the other two structures in the frequency range of the measurements. It may be considered that PZT ceramics FDLW waveguide has a "plastic" function of frequency response.

Experimental dispersion curves measured by a phase shift method have been correlated with the theoretically predicted dispersion. The analysis demonstrates that the nature of the changes in dispersion associates with the changes in the dielectric and piezoelectric properties of PZT. The experimentally verified depth of the dispersion may be the measure of the interaction between domains.

There exists ferroelectric domain layer wave in poled PZT ceramics FDLW waveguide. Many applications can be found if the operating frequency can be raised to Meg Hz range.

#### Acknowledgement

The authors wish to thank Hauzhe Cao, Feng Zhou, Hanhu Fen, Juan Wei, Guwei Goa and Yannian Jan who joined this work. The appreciation is extended to Q.Y.Jiang for her help and to Dr.Q.M.Zhang for the helpful discussions.

#### Reference

- 1 Xingjiao Li J.of.Appl. Phys. **61** 2327 (1987)
- 2 Xingjiao Li J.of.Appl. Phys **56** 88 (1984)
- 2 Xingjiao Li Ferroelectrics **47** 3-7 (1983)
- 4 K.M.Lain J.of.Appl. Phys **42** 899-906 (1971)

#### List of Figures

Figure 1: The displacement amplitude in domain wall and the potential amplitude

in domain wall  $U_3 \propto 0$  vs  $hk$   $\phi_{x1} = 0$  vs  $hk$ .

Figure 2A: PZT ferroelectric domain layer waveguide.

Figure 2B: PZT ferroelectric domain wall waveguide.

Figure 2C: PZT B-G waveguide.

Figure 3 The scheme of the interdigital transducer

Figure 4: The curves of frequency response for PZT FDLW, B-G surface and ferroelectric domain wall waveguides.

Figure 5: The curve of frequency response for unpolished interface PZT FDLW waveguide.

Figure 6 : The velocity Vs frequency curves of PZT B-G waveguide and M-T waveguide.

Figure 7 : the dispersion curve of poled PZT FDLW waveguide.( the solid curve represents the theoretical curve; the dashed curve represents the experiment results).

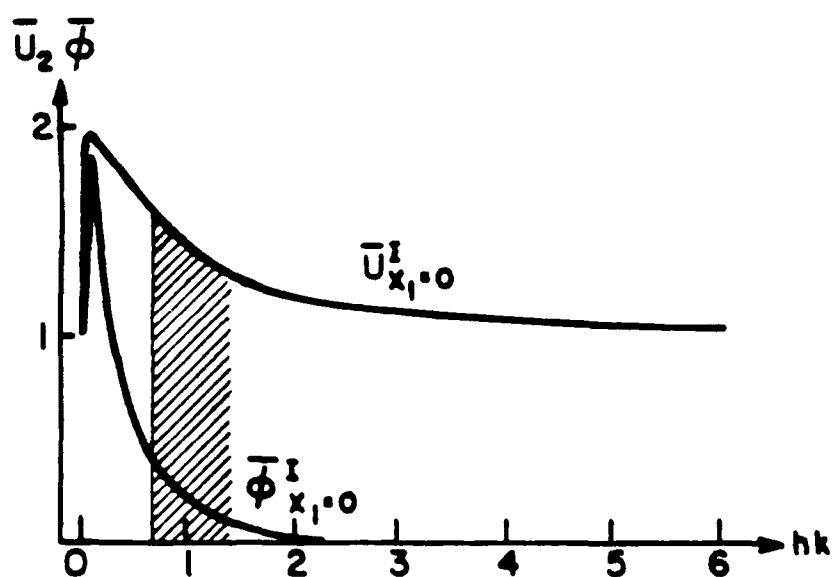
Figure 8(A) and (B): Dispersion of velocity in structure of  $M_1$  - $M_2$  domain layer -containing 2 layers

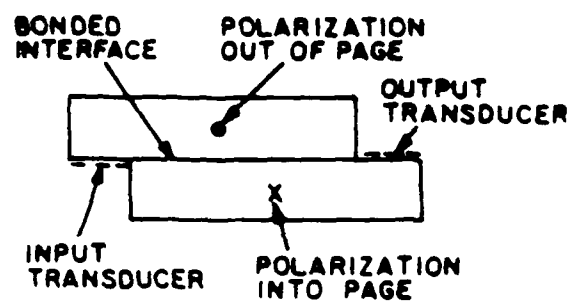
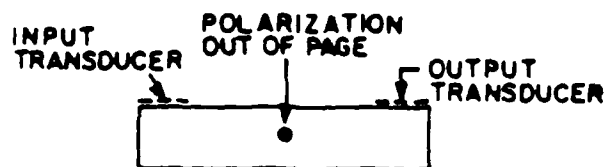
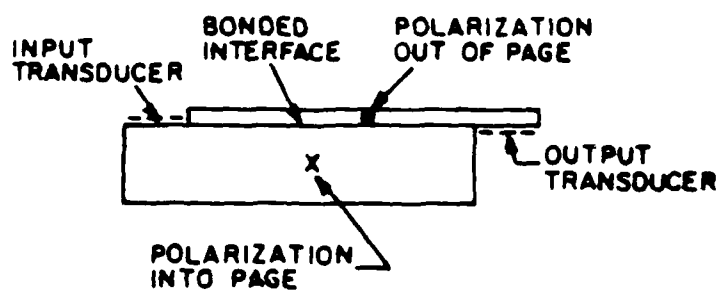
Figure 9 : Dispersion of the velocities in the structure of PZT-2 domain layer- containing 2 to 5 layers.

Figure 10 : Phase shift vs frequency for poled PZT ceramic FDLW waveguide measured by network analyser.

material parameter	M <sub>1</sub>	M <sub>2</sub>	M <sub>3</sub>	M <sub>4</sub>	M <sub>5</sub>	M <sub>6</sub>	M <sub>7</sub>	M <sub>8</sub>	M <sub>9</sub>
$\left(\frac{\epsilon'_{15}}{\epsilon_{15}}\right)^2$	1/2	1/√2	√2	2	1	1	1	1	1
$\frac{\epsilon'_{11}}{\epsilon_{11}}$	1	1	1	1	1	1/2	1/√2	√2	2

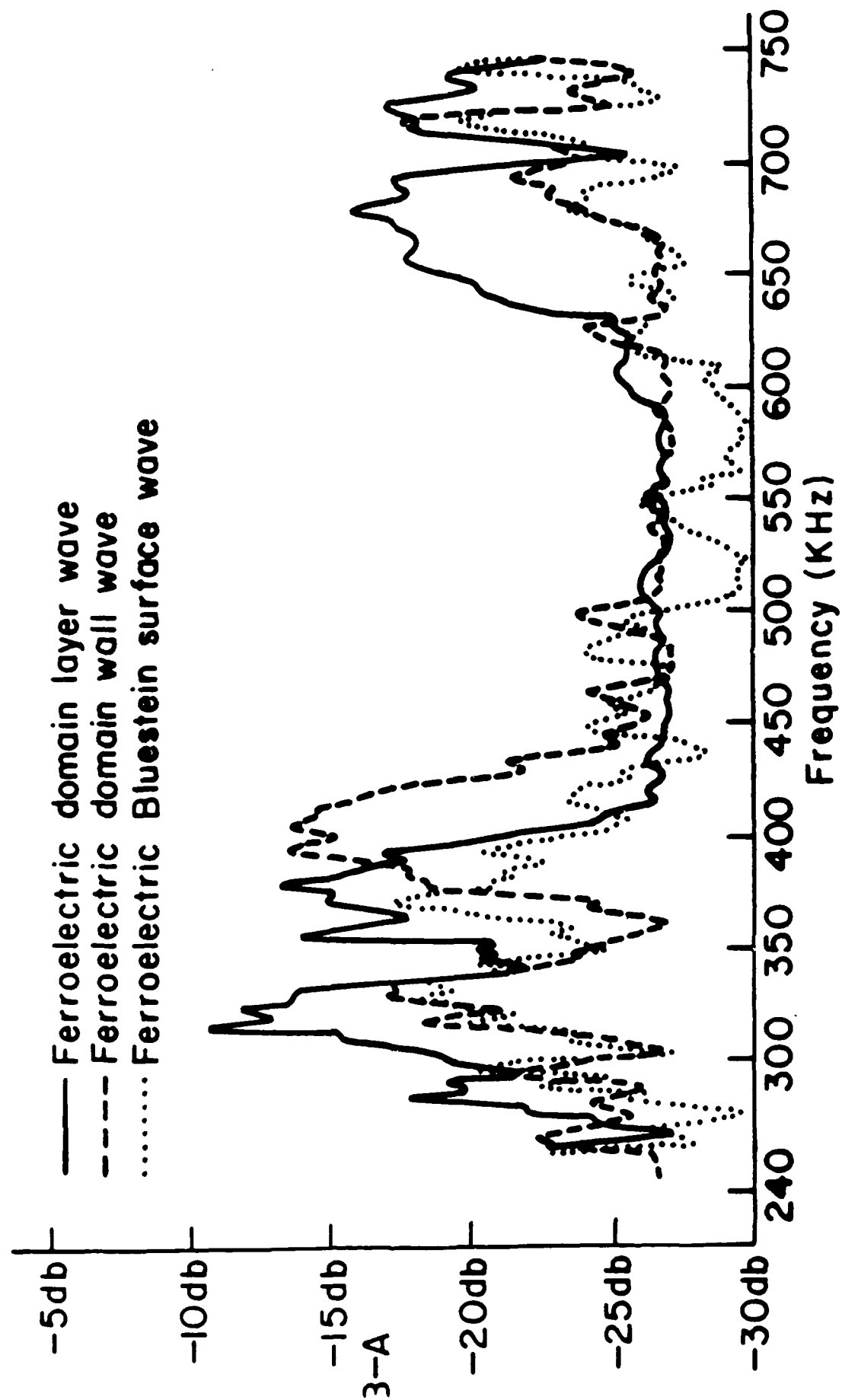
F-36

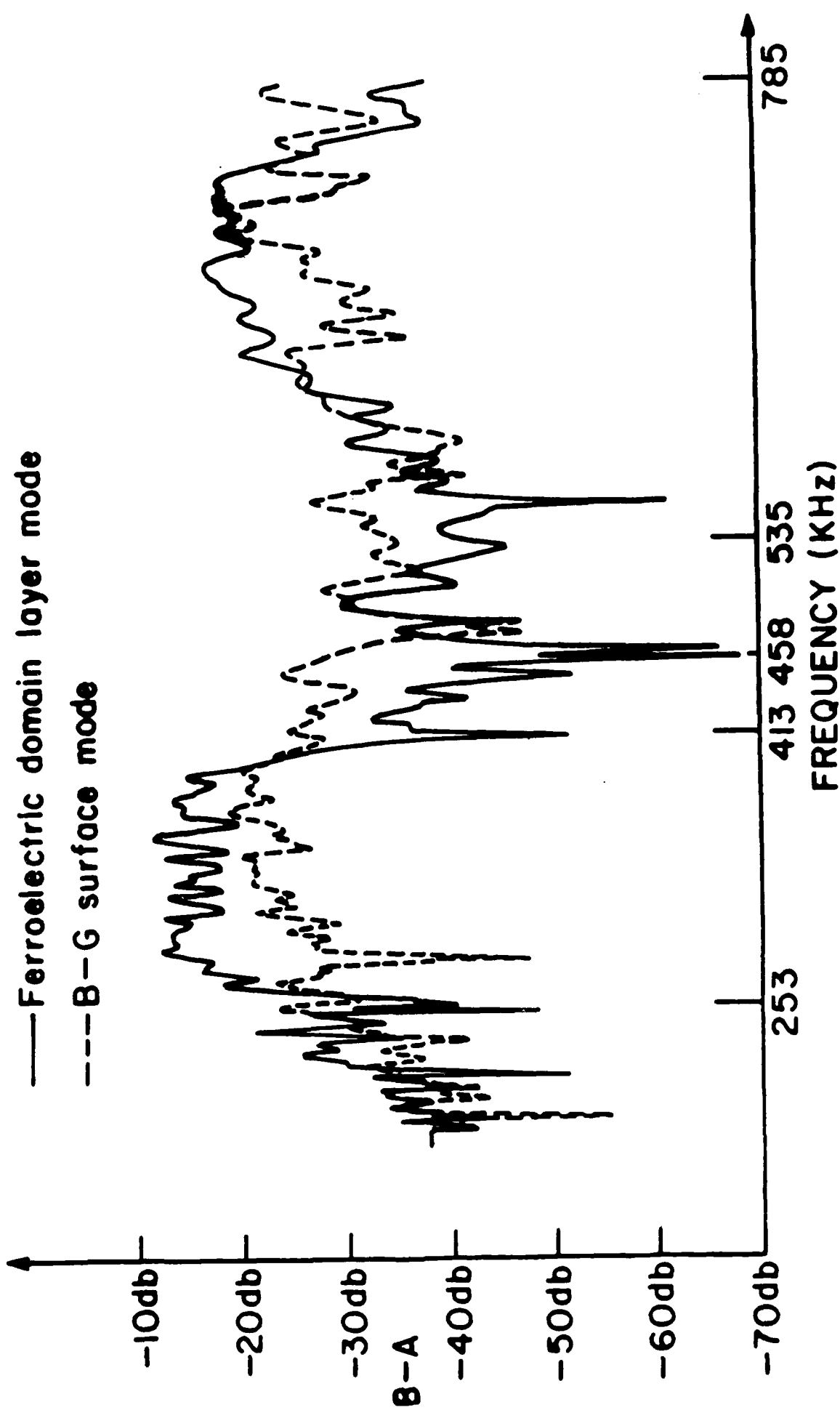


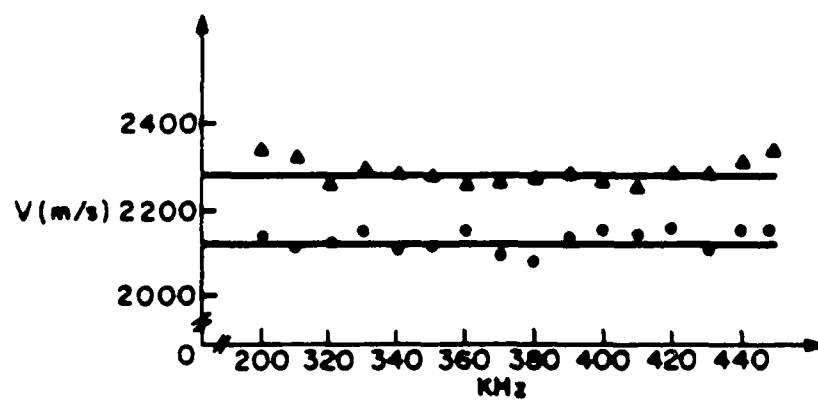


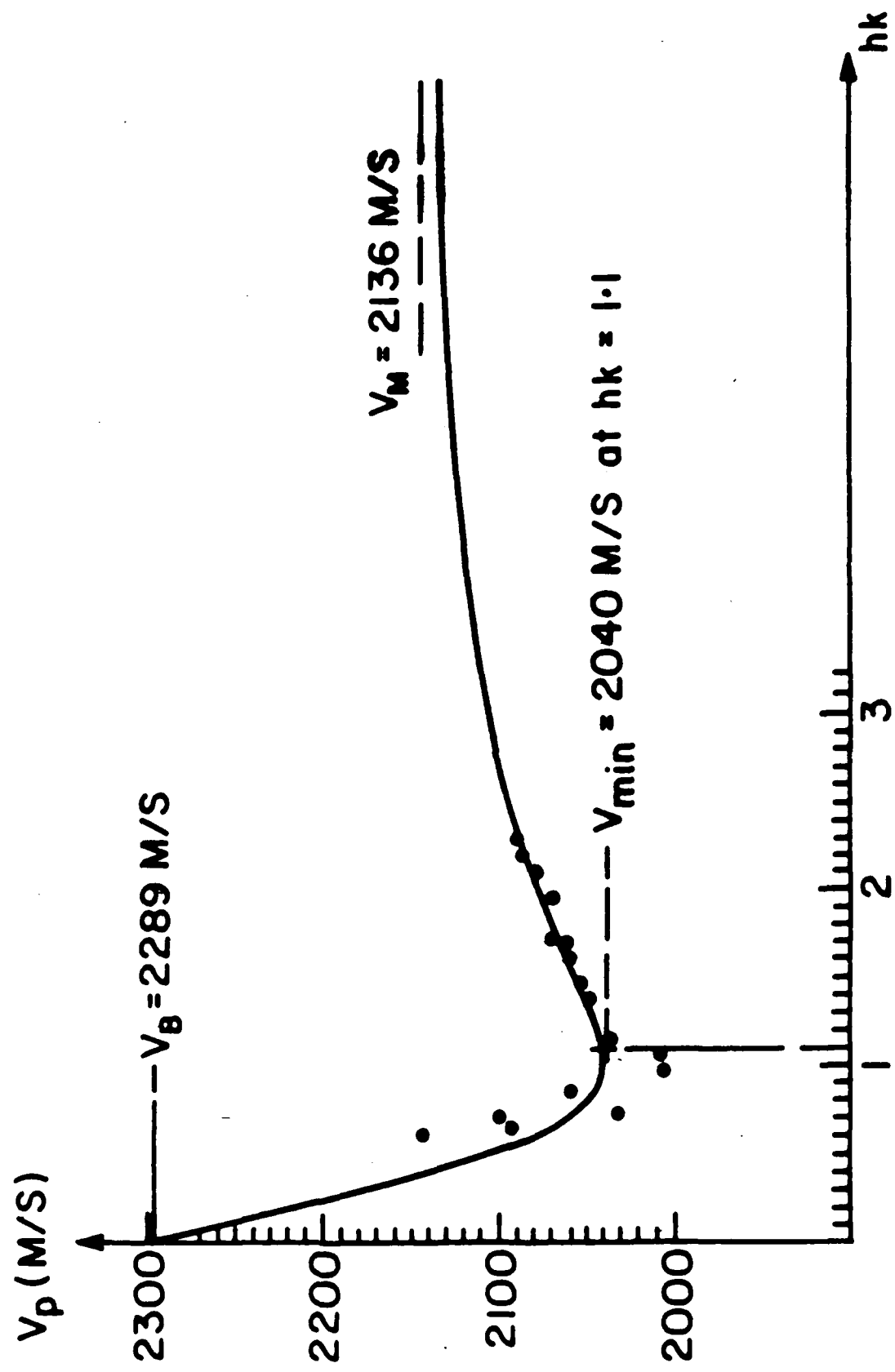


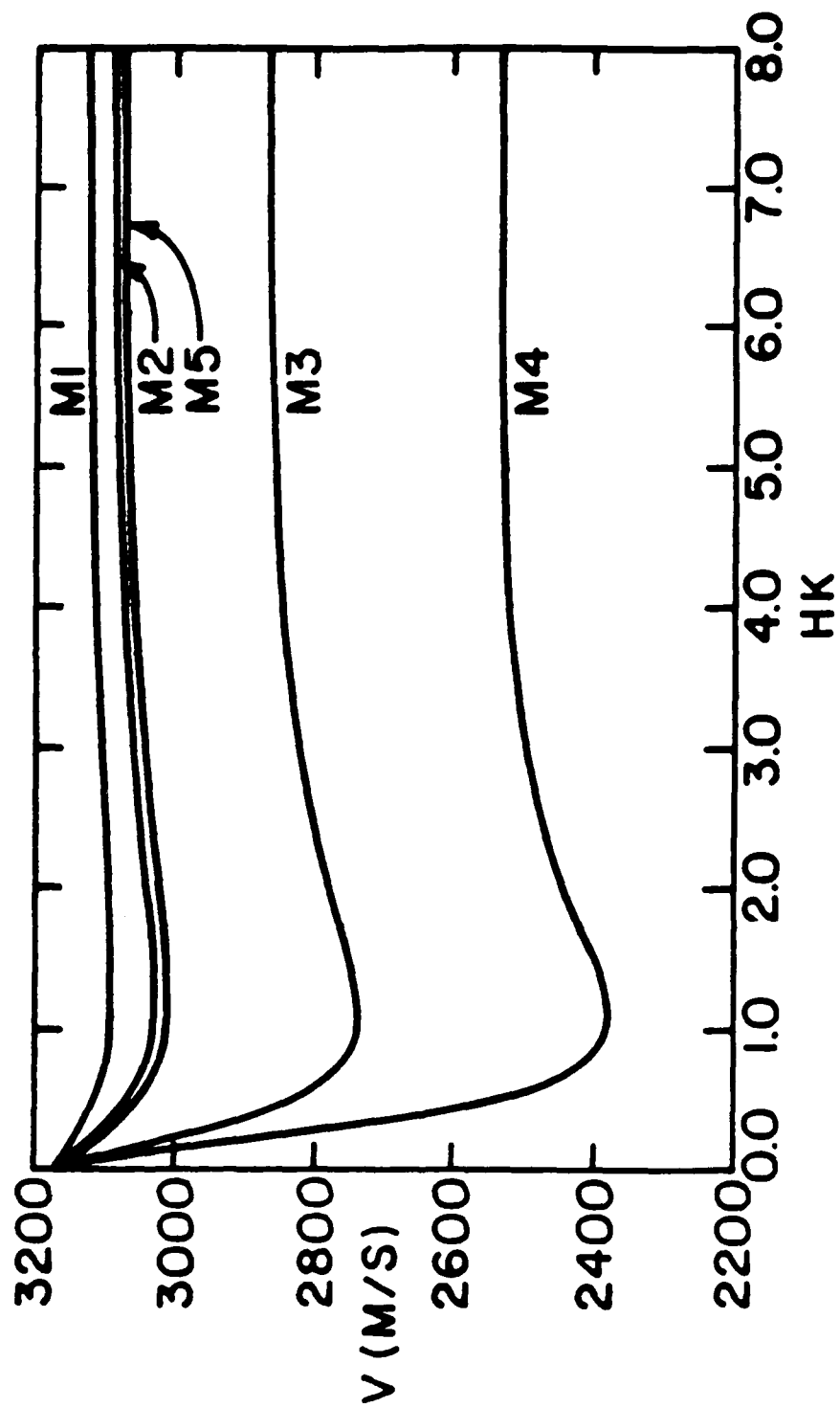


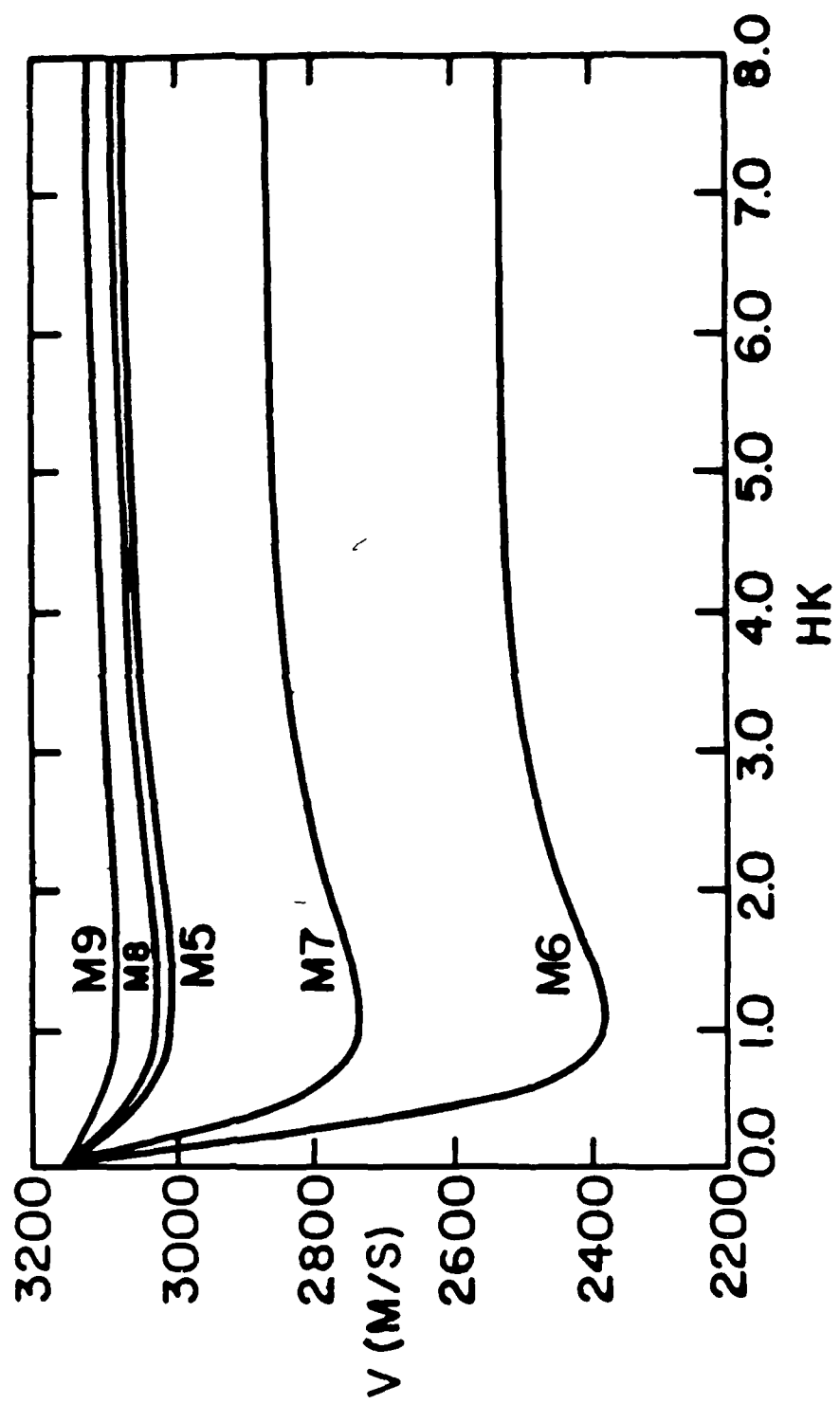


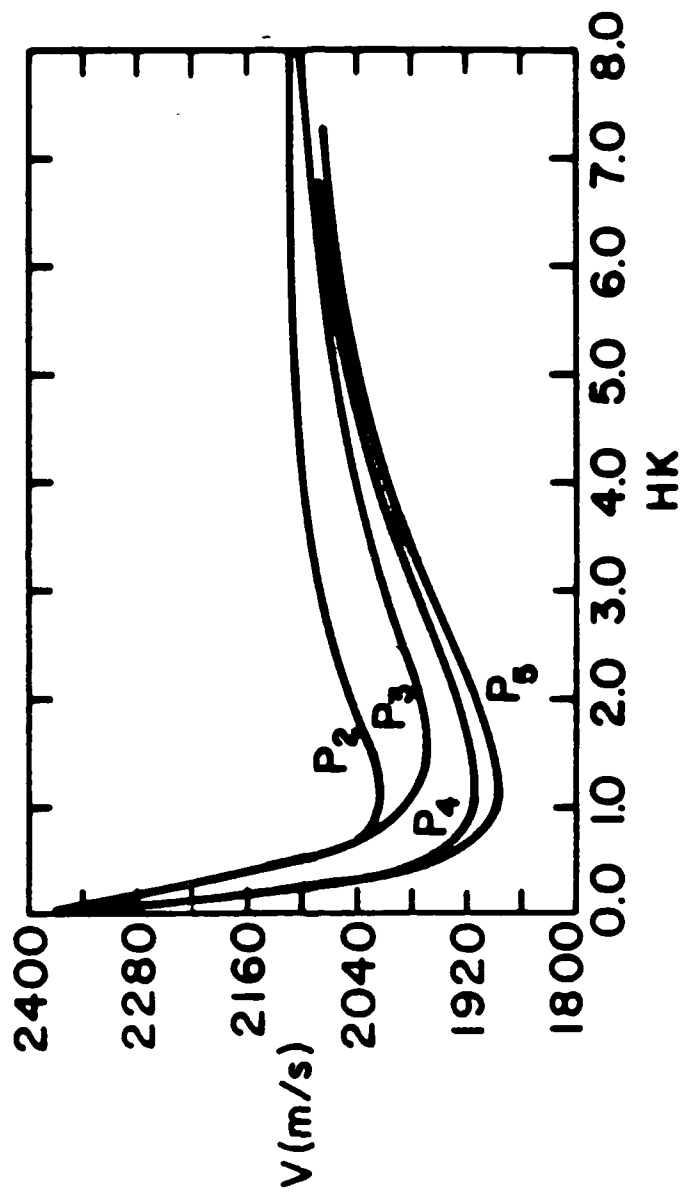




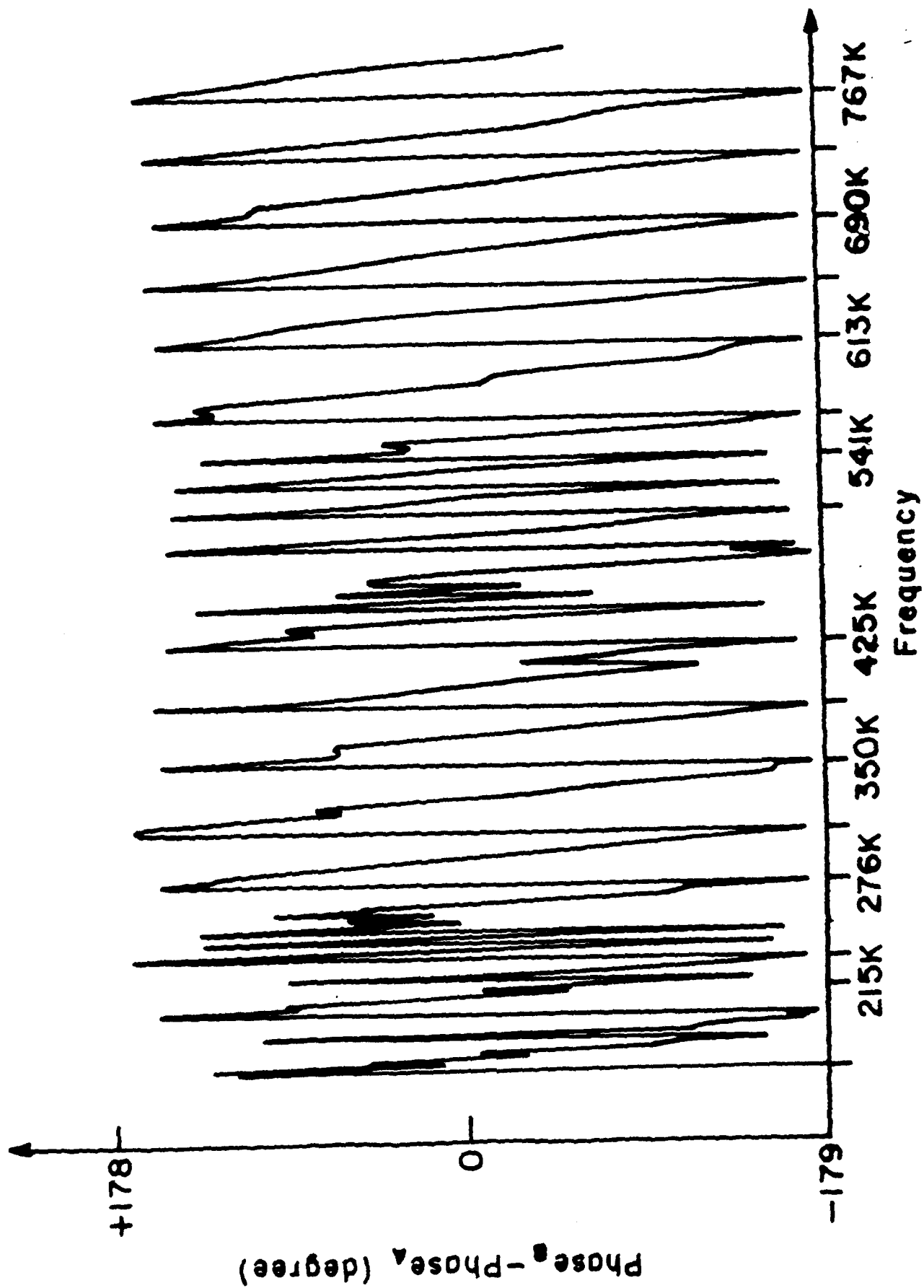












## PIEZOELECTRIC FIBER OPTIC ELECTRIC FIELD SENSOR

C.M. Lawson

The BDM Corporation, 7915 Jones Branch Drive, McLean, VA 22102

A. Malliyal, A.G. Bhalla, S.J. Jang, and L.E. Cross

The Pennsylvania State University, Materials Research Laboratory,  
University Park, PA 16802

Abstract--Two types of fiber optic interferometric electric sensors have been demonstrated where the fibers have been sensitized to electric fields in a novel way. In the first case, the fibers were embedded in a piezoelectric barium titanium silicate (fresnoite) glass-ceramic, and in the second case, in a PZT-polymer composite matrix.

### INTRODUCTION

Fiber optic sensors have recently received considerable attention because of their advantages over conventional sensors, including small size, immunity to electromagnetic interference, complete electrical isolation, and outstanding sensitivity. One of the potential applications for fiber optic sensing involves the detection of electric fields. Fiber optic electric field sensors have been shown using such diverse mechanisms as electro-absorption,<sup>1</sup> electrically induced fiber motion,<sup>2</sup> the electro-optic effect,<sup>3</sup> and piezoelectric strain.<sup>4,5</sup> This latter concept has been successfully demonstrated by coating one leg of a Mach-Zehnder interferometer with a piezoelectric polymer such as PVDF, in order to transduce an applied electric field into a measurable fiber strain.<sup>6,7</sup>

In this letter we describe the fabrication and performance of novel fiber optic electric field sensors in which one leg of a fiber optic interferometer is sensitized by a piezoelectric glass-ceramic or a PZT-polymer composite, instead of a piezoelectric polymer. The compliance of the piezoelectric glass-ceramic or the PZT-polymer composite is lower than that of PVDF polymer leading to a more efficient coupling of strain with the fiber. Two designs were used to sensitize fibers to applied electric fields. In the first design, unjacketed fibers were embedded in piezoelectric barium titanium silicate (fresnoite) glass-ceramics. In the second design, fibers were embedded in a PZT-polymer composite.

### SENSOR FABRICATION

The first type of sensors were prepared by embedding the

optical fibers in a piezoelectric glass-ceramic. The properties of grain oriented glass-ceramics which show piezoelectric properties (called polar glass-ceramics) have been investigated extensively.<sup>6</sup> Fresnoite glass-ceramics (compositions in the BaO-SrO-SiO<sub>2</sub>-TiO<sub>2</sub> system) were used in the present work. Glass plates of approximately one to two inches long and one half inch wide were prepared by melting the glass and casting the melt in graphite mold. One surface of the glass plates was fine polished and glass-ceramics with oriented crystallites were prepared by heating the glasses at 950 to 1000°C for two hours. Fine grooves were made on the crystallized surface and a fiber with approximately one inch of the jacket removed was embedded in the plate and cemented in place (ceramic #4).

The second group of sensors were fabricated from PZT ceramic (501A PZT) and a polymer to form a PZT-polymer composite. The fiber was cast in a sliced PZT plate as shown in Figure 1. Grooves

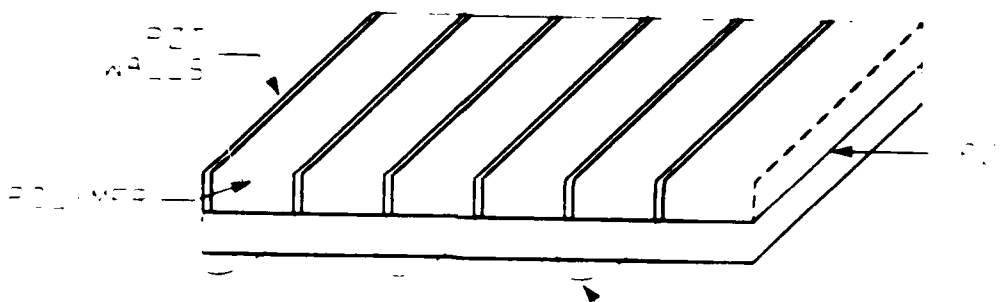


Figure 1. PZT-Polymer Composite Sensor

were made on a poled PZT disk of 1.5 inch diameter and 0.2 inch thickness with a diamond saw. Approximately 15 inches of jacketed optical fiber was laid inside the grooves and covered with a brass plate and the polymer was cured at 70°C for 12 hours. After curing, the two major surfaces of the PZT disk were electroded with air dry silver paste.

The polymer used for initial composite sensor fabrication (composite #4) was a stiff spurs epoxy. The low compliance of this epoxy provided efficient coupling of the strain generated from the PZT with the fiber. However, the use of this spurs epoxy led to thermal stress-induced fiber breakage, because of the differing thermal expansivity of the fiber and the spurs epoxy. To avoid this problem, a softer ecogel polymer was used (composite #5) which has a higher compliance than spurs epoxy. The

use of the eccogel polymer successfully eliminated fiber breakage, although the coupling of strain from the PZT to the fiber was not efficient. To increase the stiffness around the fiber the grooves in the PZT were filled with a paste of alumina powder and epoxy. The epoxy was cured at 70°C for 12 hours and the structure was supported by eccogel casting (composite #6). This structure successfully provided enhanced polymer stiffness without fiber breakage.

#### EXPERIMENTAL TESTING RESULTS

In the present work an all-fiber Mach-Zehnder interferometer was used to test the sensitized fibers. Light from a helium-neon laser was directed into a single mode fiber and split into a reference and sensing path by an input evanescent wave coupler. The fiber in the sensing path was fused into one of the electric field sensors described in the previous section, and the fiber in the reference path was fused to a phase shifter constructed by winding 100 turns of fiber on a piezoelectric cylinder with a two centimeter diameter. The other fiber ends of the sensor and phase shifter were fused to a second output evanescent wave coupler which mixes the two light beams and directs the resultant light on to photodetectors. The interferometer was maintained in quadrature with an active quadrature stabilization feedback circuit electrically connected to the reference path fiber phase shifter.<sup>7</sup>

To enable the application of an electric field, conductive electrodes were applied to the sensor and connected to a signal generator. The sensor signal-to-noise ratio (SNR) was directly measured by connecting the photodetectors to a spectrum analyzer and applying a signal of known frequency and voltage to the sensor. Figure 2 shows the SNR frequency response for each of the

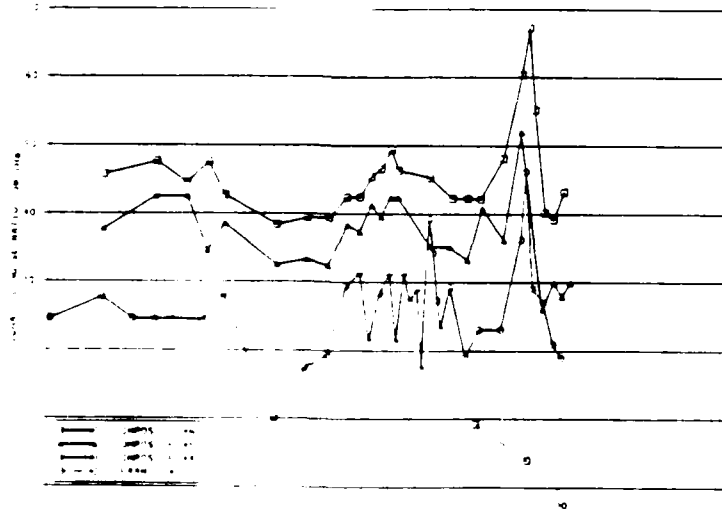


Figure 2. Sensor SNR Measurements vs. Frequency

four sensors described in the previous section in db/Hz, with a 1 volt RMS signal applied to each sensor. As can be seen from these plots, the sensitivity of the PZT-polymer composite sensors is higher than that of the glass-ceramic sensor. In addition, the sensitivity of composite sensor #6, in which the fiber is embedded in a stiff matrix of alumina powder and epoxy, is higher than that of composites #4 and #5.

In summary, we have demonstrated the feasibility of two types of fiber optic interferometric electric field sensors in which the fibers were sensitized to electric fields in a novel way. In the first case, the fibers were embedded in a piezoelectric glass-ceramic, and in the second case, in a PZT-polymer composite matrix. The SNR of these sensors was measured as a function of frequency, with a known signal voltage applied across the sensors.

#### ACKNOWLEDGEMENT

This work was supported by Rome Air Development Center.

#### REFERENCES

1. Su, S.F.: 'Fiber-optic electric-field sensor based on electro-absorption,' Presented at the 1984 Optical Society of America Annual Meeting, Talk WC7, San Diego, California.
2. Johnston, A.R.: 'Fiber-optic electric-field meter,' Nasa Tech Briefs, Fall 1985.
3. Yao, S.K., Findakley, T., Cordero-Innareta, A., R. Thaniyavarn, S. Hayward, G., and Chen, B.: 'Electromagnetic sensor using integrated optic channel waveguide modulator and polarization preserving fibers,' Proceedings SPIE, 1983, 412, pp. 154-159.
4. Koo, K.P., and Sigel, G.R.: 'An electric field sensor utilizing a piezoelectric polyvinylidene fluoride (PVF<sub>2</sub>) film in a single-mode fiber interferometer,' IEEE J. Quantum Electron., 1982, 28-13, pp. 670-675.
5. Mermelstein, M.D.: 'Optical-fiber copolymer-film electric-field sensor,' Appl. Opt., 1983, 22, pp. 1806-1809.
6. Halliyal, A., Safari, A., Bhalla, A.S., Newnham, R.E., and Cross, L.E.: 'Grain oriented glass-ceramics for piezoelectric devices,' J. Am. Cer. Soc., 1984, 67, pp. 331-335.
7. Jackson, D.A., Priest, R., Dandridge, A., and Iveten, A.B.: 'Elimination of drift in a single-mode fiber interferometer,' Appl. Opt. 1981, 20, p. 2926.

**ONR DISTRIBUTION LIST**  
**Basic Distribution List**  
**Technical and Summary Reports**

<u>Organization</u>	<u>No. Copies</u>
Defense Documentation Center Cameron Station Alexandria, VA 22314	12
Office of Naval Research Attn: Code 471 Department of the Navy 800 N. Quincy Street Arlington, VA 22217	1
Office of Naval Research Attn: Code 470 Department of the Navy 800 N. Quincy Street Arlington, VA 22217	1
Commanding Officer Office of Naval Research Branch Office Building 114, Section D 666 Summer Street Boston, MA 02210	1
Commanding Officer Office of Naval Research Branch Office 536 South Clark Street Chicago, IL 60605	1
Office of Naval Research San Francisco Area Office One Hallidie Plaza Suite 601 San Francisco, CA 94102	1
Naval Research Laboratory Attn: Code 6000 Washington, DC 20375	1
Naval Research Laboratory Attn: Code 6100 Washington, DC 20375	1
Naval Research Laboratory Attn: Code 6300 Washington, DC 20375	1

<u>Organization</u>	<u>No. Copies</u>
Naval Research Laboratory Attn: Code 2627	1
Naval Air Development Center Code 606 Attn: Mr. F.S. Williams Warminster, PA 18974	1
Naval Weapons Center Attn: Library China Lack, CA 93555	1
Naval Air Propulsion Test Center Attn: Library Trenton, NJ 08628	1
Naval Construction Batallion Attn: Materials Division Civil Engineering Laboratory Port Hueneme, CA 93043	1
Naval Electronics Laboratory Attn: Electron Materials Sciences Division San Diego, CA 92152	1
Naval Missile Center Materials Consultant Code 3312-1 Point Mugu, CA 92041	1
Commanding Officer Naval Surface Weapons Center Attn: Library White Oak Laboratory Silver Spring, MD 10910	1
Commander David W. Taylor Naval Ship Research and Development Center Bethesda, MD 10084	1
Naval Oceans Systems Center Attn: Library San Diego, CA 92132	1
Naval Underwater System Center Attn: Library Newport, RI 02840	1
Naval Postgraduate School Attn: Mechanical Engineering Dept. Monterey, CA 93940	1

<u>Organization</u>	<u>No. Copies</u>
Naval Air Systems Command Attn: Code 52031 Washington, DC 20360	1
Naval Air Systems Command Attn: Code 52032 Washington, DC 20360	1
Naval Sea System Command Attn: Code 05R Washington, DC 20362	1
Naval Facilities Engineering Command Attn: Code 03 Alexandria, VA 22331	1
Scientific Advisor Commandant of the Marine Corps Attn: Code AX Washington, DC 20380	1
Army Research Office Box 12211 Attn: Metallurgy and Ceramics Program Triangle Park, NC 27709	1
Army Materials and Mechanics Research Center Attn: Research Programs Office Watertown, MA 02172	1
Air Force Office of Scientific Research/NE Building 410 Bolling Air Force Base Attn: Chemical Science Directorate Washington, DC 20332	1
Air Force Office of Scientific Research/NE Building 410 Bolling Air Force Base Attn: Electronics and Materials Sciences Directorate Washington, DC 20332	1
Air Force Materials Laboratory Wright-Patterson AFB Dayton, OH 45433	1
Library Building 50, Room 134 Lawrence Radiation Laboratory Berkeley, CA 94720	1



<u>Organization</u>	<u>No. Copies</u>
NASA Headquarters Attn: Code RRM Washington, DC 20546	1
NASA Lewis Research Center Attn: Library 21000 Brookpark Road Cleveland, OH 44135	1
National Bureau of Standards Attn: Metals Science and Standards Division Washington, DC 20234	1
National Bureau of Standards Attn: Ceramics Glass and Solid State Science Division Washington, DC 20234	1
National Bureau of Standards Attn: Fracture and Deformation Division Washington, DC 20234	1
Director Applied Physics Laboratory University of Washington 1013 Northeast Fortieth Street Seattle, WA 98105	1
Defense Metals and Ceramics Information Center Battelle Memorial Institute 505 King Avenue Columbus, OH 43201	1
Metals and Ceramics Division Oak Ridge National Laboratory Box X Oak Ridge, TN 37380	1
Los Alamos Scientific Laboratory Box 1663 Attn: Report Librarian Los Alamos, NM 87544	1
Argonne National Laboratory Metallurgy Division Box 229 Lemont, IL 60439	1
Brookhaven National Laboratory Technical Information Division Attn: Research Library Upton, Long Island New York 11973	1

Organization

Office of Naval Research  
Branch Office  
1030 East Green Street  
Pasadena, CA 91106

No. Copies

1

**Supplementary Distribution List A**  
**Electronic, Magnetic and Optical Ceramics**

**Organization**

Advanced Research Project Agency  
Materials Science Director  
1400 Wilson Boulevard  
Arlington, VA 22209

Dr. Don Berlincourt  
Channel Products  
16722 Park Circle Drive W.  
Chagrin Falls, OH 44022

Dr. J.V. Biggers  
The Pennsylvania State University  
Materials Research Laboratory  
University Park, PA 16802

Mr. George Boyer  
Sensor Systems Program  
Office of Naval Research  
Code 222  
Arlington, VA 22217

Dr. Dean Buckner  
Piezo Products Division  
Bulton Industries  
Box 4300  
Fullerton, CA 92634

Dr. Robert Callahan  
Channel Products  
839 Ward Drive  
Box 3680  
Santa Barbara, CA 93105

Professor L.E. Cross  
Materials Research Laboratory  
The Pennsylvania State University  
University Park, PA 16802

Mr. N. Coda  
Vice President for Engineering  
Erie Technological Products  
West College Avenue  
State College, PA 16801

Dr. N. Perrone  
Code 474  
Office of Naval Research  
800 N. Quincy Street  
Arlington, VA 22217

Dr. Gene Haertling  
Motorola Corporation  
3434 Vassar, NE  
Albuquerque, NM 87107

Dr. W.B. Harrison  
Honeywell Ceramics Center  
1885 Douglas Drive  
Golden Valley, MN 55422

Dr. C.M. Stickley, V.P.  
The BDM Corporation  
7915 Jones Branch Drive  
McLean, VA 22102

Dr. L.L. Hench  
Department of Metallurgy  
University of Florida  
Gainesville, FL 32603

Dr. B.F. Rider  
Rockwell International  
400 Collins Road NE  
Cedar Rapids, IA 52406

Dr. F. Robert Hill  
Marine Resources  
755 Highway 17 and 92  
Fern Park, FL 32730

Dr. B.G. Koepke  
Honeywell, Inc.  
Corporate Research Center  
10701 Lyndale Avenue South  
Bloomington, MN 55420

Dr. R. Lapetina  
Edo Western Corporation  
2645 South 300 West  
Salt Lake City, UT 84115

Mr. C. LeBlanc  
Naval Underwater Systems Center  
TD 121  
Newport, RI 02840

Professor R. Roy  
Materials Research Laboratory  
The Pennsylvania State University  
University Park, PA 16802

Dr. Frank Recny  
General Electric  
Court Street  
Plant Building C  
Box 1122  
Syracuse, NY 13201

Dr. J.H. Rosolowski  
General Electric Company  
Research and Development Center  
Box 8  
Schenectady, NY 02301

Dr. P.L. Smith  
Naval Research Laboratory  
Code 6361  
Washington, DC 20375

Dr. R.W. Timme  
Naval Research Laboratory  
Code 8275  
Underwater Sound Reference Division  
Box 8337  
Orlando, FL 32806

Dr. Charles C. Walker  
Naval Sea Systems Command  
National Center #3  
2531 Jefferson Davis Highway  
Arlington, VA 20390

Dr. Paul D. Wilcox  
Sandia Laboratories  
Division 2521  
Albuquerque, NM 87115

The State University of New York at Alfred  
Materials Science Division  
Alfred, NY 14802

Dr. R. Rice  
Naval Research Laboratory  
Code 6360

Dr. David C. Hill  
Member, Technical Staff  
Texas Instruments, Inc.  
Attleboro, MA 02703

Dr. S.K. Kurtz  
Materials Research Laboratory  
The Pennsylvania State University  
University Park, PA 16802

Dr. N. Tallan  
AFML Wright-Patterson AFB  
Dayton, OH 45433

Dr. H.E. Bennett  
Naval Weapons Center  
Code 3818  
China Lake, CA 93555

Dr. Michael Bell  
Inorganic Materials Division  
National Bureau of Standards  
Washington, DC 20234

Dr. R. Bratton  
Westinghouse Research Laboratory  
Pittsburgh, PA 15235

Dr. Joe Dougherty  
Materials Research Laboratory  
The Pennsylvania State University  
University Park, PA 16802

Dr. James Pappis  
Raytheon Co.  
Research Division  
28 Seyon Street  
Waltham, MA 02154

Dr. Perry A. Miles  
Raytheon Co., Res. Div.  
28 Seyon Street  
Waltham, MA 02154

Dr. P.E.D. Morgan  
Rockwell Science Center  
1049 Camino Dos Rios  
Box 1085  
Thousand Oaks, CA 91360

Dr. G. Ewell  
MS6-D163  
Hughes Aircraft Company  
Centinela and Teale Streets  
Culver City, CA 90230

Dr. George W. Taylor  
Princeton Resources, Inc.  
Box 211  
Princeton, NJ 08540

Mr. John J. Theirmann  
Physics International  
2700 Merced Street  
San Leandro, CA 94577

Dr. Herb Moss  
RCA Laboratories  
Princeton, NJ 08540

Dr. R.E. Newnham  
Materials Research Laboratory  
The Pennsylvania State University  
University Park, PA 16802

Dr. Charles S. Sahagian, Chief  
EM Technology Branch, SSS Division  
HQ Rome Air Dev. Center (AFSC)  
Deputy for Electronic Technology  
Hanscom AFB, MA 01731

Dr. J. Smith  
GTE Sylvania  
100 Endicott Street  
Danvers, MA 01923

Dr. Wallace A. Smith  
North American Philips Laboratories  
345 Scarborough Road  
Briarcliff Manor, NY 10510

Mr. Raymond E. Sparks  
Technology Library R220  
Delco Electronics Division/GMC  
Box 1104  
Kokomo, IN 46901

Dr. Manfred Kahn  
Senior Scientist, Prod. Dev.  
AVX Ceramics  
Myrtle Beach, SC 29577

Mr. G. Goodman, Manager  
Corporation of Applied Research Group  
Globe-Union, Inc.  
5757 North Green Bay Avenue  
Milwaukee, WI 53201

Dr. A.E. Clark  
Naval Surface Weapons Center  
White Oak Laboratory  
Silver Spring, MD 20910

Director  
Applied Research Laboratory  
The Pennsylvania State University  
University Park, PA 16802

Dr. D. Carson  
Code 7122  
Naval Ocean Systems Center  
San Diego, CA 92152

Dr. C. Hicks  
Code 631  
Naval Ocean Systems Center  
San Diego, CA 92152

Dr. R. Smith  
Code 7122  
Naval Ocean Systems Center  
San Diego, CA 92152

Professor R. Buchanan  
Department of Ceramic Eng.  
University of Illinois  
Urbana, IL 61801

Professor B.A. Auld  
Stanford University  
W.W. Hansen Laboratories of Physics  
Stanford, CA 94306

Dr. S. Musikant  
General Electric Co.  
3188 Chestnut Street  
Philadelphia, PA 19101

Dr. A. Gentile  
Hughes Research Labs  
3011 Malibu Canyon Road  
Malibu, CA 90265

Dr. J. Harrington  
Hughes Res. Labs.  
3011 Malibu Canyon Road  
Malibu, CA 90265

Professor G. Kino  
Stanford University  
Stanford, CA 94305



Dr. Gordon Martin  
2627 Burgener  
San Diego, CA 92110

Deborah Graves  
Ceramic Engineer  
Endevco  
Rancho Vie Jo Road  
San Juan Capistrano, CA 92675

Army Research Office  
Box CM Duke Station  
Attn: Met. and Ceram. Div.  
Durham, NC 17706

National Bureau of Standards  
Inorganic Matls. Division  
Washington, DC 20234

National Bureau of Standards  
Metallurgy Division  
Washington, DC 20234

Naval Air Systems Command  
Code 320  
Washington, DC 20360

Pacific Missile Test Center  
Materials Consultant  
Code 4121  
Pt. Mugu, CA 93042

Naval Research Lab  
Code 6400  
Washington, DC 20390

Naval Sea System Command  
Code 035  
Washington, DC 20362

Naval Ship Engr. Center  
Code 6101 CTR BG #2  
3700 East-West Highway  
Prince Georges Plaza  
Hyattsville, MD 20782

Office of Naval Research  
Department of the Navy  
Code 102  
Arlington, VA 22217

Dr. G. Bansal  
Battelle Laboratories  
505 King Avenue  
Columbus, OH 43201

Dr. F.F. Lange  
Rockwell International  
Box 1085  
1049 Camino Dos Rios  
Thousand Oaks, CA 91360

Dr. G. Denman  
Code LPJ  
AFML Wright-Patterson AFB  
Dayton, OH 45433

Sheldon Derwiler, Disp. Mgr.  
Adv. Technol. Laboratories  
13208 Northrup Way  
Box 6639  
Bellevue, WA 98007

Dr. W.G.D. Frederick  
AFML Wright-Patterson AFB  
Dayton, OH 45433

Dr. P. Giellisse  
University of Rhode Island  
Kingston, RI 02881

Mr. G. Hayes  
Naval Weapons Center  
China Lake, CA 93555

Dr. R.N. Katz  
Army Materials and Mechanics  
Research Center  
Watertown, MA 02171

Dr. P.L. Lall  
Office of Naval Research  
666 Summer Street  
Boston, MA 02210

Dr. P. Land  
AFML Wright-Patterson AFB  
Dayton, OH 45433

Dr. Eugene A. Larson, Pres.  
Blue River Laboratories  
Box 442  
Lewistown, PA 17044

Dr. George Benthien  
Naval Ocean Systems Center  
Code 212  
San Diego, CA 92152

Mr. K. Letson  
Redstone Arsenal  
Huntsville, AL 35809

Mr. G. Schmitt  
AFML Wright-Patterson AFB  
Dayton, OH 45433

Mr. F. Markarin  
Naval Weapons Center  
China Lake, CA 93555

Mr. K.D. McHenry  
Honeywell Corp. Tech. Center  
10701 Lyndale Avenue South  
Bloomington, MN 55420

Dr. R.R. Neurgaonkar  
Rockwell International Science Center  
1049 Camino Dos Rios  
Box 1085  
Thousand Oaks, CA 91360

Norton Company--Library  
Industrial Ceramics Division  
Worcester, MA 01606

James W. Pell  
Manager of Development  
Rohe Scientific Corporation  
2722 S. Fairview Street  
Santa Ana, CA 92704

Dr. R.C. Pohanka  
Room 619 Ballston Tower  
800 N. Quincy Street  
Arlington, VA 22217

Dr. R.A. Queeney  
126 Hammond Building  
The Pennsylvania State University  
University Park, PA 16802

J.J. Rasmussen, Manager  
Applied Research Division  
Montana Energy and MHD R and D  
Box 3809  
Butte, MT 59701

Dr. R. Ruh  
AFML Wright-Patterson AFB  
Dayton, OH 45433

James Runt  
313 Steidle Bldg.  
The Pennsylvania State University  
University Park, PA 16802

Dr. T. Sentementes  
GTE Sylvania  
100 Endicott Street  
Danvers, MA 01923

State University of New York  
College of Ceramics  
Attn: Library  
Alfred University  
Alfred, NY 14802

Dr. R.E. Tressler  
Ceramic Science Section  
226 Steidle Building  
The Pennsylvania State University  
University Park, PA 16802

Eric Udd  
McDonnell Douglas Aston.  
5301 Bolsa Avenue  
Huntington Beach, CA 92647

Dr. T. Vasilos  
AVCO R and Adv. Dev. Div.  
201 Lowell Street  
Wilmington, MA 01887

Mr. J.D. Walton  
Engineering Experiment Station  
Georgia Institute of Technol.  
Atlanta, GA 30332

Mr. L.B. Weckesser  
Applied Physics Laboratory  
Johns Hopkins Road  
Laurel, MD 20810

Mertan Brooks  
Sandia National Labs  
Division 7472  
Box 5800  
Albuquerque, NM 87185

Darnall P. Burks  
Sprague Electric Company  
Ceramic Capacitor Operations  
Box 5327  
Wichita Falls, TX 76307

Dr. Kim Ritchie  
AVX Corporation  
Box 867  
Myrtle Beach, SC 29577

Roger T. Dirstine  
Unitrode Corporation  
580 Pleasant Street  
Watertown, MA 02172

END

DATED

FILM

8-88

DTIC